THE RHEOLOGY AND THERMODYNAMICS OF POLYMER NANOCOMPOSITES

By

Jonathan E. Seppala

A DISSERTATION

Submitted to
Michigan State University
in partial fulfillment of the requirements
for the degree of

DOCTOR OF PHILOSOPHY

Chemical Engineering

2010

ABSTRACT

THE RHEOLOGY AND THERMODYNAMICS OF POLYMER NANOCOMPOSITES

By

Jonathan E. Seppala

Recent advancements in the quality and quantity of nanoparticles have increased their use in polymer nanocomposites. Their small size creates the opportunity for interesting size ratios and limits. One of these, the nanoparticle limit, where the particle is smaller than the suspending polymer radius of gyration, has resulted in surprising effects to the mechanical properties among them a decrease in the melt viscosity and an increased Young's modulus in the solid state. Dispersing nanoparticles within polymers plays a critical role in nanocomposite properties, and the dispersion stability is very sensitive to the confinement limit ($h < R_g$) and solubility limit ($a < R_g$). Bimodal blends of linear polystyrene with tightly crosslinked polystyrene nanoparticle having a small volume fraction of unconfined chains or a small volume fraction of chains larger than the nanoparticle fail to show any unique features. Knowing the sensitivity of these limits allows for proper selection of polydisperse nanoparticles and polydisperse linear chains producing a fully polydisperse system with reduced viscosity. Rheology gives a rough estimate of dispersion in a system of tightly crosslinked polystyrene nanoparticles in linear perdeuterated polystyrene via either a viscosity reduction or adherence to Einstein's predicted viscosity increase. Dispersion or agglomeration in these systems is confirmed though small angle neutron scattering and solubility and mixing energies are calculated via Guinier and Virial analysis. These results follow the scaling penalty from chain stretching as nanoparticle radius approaches linear polymer radius of gyration. However, even in the agglomerated case rapid precipitation produced a well dispersed sys-

tem that phase separated during thermal annealing. Refinements to the rapid precipitation blending technique yielded an ideal polymer concentration for proper blending and subtle difficulties are discussed. Finally the melt viscosity of poly(methyl methacrylate) C_{60} and poly(methyl methacrylate) Fe_3O_4 nanocomposites show a reduced viscosity, results which are contrary to recently reported experiments. The method of dispersion is the key difference between this work and what has been reported in the literature. Young's Modulus was also measured with only the poly(methyl methacrylate) Fe_3O_4 nanocomposite resulting in an increase, indicating a dependence of unusual reinforcement on nanoparticle size and spacing. These details and other phenomena are discussed in this work.

To my wife Clare.

ACKNOWLEDGMENT

First and foremost I would like to thank my adviser Michael Mackay for his guidance as an adviser and rheology expert. It is difficult to remember how little I knew about rheology and research in general when I started. There are an unknown number of details regarding each that I leaned from Dr. Mackay throughout the years and I would not hesitate to point any new graduate student in his direction.

Special thanks to BASF for their funding of my work; none of it would have been possible without their generous contribution.

Though moving universities is a difficult and disruptive event, it brought me into contact with far more diverse group of people and expertise. My wife, Clare on the other hand moved away from friends and family without benefiting quite as much. I owe her a great deal of gratitude for the sacrifices she made while I pursued my PhD.

From the Mackay group, thank you to Jon Kiel and Tzuchia Tseng who were my best friends, constant companions, and competent colleagues. Additional thanks to Dr. David Bohnsack for teaching me how to use the instruments in our lab and for being available to discuss my project even after his graduation.

At the University of Delaware, I would like to thank the MSEG Department for making us feel welcome following our move and helping us to get adjusted to the UDel community. Special thanks to Professor Norman Wagner in CHEG for use of his rheology equipment, the neutron scattering expertise of his group, and for allowing me to join in their group meetings.

Neutron scattering can be very complex experiment to setup and to analyze. Fortunately

I was aided by Dr. Yun Liu, Dr. Aaron Eberle, and Dr. Armin Optiz. Thank you to the staff in CHEMS at MSU: Jennifer Somerville, Jennifer Peterman, Nikki Shook, and Joanne Peterson; as well as the staff in MSEG atUDel: Charles Garbini, Christine Williams, Dionne Putney, and Steve Beard.

Moving also afforded me two sets of graduate school friends, at MSU: Katie Shipley, Ming Wei Lau, Dan Olds, Megan Ramanowich, Luke Granlund, and Shannon Nicely; and atUDel:Conan Wieland, Laura Polvich, Katie Feldman, Carl Giller, and Bakathyr Ali - each of whom contributed in their own ways whether it was working together on course projects or discussing research problems.

I also would like to thank my parents, Fay and Dennis, and sisters, Jean and Josie for their support throughout the years and my Aunts, Laurie and Sharon, who were always interested in the technical details of my work and who provided a much needed outside perspective.

TABLE OF CONTENTS

LIST OF TABLES

LIST OF FIGURES

Chapter 1

Introduction

One of the primary draw backs in polymer-composite production is the increase in viscosity of the polymer-composite melt.[10, 11] It is generally accepted that addition of particles to a fluid will increase the viscosity of the composite fluid. In a simple hydrodynamic theory proposed by Einstein the viscosity of a suspension scales proportionally to the volume of the particles suspended via the following equation, $\eta_r = 1 + 2.5\phi$, where η_r is the viscosity ratio (suspension/neat) and ϕ is the volume fraction of particle.[4] Many subsequent models, theoretical and empirical have been developed which accurately cover a wide variety of materials.[10] These models share one common feature a viscosity increase that scales with the volume fraction of the particle added. For all of these models the particle is assumed to be rigid and for a wide variety of systems the particle is larger than the individual solvent molecules. This is also true for most polymer nanocomposites, where, even though the polymer chains are quite large, the particle introduced is still larger.

As interest in nanoscience and nanoparticles has grown the uniformness and quantity of nanoparticles has improved. Gram quantities of highly uniform very small, less than 10nm, nanoparticles made from a variety of materials, organic and inorganic, are now available.[2] Many of the common inorganic nanoparticles, Fe_2O_4, $CdSe$[14], etc, are available with surfactants and stabilizing agents allowing inorganic materials to be suspended in organic solvent, which is crucial for suspending in most polymers. These nanoparticle are being blended with a variety of polymer in a effort to produce new properties in otherwise well studied polymers. Changes is absorbance, dielectric strength[15], tailored refractive index[16] and even anti-bacterial[17] properties are being incorporated. However, many of these nanocomposites have large scale agglomeration due to nanoparticle size, dispersion method, and/or insolubility.

Recent work has been published detailing the effect of well dispersed nanoparticles which have a radius smaller than the radius of gyration of the suspending polymer, the primary effect being the decrease in melt viscosity of the composite. This is contrary to the general understanding of suspensions in polymeric materials. In a effort to understand the decrease in viscosity several other effects and some requirements were discovered. These are listed below.

1. Non-Einstein-Like viscosity decrease upon addition of nanoparticles.[18, 19, 20]

2. Faster-than-expected diffusion of nanoparticle in a polymer matrix.[21]

3. Chain swelling upon addition of nanoparticles.[22, 23, 24, 25, 26, 27, 28]

4. Confinement requirement for Non-Einstein-Like decrease.[29]

5. Entanglement[30] requirement for Non-Einstein-Like decrease.[29]

6. Appropriate method for dispersing nanoparticles in a polymer matrix.[20]

7. Indirect reinforcement of polymers by nanoparticle addition.[20]

The first and most surprising effect is the afore mentioned decreased terminal viscosity. It is generally accepted that addition of nanoparticles to an fluid increases the viscosity.[9, 10, 11, 12] Einstein first described this with a simple hydrodynamic argument where the fluid around a spherical non interacting particle takes a longer more torturous path.[4] This change in the flow field results in an increased viscosity. There are currently many different models and theoretical descriptions available for a wide variety of particles. However to date none describe a decreased viscosity upon particle addition.

In Chapter 2 of this thesis, the subtleties of nanoparticle confinement of polymer chains and the solubility of nanoparticles in linear chains are addressed with respect to melt viscosity reduction. Bimodal linear polystyrene blends composed of a monodisperse high and low molecular weight standards blended with two sizes of tightly crosslinked polystyrene nanoparticles[2]. The nanoparticle volume fraction chosen leaves a portion of the linear low molecular molecular weight content unconfined and the viscosity reduction scales indirectly with the unconfined volume. The viscosity reduction is surprisingly sensitive to volume of unconfined chains as only a small fraction completely suppresses the effect. The same is true for solubility, using a larger nanoparticles which are insoluble in the linear low molecular weight content the viscosity scale with Einstein's relation.[4] With a better understanding of these limits a polymer-nanocomposite with polydisperse linear chains and polydisperse crosslinked nanoparticles with reduced viscosity was created.

In Chapter 3 of this thesis, the dispersion characteristics and miscibility of ideal nanoparticles in a polymer melt are extended into new particle/polymer size ratios which is the key to nanoparticle phase stability[31, 32, 33]. Two sizes of tightly crosslinked polystyrene nanoparticles[2] blended with perdeuterated monodisperse linear polystyrene were studied via small angle neutron scattering (SANS) and rheology. SANS results of a properly confined ($h < R_g$) and size matched ($a < R_g$) system show well dispersed nanoparticles, with a negative mixing energy. When compared with previous work at other nanoparticles to polymer size rations the mixing energy scales appropriately with the mixing theory developed by Mackay and coworkers[20]. Rheology of this system shows a reduced viscosity. SANS results on the unconfined ($h > R_g$) and/or sized mismatched system ($a \approx R_g$) shows large agglomerates (40X the individual nanoparticle) that start from a well dispersed state and

grow during thermal annealing. The melt viscosity of this system follows Einstein's relation.

In Chapter 4 of this thesis, the methods of dispersion are used to make polymer-nanocomposites with reduced melt viscosity and increased glassy toughness. Polymer-nanocomposites with monodisperse poly(methyl methacrylate) (PMMA) standards, commercially available Fullerenes (C_{60}) and oleic acid stabilized magnetite (Fe_3O_4) are prepared by rapid precipitation. Two molecular weights of linear PMMA were used each producing a C_{60} composite with reduced melt viscosity but no change to the Young's Modulus. A combination of high molecular weight PMMA and Fe_3O_4 produced a composite with both reduced viscosity and increased Young's Modulus (unusual reinforcement). Small and wide angle x-ray scattering (SAXS and WAXS) confirmed dispersion quality.

In Chapter 5 of this thesis, some details of rapid precipitation are reported. Blends of tightly crosslinked polystyrene nanoparticles[2] with monodisperse and polydisperse polystyrene and prepared by rapid precipitation using a range of polymer concentrations solution. A maximum concentration was determined by examining the precipitate, at 25 mg/mL or above the nanoparticles remained suspended in the supernatant. This concentration happens to be just above the overlap concentration for the molecular weight used. Using this limit a polymer-nanocomposite of oleic acid stabilized cadmium selenide quantum nanocrystals[14] in monodisperse linear polystyrene is produced. A well dispersed polymer-nanocomposite was created and confirmed though small angle x-ray scattering (SAXS).

1.1 Research Objectives

The primary objective of this work is to expand the understand of the confinement and solubility limits for polymer-nanocomposites with reduced viscosity. Using controlled bimodal

blends these two limits are investigated and the results are used to create a polydisperse-polydisperse polymer-nanocomposite. Dispersion and mixing energy of ideal polymer-nanocomposites are determined for new size ratios further confirming the mixing theory proposed in the literature.[20] PMMA multifunctional polymer-nanocomposites are created and characterized. Finally rapid precipitation is studied to created better nanoparticle dispersions.

Chapter 2

Bimodal Blends

Well dispersed nanoparticles that are smaller than the radius of gyration of the neat polymer form a stable suspension which have unusual viscosity properties. It was previously shown that decreases in melt viscosity were seen for systems where a large enough volume of nanoparticles were added to confine all of the chains in a given polymer matrix.[19] Here we study bidisperse linear blends with ideal nanoparticles to see if the viscosity decrease occurs in these system. Confinement is achieved when the interparticle half-gap (h) is less than the radius of gyration. The interparticle half gap is calculated using Equation 2.1, where a is the radius of the particle, ϕ_m is the maximum packing fraction (0.638 for random packing) and ϕ is the volume fraction of the nanoparticle.

$$\frac{h}{a} = \sqrt[3]{\frac{\phi_m}{\phi}} - 1 \tag{2.1}$$

The radius of gyration (R_g) for polystyrene (PS), the polymer used in this work, is calculated using Equation 2.2 based on a fit to other work[34], where R_g is in nanometers and MW is the molecular weight of a given chain in kiloDaltons. For monodisperse systems the chain size can be calculated from the number average molecular weight (M_n) or weight average molecular weight (M_w) since the difference in chain size between the two will be very small. Obviously this will not be the case for bidisperse or polydisperse systems.

$$Rg[nm] = 0.83\sqrt{MW[kD]} \tag{2.2}$$

For the purpose of this experimental set we wished to selectively confine specific portions of a bidisperse blend. Blends of low and high molecular weight monodisperse linear polystyrene standards with small and large tightly crosslinked polystyrene nanoparticles[2] are prepared by the rapid precipitation technique.[20]

There are several limits that can be addressed just based on chain length, nanoparticle size and nanoparticle volume. Consider that the nanoparticles are displacing entanglements in a time (or frequency) dependent manner. If the material properties are measured at frequency or shear rate faster than the particle diffusion time the nanoparticle-polymer interactions may appear as entanglements. The chains themselves are still limited by their remaining entanglements[30] and are restricted to motion by reptation[35, 36, 37, 38] along their contour length[39, 40]. However, moving to lower frequencies or shear rates the nanoparticles can diffuse away during the deformation resulting in a decrease in entanglement density per chain and a decreased viscosity. In this scenario the lowest theoretical viscosity will be a system where enough nanoparticles are present to disrupt all of the chain entanglements. Since the nanoparticles are diffusing uninhibited by the entanglements seen in previous work[21] the viscosity reduction is most pronounced in the terminal region. This system would have a baseline viscosity at the Rouse limit ($\eta \propto M^1$)[36, 38] plus the increase predicted by Einstein's hydrodynamic theory with Batchelor correction where applicable ($\eta_r = 1 + 2.5\phi + 6.2\phi^2$)[4, 5] assuming the volume fraction of nanoparticles required was still within the proper range. The upper bound on viscosity is that of a neat system which typically scales to the well known 3.4-3.8 power ($\eta \propto M^{3.4}$)[41, 42, 43] for most linear polymers. This means for a larger molecular weight a larger decrease can be achieved since there is a wider range between the Rouse limit and the entangled limit.

While some may argue the viscosity decrease is simply that of a blended system with a low viscosity additive it should be pointed out that the viscosity decrease is less than that predicted by addition of a volume having zero viscosity and the tightly crosslinked polystyrene nanoparticles[2] themselves have no terminal viscosity since in the pure state

they are a jammed system.[1] A thorough understanding of the limits of the viscosity decrease will allow it's predictable use in future systems.

2.1 Experimental Methods

75 kD and 393 kD monodisperse linear polystyrene standards (Scientific Polymer Products), here labeled 75PS and 393PS, were used as received.

40 kD and 230 kD tightly crosslinked polystyrene nanoparticles[2], here labeled 40NP and 230NP, were synthesized from a 20% benzocyclobutene functionalized linear polystyrene prepared by Brooke Van Horn according to a method present here [2]. Tightly crosslinked nanoparticles were prepared in the following manner a dilute suspension (1 mg/mL) of the linear precursor in benzyl ether is dripped into a nitrogen padded bath of vigorously stirring benzyl ether at 250 °C. Under these conditions the linear precursor will intramolecularly crosslink. Benzyl ether is distilled off from the suspension until approximately 10 mL remains. This suspension is precipitated into a 10X volume of stirring methanol. After settling overnight the solids are separated from the suspensions via a polyamide membrane ($0.2\mu m$ pore diameter) and resuspended in THF and precipitated again in methanol. This process is repeated 3 times in total before the purified solids are transferred to a vacuum oven at 40 °C for at least 1 week to drive off all of the solvent and non-solvent. The size of synthesized nanoparticles were characterized using light scattering on a Protein Solution Dynapro dynamic light scattering unit (now a division of Wyatt). Intensity fluctuations in the light scattered from the diffusing particles are related to the particle diffusion coefficient. A hydrodynamic radius is reported, calculated from the Stokes-Einstein relationship $D = \frac{k_B T}{6\pi\eta_{solv} R_h}$[44, 45].

Blends of 75 kD and 393 kD linear polystyrene were prepared in 25 v% increments from 0 to 100 with and without 40 kD and 230 kD tightly cross linked polystyrene nanoparticles[2]. All blends were prepared by suspending solids in tetrahydrofuran (THF), a good solvent, at 10 mg/mL overnight and precipitating into 10X volume of vigorously stirred methanol, a nonsolvent. The solutions were added drop-wise via a separation flask into the methanol. White precipitates formed immediately. Slurries were left to settle overnight before excess methanol was removed from the top via a vacuum apparatus. Remaining solvent-nonsolvent was evaporated off under ambient conditions overnight before placing the solids in a vacuum oven at 40 °C for more than one week.

Dried powder was placed into a 8-mm vacuum press under 0.4 kN at 130 °C for 15min then 0+ kN at 170 °C for 1.75 hours ($> 10\tau_d$[46]). Disks were then placed in the vacuum oven overnight. Rheological experiments were conducted on a strain controlled ARES-G2 rheometer. 8mm parallel plates were heated to 150 °C for 30 minutes then zeroed. Samples were loaded on hot plates. The plates are closed to 1.0 N and heated to 180 °C to adhere the disk to the plates. The temperature was then dropped to 150 °C under auto compression to maintain good contact. The system was then equilibrated for 20 minutes before starting a test. A strain sweep was conducted to determine the linear viscoelastic region which ends around 8% strain. Frequency-temperature sweeps were run from 150 to 210 °C in 20 °C increments. For temperatures below 210 °C, the frequency sweep ran from 100 to 1 rad/s, at 210 °C the frequency range was extended down to 0.1 rad/s. A constant gap was maintained by the thermal compensation control with a thermal coefficient of expansion of 2.6μm/°C. Boltzmann Time-temperature superposition[30] is used to shift frequency sweeps from different temperature into a single master curve with a reference temperature of 170

$^{\circ}$C.

The terminal viscosity is reported from a fit of the Carreau-Yasuda Model ($\eta(\dot{\gamma}) = \eta_0 [1 + (\lambda\dot{\gamma})^a]^{\frac{n-1}{a}}$)[6, 7] after converting the oscillatory shear data into steady shear data using the Cox-Merz Rule ($\eta(\dot{\gamma} = \omega) = |\eta * |(\omega))$[7, 8]. The plateau modulus is determined using the MIN method[47] where the value of the storage modulus at the minimum of Tan(δ) is reported,

($G^0_{Nexp} = G'(\omega)_{tan(\delta)\rightarrow minimum}$).

2.2 Results & Discussion

As noted earlier it is generally understood the viscosity ratio (η_r, blend viscosity/neat viscosity) increases linearly with the volume fraction of filler added, as shown in Einstein's relation[4] $\eta_r = 1 + 1.5\phi + 6.2\phi^2$ with Batchelor correction[5] for $\phi > 2\%$. Consequently the magnitude of change in viscosity will scale with the viscosity of suspending fluid. At constant volume fraction filler (constant increase in viscosity ratio) the magnitude of viscosity increase will be larger for a high viscosity fluid compared to a low viscosity fluid. The same should hold true for polymer nanocomposites with reduced viscosity found in the literature.[19, 29]

By blending 75PS and 393PS we were able to create a controlled bidisperse blend that captures the range of chain sizes and polydispersity present in commercial polymers. From Table 2.1, we see the polydispersity index (PDI) of the bidisperse blends range from 1.24 to 1.68, which compares well with the 1.5 PDI of commercial polystyrenes. From the molecular weight distribution (MWD), Figures 2.1 & 2.2, we can also determine what chains are confined and therefore are capable of exhibiting a reduced viscosity. In order to achieve confinement the interparticle half-gap, h, must be less than the R_g of the suspending chains.

Table 2.1: M_n, M_w and PDI of neat bidisperse PS blends from GPC. PDIs are similar to those of commercially available polystyrenes, 1.5.

Sample	M_n (kD)	M_w (kD)	PDI
75PS	79.7 ($2.6M_c$)	85.2	1.07
25v% 393PS	140	235	1.68
50v% 393PS	205	305	1.49
75v% 393PS	280	347	1.24
393PS	341 ($11.6M_c$)	361	1.06

In Figures 2.1 & 2.2 we show the molecular weight distribution (MWD) for all of the bidisperse blends as determined by GPC. The vertical lines indicate the smallest chain confined for a given volume fraction and size of nanoparticle, see Table 2.2, equal to those used in this study. This means any chains higher in molecular weight than the vertical line will be confined by that nanoparticle size at that volume fraction. From Figure 2.1 one can see 2.0 v% of the 230 kD tightly crosslinked polystyrene nanoparticles (230NP)[2] will confine almost all of the 393PS, leaving the 75PS unconfined. 5.0 v% 230NPs will confine all of the 393PS and 1/4 of the 75PS. Moving to 8.5 v% 230NP will again confine all of the 393PS and all of the 75PS. Due to the smaller size of the 40 kD tightly crosslinked polystyrene nanoparticles[2] (40NP) they will confine significantly smaller chains at the same volume fraction of 230NP. This equates to needing fewer nanoparticles to confine a particular chain length. Again looking at Figure 2.2 the 2.0 v% 40NP line suggests all of the 393PS leaving 1/4 of the 75PS unconfined. As the volume fraction of 40NP is increased to 4.7 v% all the chains should be confined. In Tables 2.1 and 2.2 we show the number and weight average molecular weights and polydispersity for the bidisperse blends and polystyrene nanoparticles, respectively. Included in Table 2.2 are the radii of the nanoparticles used in this study.

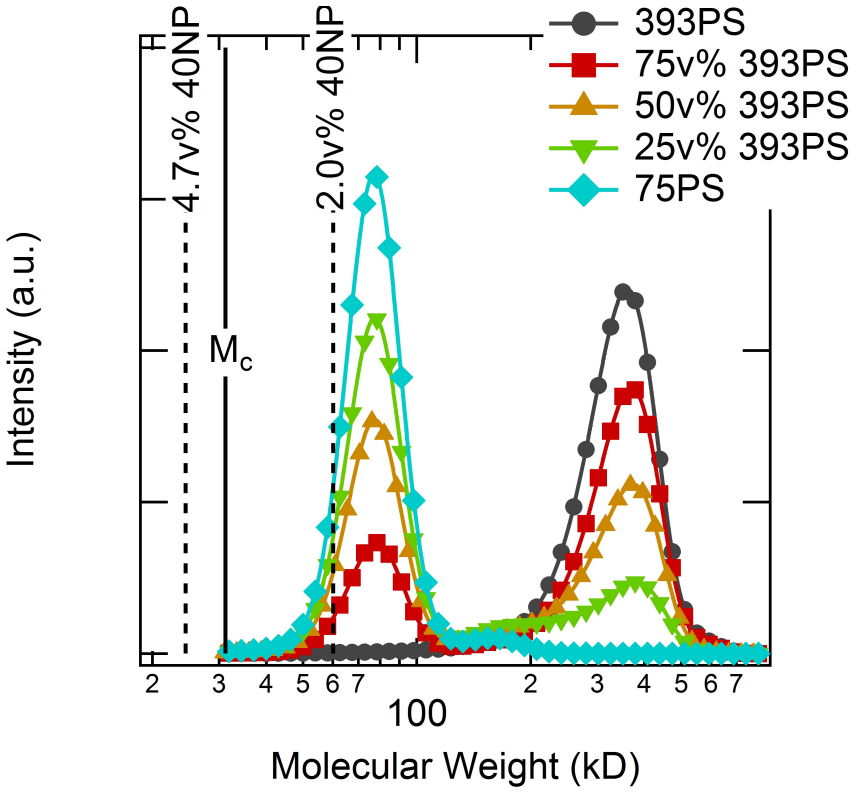

Figure 2.1: Molecular weight distribution of bidisperse linear polystyrene blends as determined by GPC. The dashed vertical lines indicate the smallest chain confined by a given volume fraction of 40 kD tightly crosslinked polystyrene nanoparticles[2]. The critical molecular weight for entanglement M_c is also noted, solid vertical line. For interpretation of the references to color in this and all other figures, the reader is referred to the electronic version of this dissertation.

Table 2.2: M_n, M_w, PDI and radius of PS nanoparticles. *Radius based on bulk density of polystyrene (1.04 g/cm^3). $^\dagger R_h$ DLS in toluene at 30 °C. $^\ddagger R_g$ SANS in 120 kD perdeuterated polystyrene (120dPS) at 170 °C. ††230NP particles were agglomerated in SANS study, R_h in d-cyclohexane is reported instead.[1]

Sample	M_n (kD) kD	M_w (kD) kD	PDI	$^\star a$ (nm) nm	$^\dagger R_h$ (nm) nm	$^\ddagger R_g$ (nm) nm
40NP	36.5	37.1	1.02	2.4	3.0	2.8
230NP	231	248	1.08	4.4	7.2	††5.9

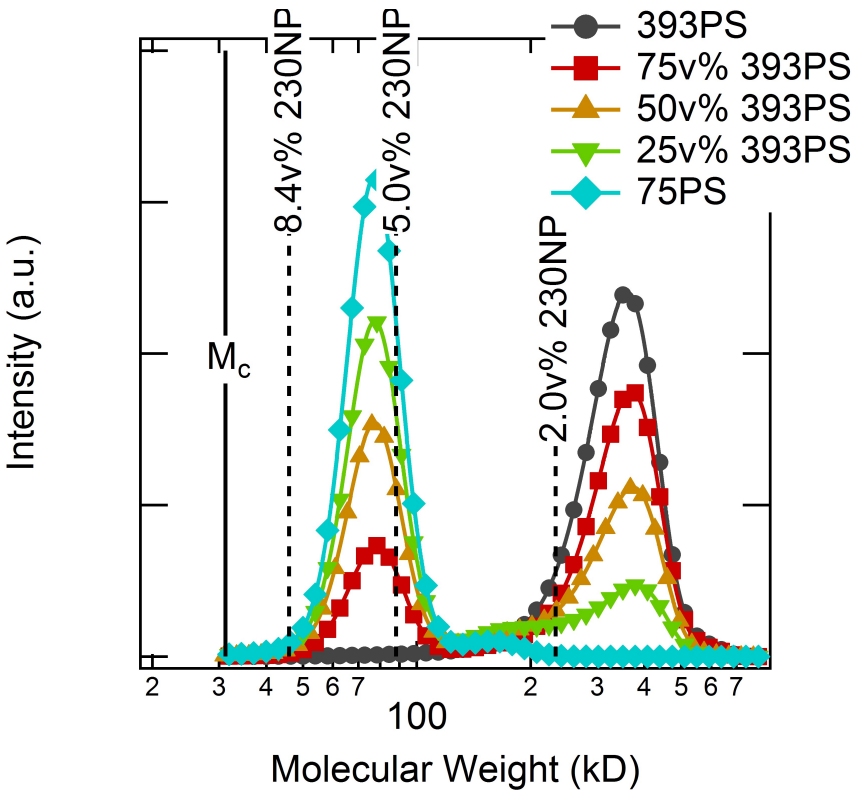

Figure 2.2: Molecular weight distribution of bidisperse linear polystyrene blends as determined by GPC. The dashed vertical lines indicate the smallest chain confined by a given volume fraction of 230 kD tightly crosslinked polystyrene nanoparticles[2]. The critical molecular weight for entanglement M_C is also noted, solid vertical line.

2.2.1 Bidisperse Blends - 40NP

In Figure 2.3, we show the terminal viscosity ratios (calculated by fitting the Carreau-Yasuda Model) for bimodal blends with two concentrations of 40NP, 2.0 v% and 4.7 v%. Focusing on blends with 2.0 v% 40NP, we see that the viscosity increases for 75PS which is not unexpected since a portion of the chains are unconfined ($h > R_g$). 2.0 v% 40NP in 393PS has a large viscosity decrease, also not unexpected since all of the chains are confined in this system ($h < R_g$). If we look at the bidisperse blends, we see that as 393PS content is added, the reduced viscosity ratio becomes larger. From these five points, it is clear that high molecular weight content receives the most benefit from reduced viscosity by nanoparticle addition. 50 v% 393PS has a PDI of 1.5, similar to commercial blends, and the nanocomposite created with this bidisperse blend has a slight reduced viscosity. We are confident that the reduced viscosity effect of nanoparticles will be useful in commercial polymers and the effect will be more pronounced with higher molecular weight materials. The data point for 75PS +4.7 v% 40NP is not included since pressed disks continually cracked before rheological measurements could be preformed. Although all chains would be confined the viscosity ratios for the 4.7 v% 40NP blends are not as impressive as the 2.0 v% 40NP blends. We suspect that the nanoparticles at this high loading are on the verge of phase separation.

The viscosity ratios for 2.0 v% 40NP bidisperse blends that exhibit a reduced viscosity in Figure 2.3 are listed in Table 2.3. The change in terminal viscosity is also listed to highlight the magnitude of the reduced viscosity in high molecular weight blends. Not only is the magnitude higher due to the higher viscosity of the suspending matrix but the decrease in the ratio of the terminal viscosity is also larger. Since a higher molecular weight material has a larger difference between the Rouse regime and the entangled polymer limit the viscosity

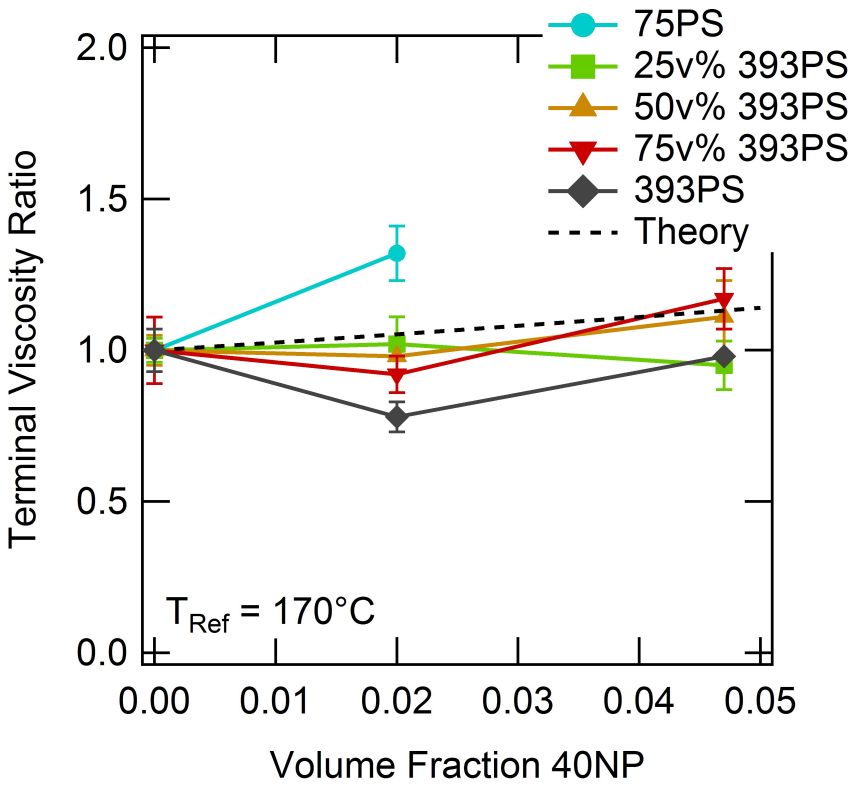

Figure 2.3: Terminal viscosity ratios (η_r^0) of linear bimodal blends with 40 kD tightly crosslinked polystyrene nanoparticles[2] (40NP). Theory line indicates the Einstein prediction[4] with the Batchelor correction[5] ($\eta_r = 1 + 2.5\phi + 6.2\phi^2$). As the fraction of high molecular weight linear chains (393PS) is increased the melt viscosity moves to a reduced value. Terminal viscosities are reported as the η^0 parameter from a fit of the Carreau-Yasuda Model[6, 7] following conversion of the complex viscosity to steady shear using the Cox-Merz Rule[7, 8]. Complex viscosity and moduli master curves for these systems are available in Appendix A. All data shifted to a reference temperature of 170 °C.

Table 2.3: Terminal viscosity ratios (η_r^0) and change in terminal viscosities ($\Delta\eta^0$) of bimodal linear polystyrene and 2 v% 40 kD tightly crosslinked polystyrene nanoparticles[2] (40NP). As volume fraction of confined chains increases the viscosity reduction increases.

Sample	η_r^0	$\Delta\eta^0$ (Pa-s)
75PS	1.33	+1300
25 v% 393PS	1.12	+4600
50 v% 393PS	0.98	-4000
75 v% 393PS	0.92	-38000
393PS	0.78	-250000

drop can be and is significantly larger.

Industrial equipment operates at shear rates in the $10^2 - 10^3 s^{-1}$ so it is important to demonstrate the viscosity reduction occurs at all frequencies. By employing the Cox-Merz Rule[8, 7] $\eta(\dot{\gamma} = \omega) = |\eta * |(\omega)$, a valid assumption for polystyrene, we can assume the oscillatory response is the same as the steady shear response. Table 2.4 lists the viscosity ratios for the 2.0 v% 40NP blends with a reduced viscosity at selected frequencies. The reduced viscosity is present in significant magnitude at all frequencies although the effect is lessened further from the terminal region. Where the frequency/shear rate is approaching the diffusion rate of the nanoparticles. These reductions are more substantial considering standard fillers at this volume fraction would produce an increase of at least 5 %, a ratio of 1.05. By using well dispersed nanoparticles instead of traditional fillers new properties can be incorporated into polymers and processibility can be improved through reduced viscosity.

2.2.2 Bidisperse Blends - 230NP

The 230NP nanoparticles are very close in size to the 75PS chains, as such they approach the solubility limit for nanoparticles in a polymer matrix.[20] As high molecular weight content

Table 2.4: Complex viscosity ratios ($\eta_r^*(\omega)$) for 2.0 v% 40NP blends with reduced viscosity at selected frequencies. Again the highest viscosity material has the largest reduced viscosity, however even the 75 v% 393 bimodal blend has a reduced viscosity at industrially relevant frequencies.

Sample $\omega =$	η_r^* $10^1 \frac{rads}{s}$	η_r^* $10^2 \frac{rads}{s}$	η_r^* $10^3 \frac{rads}{s}$
50 v% 393PS	0.99	0.99	1.00
75 v% 393PS	0.92	0.89	0.91
393PS	0.91	0.93	0.95

is added, these nanoparticles should become more soluble. In Figure 2.4 we again show terminal viscosity ratios, this time for three volume fractions of 230NP; 2.0 v%, 5.0 v% and 8.5 v%. In general, most of the blends that contained 75PS and 230NP have an increase in viscosity close to that of Einstein's relation. The 393PS blended with 230NP resulted in a steady decrease in viscosity as more nanoparticles were added, Figure 2.4. For the 393PS sample the 230NP are significantly smaller than the R_g of the chains making them more soluble. The increase that was present in all bidisperse blends with 75PS and pure 75PS with 230NP shows the solubility of the nanoparticles is independent of the number of small chains present, at least at the volume fractions of 75PS studied. From this experiment we can conclude that in order to make a nanocomposite with reduced viscosity the nanoparticles should be significantly smaller than any chain present in the suspending polymer.

2.3 Polydisperse Systems

Part of the purpose of this experimental set was the determine the industrial feasibly of nanocomposite melts with reduced viscosity. BASF was kind enough to provide us with a polydisperse linear chain (SAN) ($M_w = 197\ kD$, PDI = 1.5) and a polydisperse crosslinked

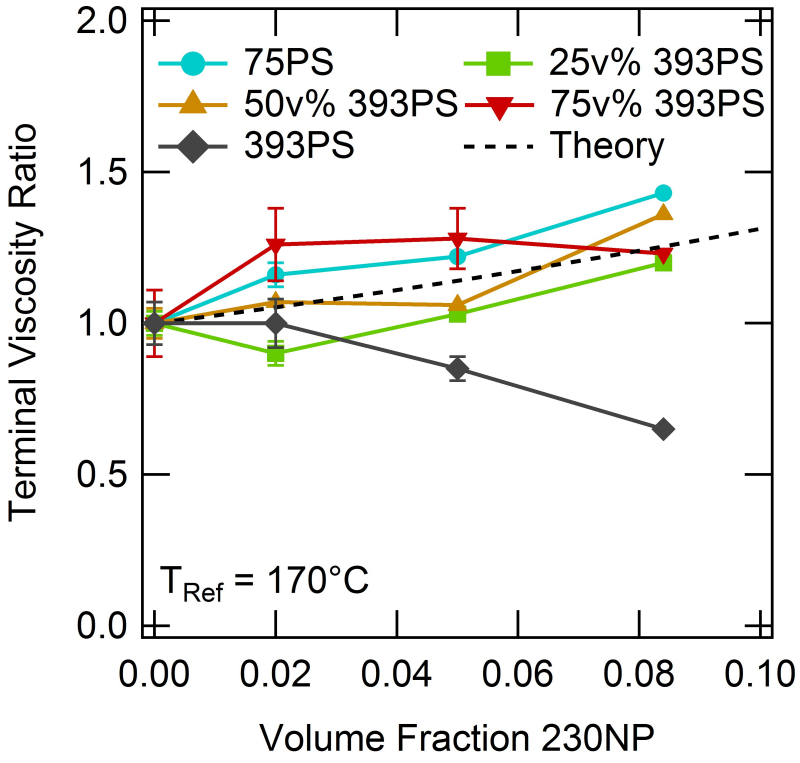

Figure 2.4: Terminal viscosity ratios of bimodal linear polystyrene with 230 kD tightly crosslinked polystyrene nanoparticles[2] (230NP). Theory line indicates the Einstein prediction[4] with the Batchelor correction[5] ($\eta_r = 1 + 2.5\phi + 6.2\phi^2$). All nanocomposites with 75PS and 230NP essentially behave as Einstein predict which indicates the nanoparticles are phase separated. Terminal viscosities are reported as the η^0 parameter from a fit of the Carreau-Yasuda Model[6, 7] following conversion of the complex viscosity to steady shear using the Cox-Merz Rule[7, 8]. Terminal viscosity ratios with 8.5 v% 230NP blends with any v% of 75PS are extrapolated. Complex viscosity and moduli master curves for these systems are available in Appendix A. All data shifted to a reference temperature of 170 °C.

nanoparticle ($R_h = 1 - 3\ nm$) (SAN-NP). These systems were prepared and characterized in the same manner as the previous systems, with the exception of methyl ethyl ketone (2-butanone) being used as the solvent. In Figure 2.5 we show the viscosity ratios in the terminal region and at high frequency. Also included in the figure are some comparisons to blending rules assuming the volume added has a viscosity of 0, for the sake of calculating the actual value 1×10^{-36} Pa-s was used. For the simple blending case, labeled simple, the viscosity was calculated by a volumetric average Equation (2.3). Tsenoglou's blending rule for linear polymer was also used, equation 2.4[48] where η_B is the blend viscosity, $v_{i,j}$ is the volume of the component, and $\eta_{i,j}$ is the viscosity of the component. Both cases are presented to show how the nanoparticle reduction cannot be described by a simple blending even assuming the viscosity of the nanoparticle is zero which would never be the case. Interestingly enough the decrease at high frequency is fairly well captured by the decrease in plateau modulus.

$$\eta_{blend} = \eta_{polymer}\phi_{polymer} + \eta_{nanoparticle}\phi_{nanoparticle} \tag{2.3}$$

$$\eta_B = 2\sum_{i=1}^{n}\sum_{j=1}^{n} v_i v_j \frac{\eta_i \eta_j}{\eta_i + \eta_j} \tag{2.4}$$

2.4 Summary

In this work we clearly see two different failures of the nanocomposite melts with reduced viscosity. We will begin our discussion by addressing the results with 230 kD tightly crosslinked polystyrene nanoparticles[2] (230NP). Tuteja and Mackay[20] have already postulated the favorable and unfavorable energies that drive or in this case prevent the dispersion of nanopar-

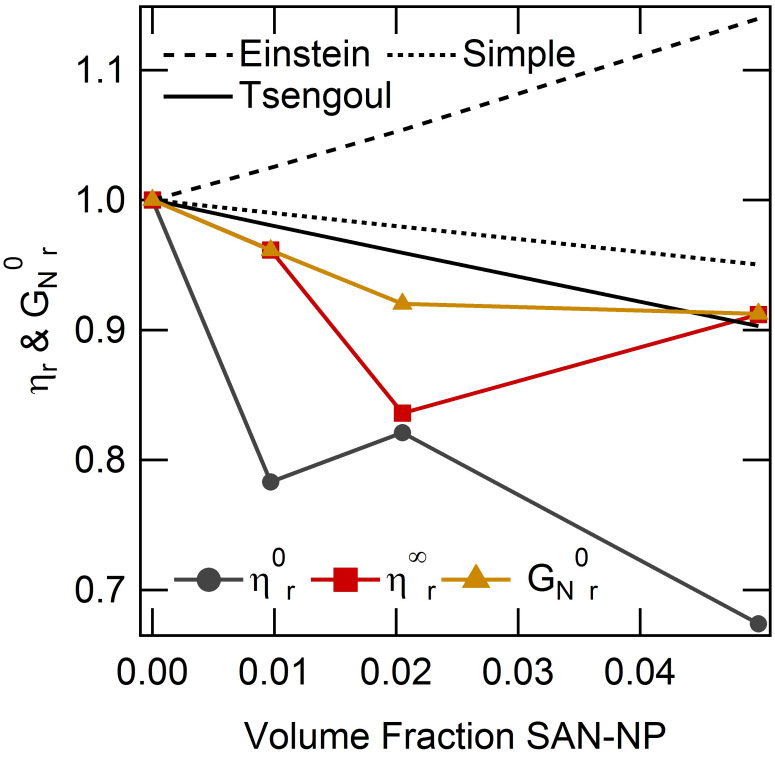

Figure 2.5: Terminal viscosity ratios and plateau modulus ratios of poly(styrene-co-acrylonitrile) with crosslinked poly(styrene-co-acrylonitrile) nanoparticles. Theory line indicates the Einstein prediction[4] with the Batchelor correction[5] ($\eta_r = 1 + 2.5\phi + 6.2\phi^2$). Simple Equation (2.3) and Tsenoglou (Equation 2.4) indicate results based on blending with a volume of material with essentially zero viscosity. The ratio of G^0_N is also included while it captures most of the decrease at high frequency it does not account for the large decrease a low frequency, which is typical of these nanocomposites. Terminal viscosities are reported as the η^0 parameter from a fit of the Carreau-Yasuda Model[6, 7] following conversion of the complex viscosity to steady shear using the Cox-Merz Rule[7, 8]. Terminal viscosity ratios with 8.5 v% 230NP blends with any v% of 75PS are extrapolated. Complex viscosity and moduli master curves for these systems are available in Appendix B. All data shifted to a reference temperature of 170 °C.

ticles in linear polymer. Keeping the nanoparticles dispersed results in a favorable energy gain by increasing molecular contacts[49] that would otherwise be unavailable to the system in an agglomerated case. However, there is a penalty associated with the dispersion of nanoparticles, physically this is due to the chains stretching[22, 23, 24, 25, 26, 27, 28] to accept the nanoparticles resulting in an entropic loss to the chains[50, 51]. This penalty scales with $(a/R_g)^3$[20] based on stretching of polymer brushes[33, 51], which obviously becomes very large as the nanoparticle radius (a) approaches the polymer chain length (R_g). This explains the phase separation we see in the bimodal blends with 230NP. Since the 75 kD linear polystyrene (75PS) and the 230 kD tightly crosslinked polystyrene nanoparticles[2] (230NP) are approximately the same size the benefit of dispersion is outweighed by the penalty incurred by stretching[22, 23, 24, 25, 26, 27, 28] around such a large (relative to the chain) nanoparticle. One would expect that as the average molecular weight of the suspending chains is increased a nanoparticle at a fixed radius would become more soluble and therefor more likely to produce a viscosity decrease. At the two extremes (monodisperse chains) only 75 kD linear polystyrene (75PS) and only 393 kD linear polystyrene (393PS) blended with 230NP this holds quite true. The monodisperse 393 kD linear polystyrene (393PS) has a reduced viscosity at all volume fractions of 230NP and mondisperse 75 kD linear polystyrene (75PS) has an increase a all volume fractions of 230NP. Which is not much of a surprise, the 230NPs are soluble in the high molecular weight content (393PS) and insoluble in the low molecular weight content (75PS). However, the viscosity of the 75% 393PS bimodal blend with 230NP shows a very large increase in viscosity, higher than that off all other systems. And unlike the bimodal blends with 40 kD tightly crosslinked polystyrene nanoparticle[2] (40NP) the viscosity decrease does not correspond to the volume fraction of low molecular

weight chains. Specifically the 25% and 75% 393PS polystyrene systems appear to be flipped in this respect.

Moving to the smaller nanoparticle system we see the sensitivity to the confinement limit even with a small number of unconfined chains. Looking at the results for the bimodal blends with 40 kD tightly crosslinked polystyrene nanoparticles[2] (40NP) there is only a small volume fraction of unconfined chains yet they have a strong influence on the viscosity. There is little theoretical reasoning for why confinement is so important or why it should scale with the R_g (M_w). However, there is a significant amount of experimental data[19, 20, 29] in the literature and in this work showing the limit of $h < R_g$ being quite important to the viscosity reduction. The results suggest an equilibrium state where only the larger chains are swollen and the smaller chains are unaffected by the nanoparticles resulting in the classic increase in viscosity[9, 10, 11, 12]. We can again turn to Tsenoglou's blending rule[48] and we find that while it over predicts the blend viscosity for the intermediate bimodal blends with 2.0v% nanoparticles it does so no worse than what would be calculated for the neat bimodal systems. Since Tsenoglou's relationship is based on the relaxation time of the blended chains it should be a valid approximation for the viscosity as it would for a linear-linear bimodal blend. In either case, the neat system or the nanocomposite, polydispersity of the chains will effect the prediction leading to the discrepancy between the prediction and the actual blended viscosities. Still only a small volume fraction of the 75PS chains are unconfined, even in the pure 75PS case.

Finally looking at the polydisperse systems we see the results are quite promising for industrial applications, this particular size of nanoparticle is above the confinement limit and small enough to be soluble in the suspending chains. The viscosity reduction is still

present even at high frequency though that decrease correlates to the decrease in plateau modulus and can almost be described by using Tsenoglou's blending rule for a material with zero viscosity.

From this work we conclude that the minimum amount of nanoparticles required for a viscosity drop does not need to be calculated solely on the smallest chain present. However there is no appropriate limit that can be determined form this experimental set. It was also observed that blends made with nanoparticle which are of similar size to the polymer matrix will not give favorable results. In general the best results can be obtained with long chains and small nanoparticles. Under these conditions only a small volume of nanoparticles would be required to achieve a decrease in the terminal viscosity limiting the likelihood of phase separation.

Chapter 3

Dispersion and Mixing Energy of Ideal Systems

3.1 Introduction

As nanoparticles are becoming available on a larger and more uniform scale, they are finding their way into composite materials: sometimes replacing contemporary colloidal sized particles since the nanoscale particles produce the same benefits, increased tensile strength and modulus, at lower loading in polyimide-clay composites.[52] Other composite materials rely on new functionality intrinsic to the nanoparticle such as conductivity.[53] In either case, the performance of the composite material is dependent on the dispersion of the nanoparticles. This is especially true for optical nanocomposite materials which rely on the particle being small enough to prevent light scattering[54]. If the nanoparticles cannot be dispersed or do not remain dispersed, the composite material will lose performance or functionality altogether. Understanding the thermodynamics governing nanoparticle suspension in polymeric systems is critical for these nanocomposites.

We begin our study of nanoparticle dispersion by looking at the size relationship between the nanoparticles and suspending polymer. It has been shown that when the suspended particle becomes smaller than the suspending chain the melt viscosity of the composite decreases[19, 18, 55] contrary to well established results and theory from larger particle suspensions.[10] Suspensions of well dispersed nanoparticles in a polymer matrix have been shown to produce other unusual material properties; faster than expected diffusion of the nanoparticle [21] and good-solvent-like chain swelling[27].

The dispersant phase of many polymer-nanocomposites are comprised of inorganic materials with a surface coating to make them compatible with polymers and/or organic solvent.[56] Inorganic nanoparticles can be synthesized in large quantities in uniform sizes[57, 58, 59] and the chemistry for attaching organic solubilizing groups is well understood.[14, 60]

Unfortunately, inorganic nanoparticles are chemically different from the suspending polymer complicating the forces present by introducing attractions or repulsions based on the chemistry at the surface and the polymer matrix. This chemical disparity can lead to phase separation[61, 62, 63] and/or agglomeration of nanoparticles into larger clusters. By using organic nanoparticles, specifically tightly crosslinked polystyrene nanoparticles[2], in a polymer matrix, again polystyrene, an refractive index match ideal system[11, 64] is created where size and shape dominate the polymer and nanoparticle arrangement (packing).

Scattering has long been used to determine interparticle forces by measuring the Second Virial Coefficient of dilute concentrations of suspended particles.[65, 66, 67] We can also measure the particle size and molecular weight using the appropriate analysis. While the crosslinked polystyrene nanoparticle polystyrene polymer system is ideal, measuring the morphology is complicated by a lack of contrast between the two components. With comparable chemical structures and density the optical, X-ray, and electron contrast are minimal. However, perdeuterated monodisperse linear polymer has a large neutron contrast with respect to the hydrogen rich nanoparticles. Making neutron scattering an excellent method to study this ideal system.

3.2 Experimental Methods

120 kD perdeuterated linear monodisperse polystyrene (Polymer Source, Inc; Montreal, QC, Canada) was used as received, here referred to as 120dPS. The as received material was run through the GPC to confirm molecular weight and distribution, compared against a 5 point polystyrene standard, M_n = 122 kD and M_w = 130 kD. NMR was used to confirm deuteration, compared against a protonated chain of similar M_w.

40 kD and 230 kD tightly crosslinked polystyrene nanoparticles[2] were synthesized from a 20% benzocyclobutene functionalized linear polystyrene prepared by Brooke Van Horn according to a method present here[2]. Tightly crosslinked nanoparticles[2] were prepared in the following manner a dilute suspension (1 mg/mL) of the linear precursor in benzyl ether is dripped into a nitrogen padded bath of vigorously stirring benzyl ether at 250 °C. Under these conditions the linear precursor will intramolecularly crosslink with minimal intermolecular side reactions. Benzyl ether is distilled off from the suspension until 10 mL remains. This suspension is precipitated into a 10X volume of stirring methanol. After settling overnight the solids are separated from the suspensions via a polyamide membrane ($0.2\mu m$ pore diameter) and resuspended in THF and precipitated again in methanol. This process is repeated 3 times in total before the purified solids are transferred to a vacuum oven at 40 °C for at least 1 week to drive off all of the solvent and non-solvent. The size of synthesized nanoparticles were characterized using dynamic light scattering (DLS) on a Protein Solution Dynapro dynamic light scattering unit (now a division of Wyatt). Intensity fluctuations in the light scattered from the diffusing particles is related to the particle diffusion coefficient. A hydrodynamic radius is reported, calculated from the Stokes-Einstein relationship $D = \frac{k_B T}{6\pi\eta_{solv} R_h}$[44, 45].

Blends of 40 kD and 230 kD tightly crosslinked polystyrene nanoparticles[2] (40NP and 230NP) and 120 kD linear perdeuterated polystyrene standard (120dPS) are prepared by rapid precipitation. An appropriate mass of nanoparticle and deuterated polymer are dispersed in a good solvent tetrahydrofuran (THF) at a concentration of 10 mg/mL. The suspension is left on a rocking mixer for several days to ensure the polymer is suspended properly. Each suspension is sonicated for 60 minutes to ensure the nanoparticles are well

dispersed. Following sonication each suspension is precipitated into a 10X volume of stirring methanol. Solids are immediately separated via a polyamide membrane ($0.2\mu m$ pore diameter) in a Büchner funnel - vacuum flask apparatus with a water aspirator. The semi-dried solids are then rinsed with methanol and transfered to a vacuum oven at 40 °C at for at least one week to ensure all solvent and non-solvent is removed.

Disks for rheology are prepared by placing dried powder into an 8-mm vacuum press under slight pressure at 170 °C for 60 minutes ($> 10\tau_d$[46]).

Disks for SANS are prepared by placing dried powder into an 8-mm vacuum press under slight pressure at 170 °C for 15 minutes. Disks were then loaded into Al washers and into scattering cells where they were annealed in a vacuum oven for 45min at 170 °C before being loaded into the neutron beam line sample chamber.

Rheological experiments were conducted on a strain controlled ARES-G2 rheometer. 8-mm parallel plates were heated to 130 °C for 60 minutes then zeroed. Samples were loaded on hot plates. Plates are closed to 1 N and heated to 170 °C to adhere the disk to the plates. The temperature was then dropped to 130 °C under auto compression to maintain good contact. The system was then equilibrated for 30 minutes before starting a test. A strain sweep was conducted to determine the linear viscoelastic region which ends around 8% strain. Frequency-temperature sweeps were run from 100 to 0.1 rad/s and 130 to 190 °C in 20 °C increments. A constant gap was maintained by the thermal compensation control with a thermal coefficient of expansion of 2.6 μm/°C. Boltzmann Time-temperature superposition[30] is used to shift frequency sweeps from different temperature into a single master curve with a reference temperature of 170 °C.

Small angle neutron scattering (SANS) measurements were carried out using the 30-

m NG-3 SANS instrument at the National Institute of Standards and Technology (NIST), Center for Neutron Research (NCNR) in Gaithersburg, MD. Two instrument configurations were used for nanocomposites with 40 kD tightly crosslinked polystyrene nanoparticles[2] (40NP). The first configuration had a sample to detector distance of 133 cm with a 20 cm detector offset, 8 beam guides, and 6 Å wavelength, giving an expected scattering vector (q) range of 0.0304-0.4472 $Å^{-1}$. The second configuration had a sample to detector distance of 400 cm with a 0 cm detector offset, 5 beam guides, and 6 Å wavelength, giving an expected q range of 0.0086-0.1179 $Å^{-1}$. All the measurements were performed at 170 °C with a 1/4 inch aperture. Four instrument configurations were used for nanocomposites with 140 kD tightly crosslinked polystyrene nanoparticles[2] (230NP). The first configuration had a sample to detector distance of 133 cm with a 20 cm detector offset, 8 beam guides, and 6 Å wavelength, giving an expected scattering vector (q) range of 0.0304-0.4472 $Å^{-1}$. The second configuration had a sample to detector distance of 400 cm with a 0 cm detector offset, 5 beam guides, and 6 Å wavelength, giving an expected q range of 0.0086-0.1179 $Å^{-1}$. The third configuration had a sample to detector distance of 1317 cm with 0 cm offset, 2 beam guides, and 6 Å wavelength, giving an expected q range of 0.0046-0.0360 $Å^{-1}$. The fourth configuration had a sample to detector distance of 1317 cm with 0 cm offset, 0 beam guides, and 8 Å wavelength, giving an expected q range of 0.0010-0.0257 $Å^{-1}$. Experiments were performed at 170 °C and 127 °C with a 1/4 inch aperture. Data reduction and analysis of the data was done using the SANS and USANS Data Reduction and Analysis software provided freely by the NCNR at NIST.[68]

3.3 Results & Discussion

3.3.1 120dPS-40NP

In Figure 3.1 we show the terminal viscosity ratios for 120 kD perdeuterated linear polystyrene (120dPS) with four volume fractions of 40 kD tightly crosslinked polystyrene nanoparticles[2] (40NP). The addition of crosslinked polystyrene nanoparticles reduces the melt viscosity, contrary to Einstein's[4] and others predictions and a large body of experiments with larger particles.[10] This reduction in viscosity is consistent with prior studies[20, 29, 55] of well dispersed nanoparticles with radii smaller than the radius of gyration ($a < R_g$) of the suspending polymer and enough nanoparticles are present to achieve confinement ($h < R_g$), 1v%, produces this effect.[20] Complete master curves for these composites are included at the end of the chapter, Figure 3.14.

In Figure 3.2 we show the one dimensional scattering profiles of four volume fractions of 40 kD tightly crosslinked polystyrene nanoparticles[2] (40NP) in 120 kD perdeuterated linear polystyrene (120dPS). The scattering intensity increases regularly with nanoparticle content, as expected, and the shape of scattering profile is consistent with particle-based systems with an incoherent background.

Kratky plots ($q^2I(q)$ vs q) made from the scattering profiles, Figure 3.3, exhibit a single peak centered at 0.07-0.08 Å that becomes more pronounced at higher volume fraction, which is indicative of particle like structure. In Table 3.1 the peak positions and characteristic length scales are reported.

Guinier plots, Figure 3.4, were constructed directly from the reduced SANS data taken at 170 °C and using Equation (3.1)[69, 70] the intensity at zero wavevector, I(0), and the

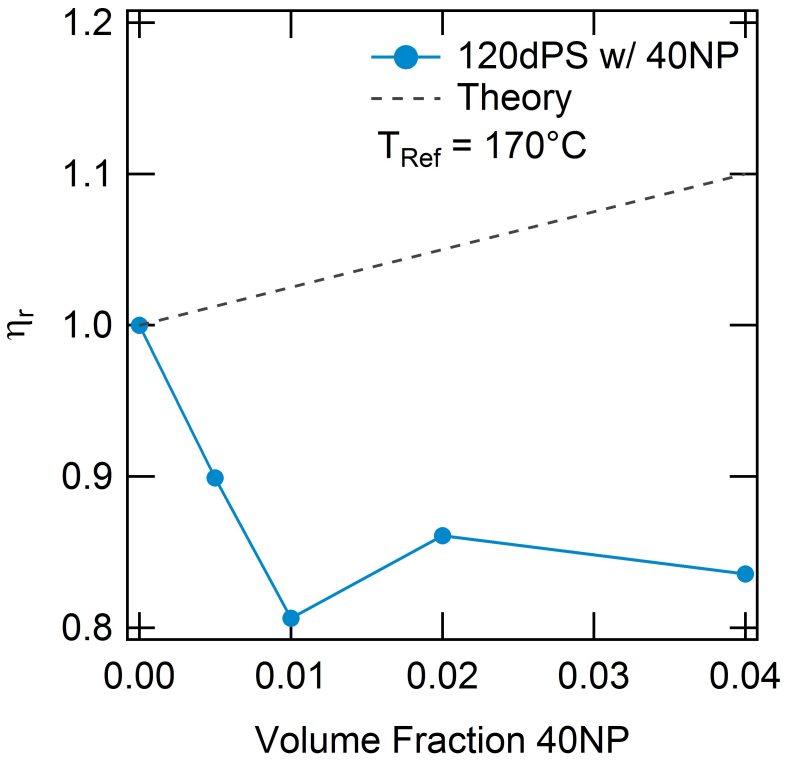

Figure 3.1: Terminal viscosity ratios (η_r^0) of 120 kD perdeuterated linear polystyrene (120dPS) with 4 volume fractions of 40 kD tightly crosslinked polystyrene nanoparticles[2] (40NP). Theory line indicates Einstein's relation[4] with Batchelor's correction[5] ($\eta_r = 1 + 2.5\phi + 6.2\phi^2$). The reduced viscosity typical of a well dispersed nanoparticle in a polymer melt is present. Terminal viscosities are reported as the η^0 parameter from a fit of the Carreau-Yasuda Model[6, 7] following conversion of the complex viscosity to steady shear using the Cox-Merz Rule[7, 8]. Complex viscosity and moduli master curves for these systems are available at the end of this chapter, Figure 3.14. All data shifted to a reference temperature of 170 °C.

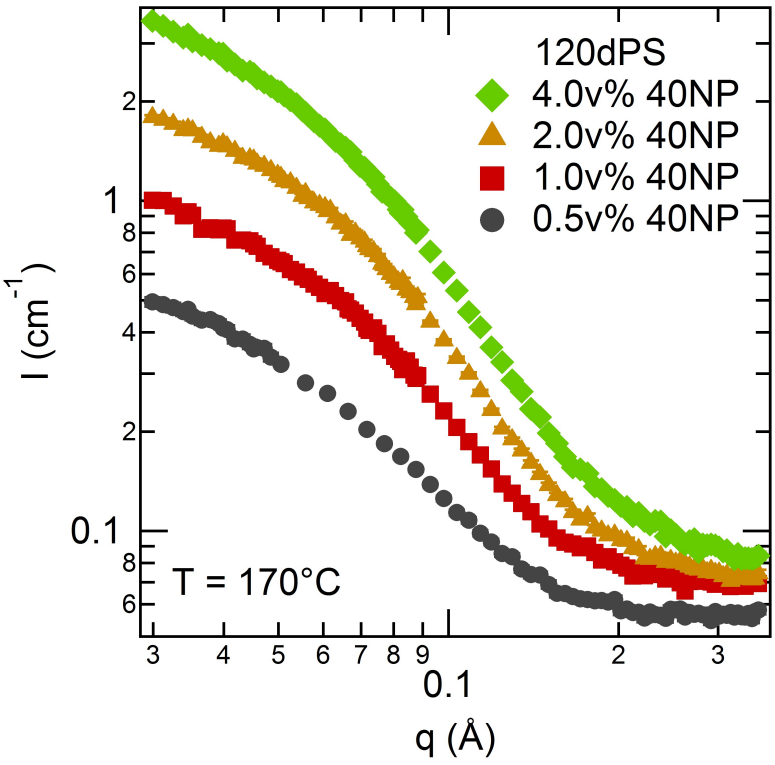

Figure 3.2: One dimensional neutron scattering profiles ($I(q)$ vs q) from the azimuthally averaged two dimensional scattering profiles of four volume fractions of 40kD tightly crosslinked polystyrene nanoparticles[2] (40NP) in 120 kD perdeuterated linear polystyrene (120dPS) at 170 °C. As expected the scattering intensity increases with increasing 40NP content and has the shape of a particle-like scatterer with incoherent background.

Table 3.1: Peak position from Gaussian fit to Kratky Plots (Figure 3.3) of four volume fractions of 40 kD tightly crosslinked polystyrene nanoparticles (40NP) in 120 kD perdeuterated linear polystyrene measured at 170 °C. Peak positions are constant regardless of volume fractions and the characteristic length scale (d)is approximately the same size as the R_h for these nanoparticles which is a good indication of dispersion.

Sample	Peak Position (Å^{-1})	Size $d = \frac{2.6}{q}$ (nm)
0.5v% 40NP	0.08127	3.2
1.0v% 40NP	0.08068	3.2
2.0v% 40NP	0.08004	3.2
4.0v% 40NP	0.07646	3.4

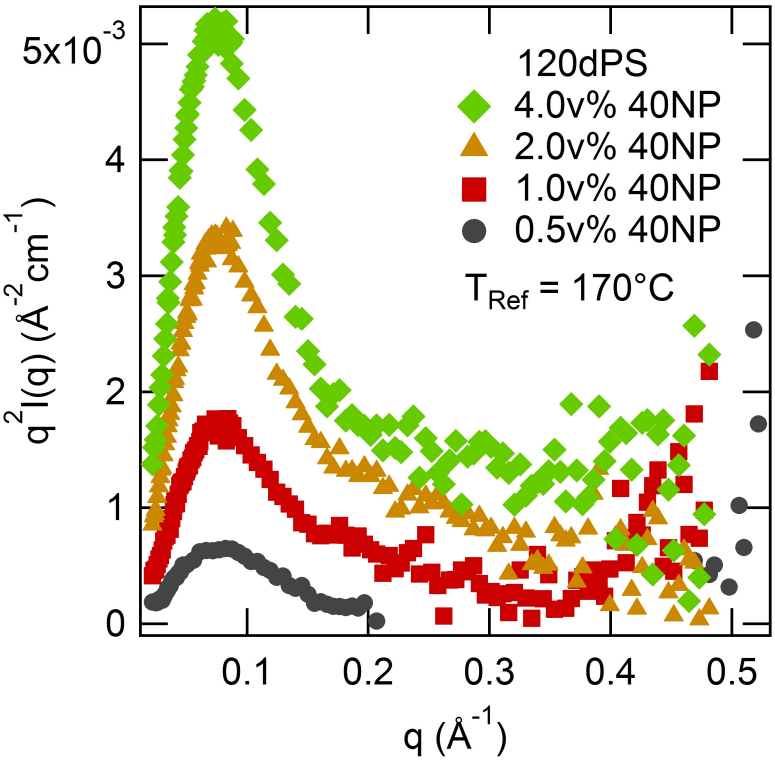

Figure 3.3: Kratky plots ($q^2I(q)$ vs q) constructed directly from the one dimensional scattering profiles of four volume fractions of 40 kD tightly crosslinked polystyrene nanoparticles (40NP) in 120 kD deuterated linear polystyrene (120PS) with the incoherent background subtracted. A peak in the Kratky plot indicates a particle like structure, which is expected for this system. Furthermore the peak positions are constant for all volume fractions.

Table 3.2: M_n, M_w, PDI (determined by GPC) and hydrodynamic radius (determined by DLS) of crosslinked polystyrene nanoparticles used in this work. Hydrodynamic radius determine by DLS in toluene at 30 °C.

Sample	M_n (kD)	M_w (kD)	PDI	R_h (nm)
40NP	36.5	37.1	1.02	3.0
230NP	231	248	1.08	7.2

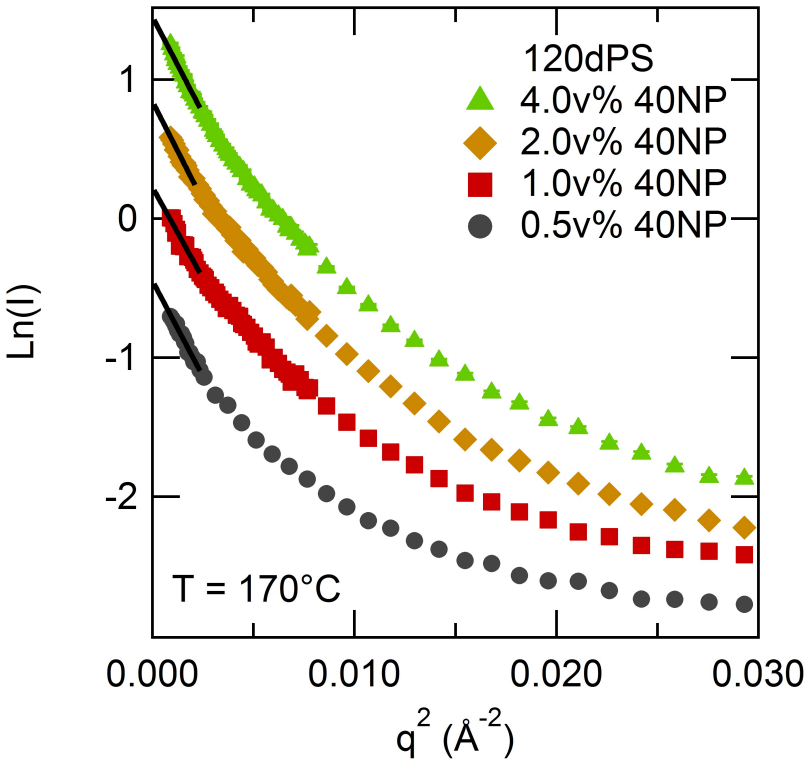

Figure 3.4: Guinier plots ($Ln(I(q))$ vs q) of the azimuthally averaged scattering profile from 4 volume fractions of 40 kD tightly crosslinked polystyrene nanoparticles[2] (40NP) in 120 kD perdeuterated linear polystyrene (120dPS). Solid lines indicate fits to Equation (3.1), fits ranged from $0.0009 < q^2 < 0.0025\text{Å}^{-2}$ and the radius of gyration and intensity at zero wavevector were determined. From the fits the average radius of gyration is 2.8 ± 0.1 nm indicating excellent dispersion. The results of the fits to the Equation (3.1) are listed in Table 3.3.

z-average radius of gyration ,$\langle R_g \rangle_z$, of the nanoparticles were determined and reported in Table 3.3.

$$I(q) = I(0)e^{\frac{-[qR_q]^2}{3}} \tag{3.1}$$

Using I(0) and the concentration of nanoparticles in the polymer matrix Virial plots were constructed, Figure 3.6. Using Equation (3.3.1)[65, 66, 69], the Second Virial Coefficient, A_2, was calculated from the slope and the weight average molecular weight, M_w, was determined from the intercept. The results are in excellent agreement with the literature[1] and

Table 3.3: Results of Guinier fits to scattering profiles of 40 kD tightly crosslinked polystyrene nanoparticles[2] (40NP) in 120 kD perdeuterated linear polystyrene (120dPS) at 170 °C. The radius of gyration is in excellent agreement with R_h and literature values[1]. The intensity at zero wavevector (I_0) will be used to determine solubility and mixing energy.

Sample	$I_0(cm^{-1})$	$\pm$	$\langle R_g \rangle_z$ (Å)	$\pm$
0.5v% 40NP	0.64	0.01	28.7	0.5
1.0v% 40NP	1.25	0.02	28.0	0.4
2.0v% 40NP	2.32	0.03	29.3	0.4
4.0v% 40NP	4.27	0.05	28.9	0.3

complimentary experiments, Table 3.2.

$$\frac{c}{I(0)} = K[1 + 2A_2 c M_w] \tag{3.2}$$

$$K = \frac{N_A}{M_w v^2 (\Delta\rho)^2)} \tag{3.3}$$

$$= \frac{M_w}{N_A V^2 (\Delta\rho)^2)} \tag{3.4}$$

From the Guinier fits, Figure 3.4 & Table 3.3, the R_g was calculated to be 2.8 ± 0.1 nm suggesting the nanoparticles are well dispersed since it would be much larger were the particles agglomerated. Also the R_g determined from SANS is very close to the hydrodynamic radius (R_h) of 3.0 nm determined by DLS in toluene (a good solvent), Table 3.2. Interestingly, using the M_n to calculate the particle radius, and assuming a density of 1 g/mL (a reasonable assumption), we find it to be 2.4 nm. This is smaller than the measured radius (a) assuming hard sphere behavior; $a = \sqrt{\frac{5}{3}} R_g = 3.6\ nm$ and results in a Buchard's P-ratio ($P^2 = R_g^2/R^2$) of 1.16 placing the density distribution between that of a uniform

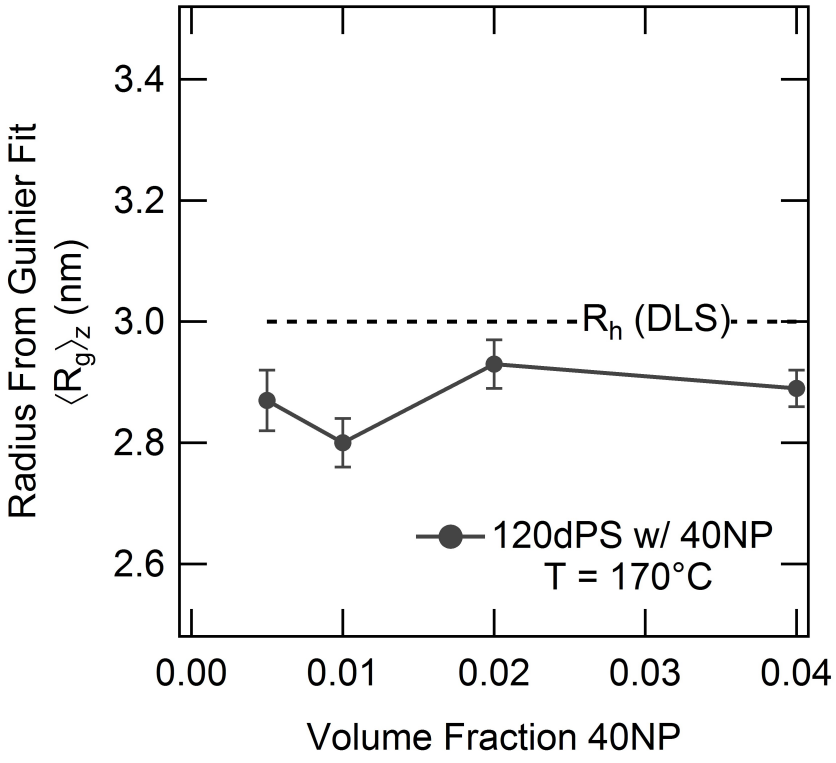

Figure 3.5: Radius from Guinier fit of 4 volume fractions of 40 kD tightly crosslinked polystyrene nanoparticles[2] (40NP) in 120 kD perdeuterated linear polystyrene (120dPS). The dashed line marks the hydrodynamic radius (R_h) determined by DLS, Table 3.2. The two radii are in excellent agreement and the SANS results indicate excellent dispersion.

sphere and a Gaussian chain.[71] So, the particles may be swollen in the melt state and do not behave as hard spheres. Note the particles could be agglomerated to increase the radius of gyration; however, the molecular weight should accordingly increase to a value in excess of 100 kD which is certainly not the case.

From the Virial plot, Figure 3.6, the M_w calculated from the intercept is $40.0 \pm 0.3\ kD$. Although a little higher, this value agrees with the weight average molecular weight 37.1 kD, determined for the linear precursor by GPC, as some dimerization may occur during the synthesis of the nanoparticles. A_2 calculated from the slope of the Virial Plot, Figure 3.6, is $(7.66 \pm 0.34)x \times 10^{-5}\ cm^3 mol/g^2$. A comparison of A_2 for a hard-sphere with the same radius and molecular weight calculated using the following equation, $A_2 = 16N_a a^3/3M^2$, was found to be $2.9 \times 10^{-4}\ cm^3 mol/g^2$, $\frac{A_2}{A_{2-HS}} = 0.26$. Using the square well potential, Equation (3.5), one can find $A_2 = 1 - (\lambda 3 - 1)[exp(\epsilon/kT) - 1]$ assuming a typical value for λ, 1.5, a well depth of about -0.35kT is calculated. Although the square-well potential is a crude approximation for this system the energy is consistent with van der Waal's force, 0.3-0.4kT.

$$U(r) = \begin{cases} \infty & r < 2a \\ -\epsilon & 2a < r < \lambda 2a \\ 0 & r > \lambda 2a \end{cases} \tag{3.5}$$

The Huggins interaction parameter χ can be calculated from A_2 using Equation (3.6).[72]

$$\chi = \frac{1}{P_1}\left[\frac{1}{2} - \frac{V_1 M_2^2 A_2}{V_2^2}\right] \tag{3.6}$$

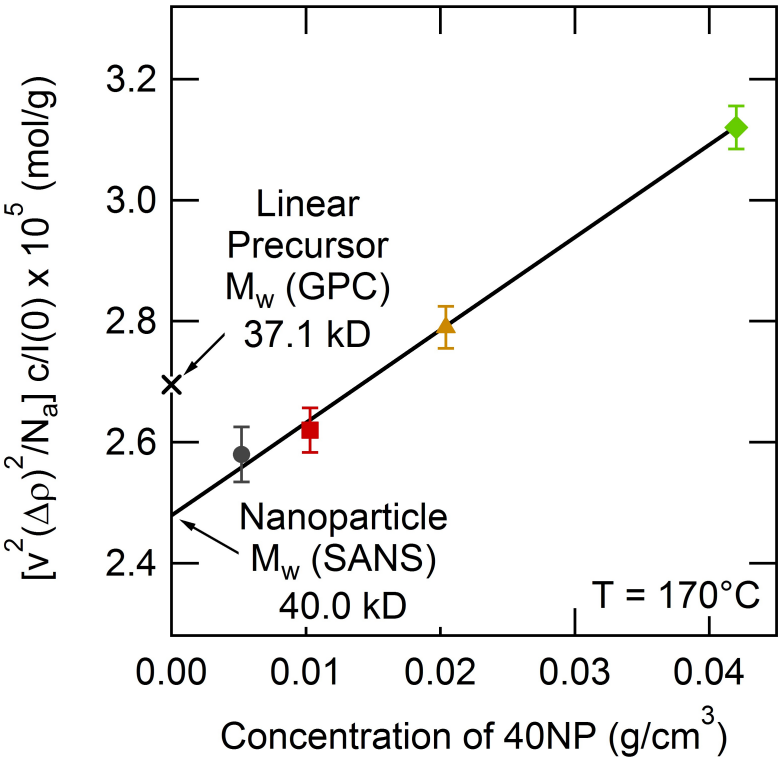

Figure 3.6: Virial Plot, concentration of scatterer over intensity at zero wavevector against concentration of scatterer (c/I_0 vs c) for 40 kD tightly crosslinked polystyrene nanoparticles[2] in 120 kD perdeuterated linear polystyrene at 170 °C. Solid line indicates linear regression fit to data set. Second Virial Coefficient, A_2, is proportional to the slope and M_W is the inverse of the intercept according to Equation (3.3.1). $A_2 = (7.66 \pm 0.34)x \times 10^{-5}\ cm^3 mol/g^2$ a value which proves the nanoparticles are soluble in the 120 kD perdeuterated linear polystyrene at 170 °C. Also $M_W = 40.0 \pm 0.3\ kD$ suggesting a slight dimerization during nanoparticle synthesis when compared to the M_W of the linear precursor at 37.1 kD but reinforcing the dispersion claim.

Where P is the ratio of the reduced volume to a reduced reference volume, in this work we will use the volumes in their unreduced form and the Kuhn segment length for PS is used as the reference volume. The subscript 1 denotes the polymer chain or solute and 2 denotes the nanoparticle. This relationship between χ and A_2 is limited to systems with uniform segment density and no dependence for χ on concentration.[72] These assumptions are valid for our system since it is comprised of linear chains and the concentrations of the nanoparticles are small and cover a short range. From this expression χ is calculated to be -0.047 ± 0.002, a favorable mixing energy. This is quite surprising given blends of linear protonated and deuterated polystyrene have a positive χ and phase separate[73, 74]. If this system was composed of to linear chains of the same molecular weights χ would be 1.6 ± 0.6 which is below 0.5 so the system would be stable. However, mixing is more favorable for the linear-nanoparticle system than the linear-linear system especially as molecular weights are increase.

Comparing to a larger chain larger nanoparticle system in the literature, 473 kD perdeuterated polystyrene with 210 kD crosslinked polystyrene nanoparticles ($\chi = -1.2 \times 10^{-3}$)[20], we see the smaller system has more favorable mixing energy. Initially this may seem counter-intuitive as larger chains have a smaller swelling penalty, however, that penalty scales as $(a/R_g)^3$)[20] and the combination of larger chains and larger nanoparticles results in a higher swelling penalty, $(5.9/21)^3 > (2.8/11)^3$.

3.3.2 120dPS-230NP

Moving to larger nanoparticles, 230 kD tightly crosslinked polystyrene nanoparticles[2] (230NP) were blended with 120 kD perdeuterated linear polystyrene (120dPS). In Figure 3.7 we show

Table 3.4: Kratky peak position from four volume fractions of 230 kD tightly crosslinked polystyrene nanoparticles[2] (40NP) in 120 kD perdeuterated linear polystyrene (120dPS) measured at 170 °C. The large characteristic length (d) indicates the 230NPs are phase separating and not surprisingly the high volume fractions have larger agglomerates since there is more opportunity for individual nanoparticles to come into contact.

Sample	Peak Position (Å^{-1})	Size $d = \frac{2.6}{q}$ (nm)
0.5v% 230NP	0.00914	34.4
1.0v% 230NP	0.00745	42.2
2.0v% 230NP	0.00211	148.9
4.0v% 230NP	0.00192	163.6

the one dimensional scattering profile of four volume fractions of 230NP in 120dPS. Problems with the instrument control software prevent acquisition of the low q-range for the lowest two volume fractions of nanoparticles. The scattering profiles of the nanocomposites with 230NP look similar to the profiles of the 120dPS-40NP nanocomposites, though the scattering intensity is significantly higher, indicating a larger scatterer volume in the q-range measured. This increase is somewhat expected since the 230 kD tightly crosslinked polystyrene nanoparticles[2] (230NP) are approximately 2 times larger than the 40 kD tightly crosslinked polystyrene nanoparticles[2] (40NP), however, that size does not account for such a large increase in scattering intensity.

Kratky plots ($q^2I(q)$ vs q) made from the scattering profiles of the 140NP composites, Figure 3.8, exhibit a single peaks that become more pronounced at higher volume fraction, again indicative of particle like structure. However, the the peaks do not occur at the same position. Peak locations are listed in Table 3.4, the peak position decrease with increasing volume fraction of 230NP. This corresponds to an increased scatterer size as volume factions increase, which is not unexpected if the system 230NP nanoparticles are phase separating.

Fitting to the Guinier region, Figure 3.9 to determine R_g and I_0 for the 120dPS-230NP

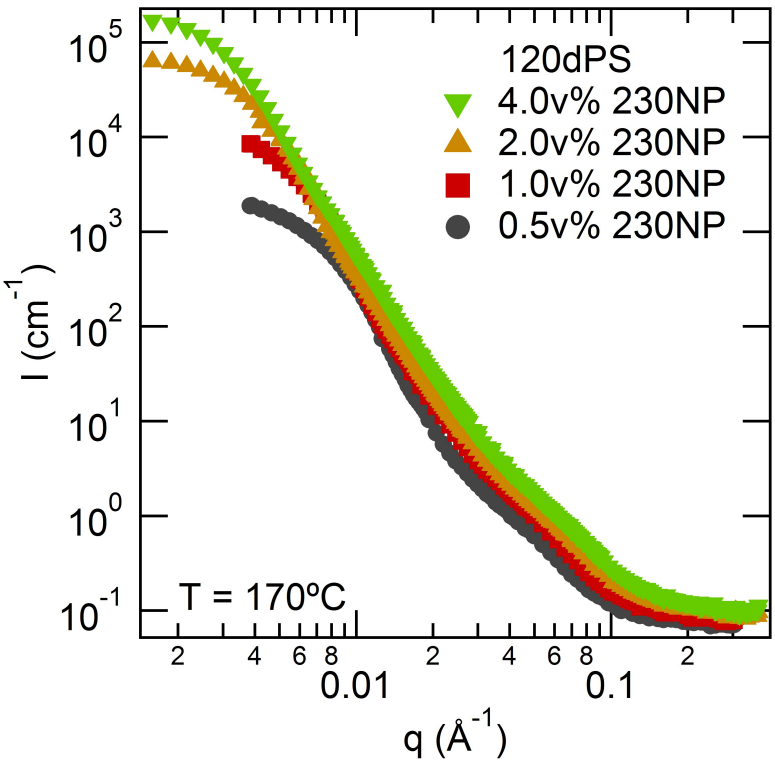

Figure 3.7: Neutron scattering profiles ($I(q)$ vs q) of the azimuthally averaged 2D scattering profiles from 4 volume fractions of 230 kD tightly crosslinked polystyrene nanoparticles[2] (230NP) in 120 kD perdeuterated linear polystyrene (120dPS). Like the scattering profiles of the 120dPS-40NP system, Figure 3.2, the scattering intensity increases with increasing 230NP content and has the shape of a particle-like scatterer with incoherent background.

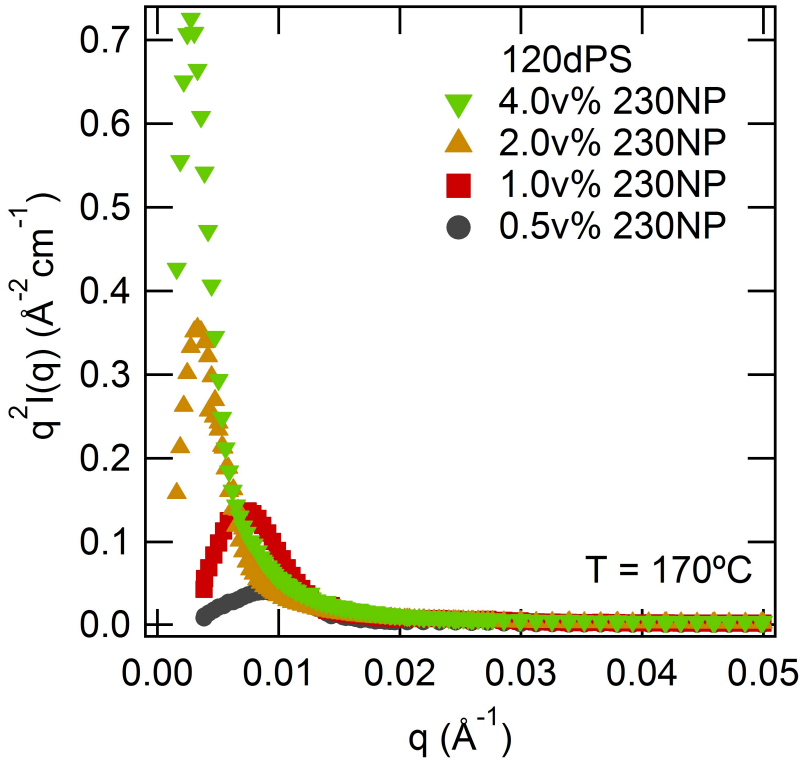

Figure 3.8: Kratky plots ($q^2I(q)$ vs q) of the azimuthally averaged scattering profile from 4 volume fractions of 230 kD tightly crosslinked polystyrene nanoparticles[2] (230NP) in 120 kD perdeuterated linear polystyrene (120dPS) at 170 °C. A peak in the Kratky plot indicates a particle like structure, which is expected for this system. However the peak positions decrease with volume fraction of 230NP which corresponds to an increase in the characteristic length scale (d) of the scatter (230NP). Peak positions and characteristic length scales are listed in Table 3.4.

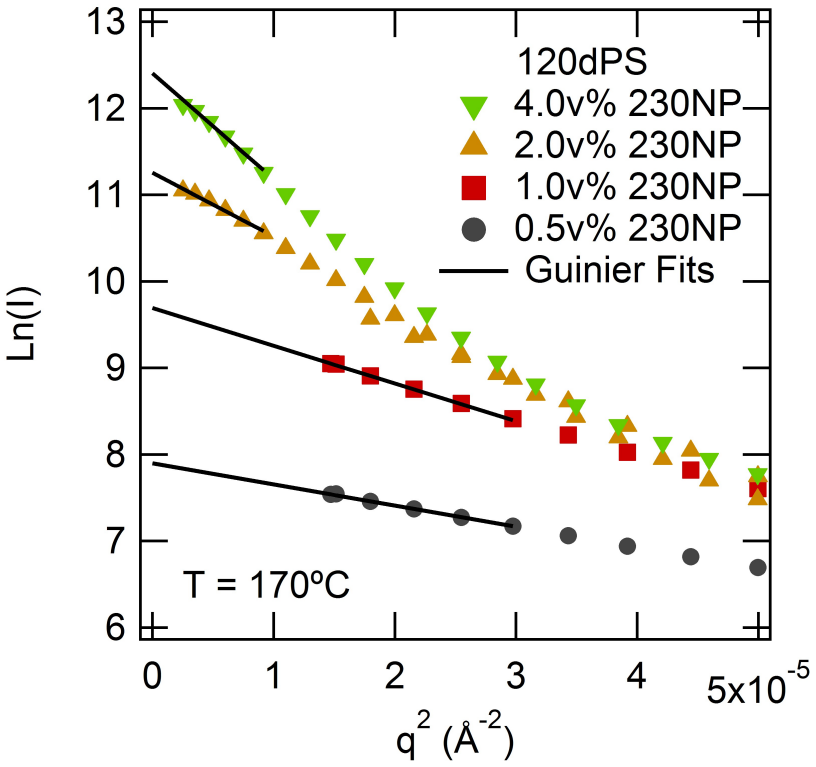

Figure 3.9: Guinier plots ($Ln(I(q))$ vs q) of the azimuthally averaged scattering profile from 4 volume fractions of 230 kD tightly crosslinked polystyrene[2] (230NP) in 120 kD perdeuterated linear polystyrene (120dPS) at 170 °C. Solid lines indicate fits to Guinier Equation, Equation (3.1) and the radius of gyration and intensity at zero wavevector were determined. Similar to the characteristic length scale from the Kratky plots (Figure 3.8, Table 3.4 the radius of gyration increases with volume fraction of 230NP and is significantly larger than the R_h and literatures values[1] for these nanoparticles, a clear sign of phase separation. The intensity at zero wavevector (I_0) will be used to determine solubility and mixing energy. The results of the fits to the Equation (3.1) are listed in Table 3.5.

systems we see a significantly larger than expected radius of gyration listed in Table 3.5. Again this is a clear sign of the 230NP nanoparticles phase separating.

A Virial plot (c/I_0 vs c, constructed form the Guinier fit data, is not particularly relevant for this phase separated system. The calculated Second Virial coefficient is negative, though not directly related to the individual nanoparticles, and the molecular weight is quite large, 2.11×10^8 g/mol. However this molecular weight is consistent with average agglomerate

Table 3.5: Results of Guinier fits to scattering profiles of 230 kD tightly crosslinked polystyrene nanoparticles[2] (230NP) in 120 kD perdeuterated linear polystyrene (120dPS) at 170 °C. The large R_g is a clear sign of phase separation which increases with volume fraction of 230NP. Aggregate size vs volume fraction is plotted in Figure 3.10.

Sample	$I_0(cm^{-1})$	±	$\langle R_g \rangle_z$ (Å)	±
0.5v% 140NP	2692	24	270.8	2.2
1.0v% 140NP	16174	807	361.5	12.7
2.0v% 140NP	77188	445	469.4	3.6
4.0v% 140NP	244018	3541	605.0	7.0

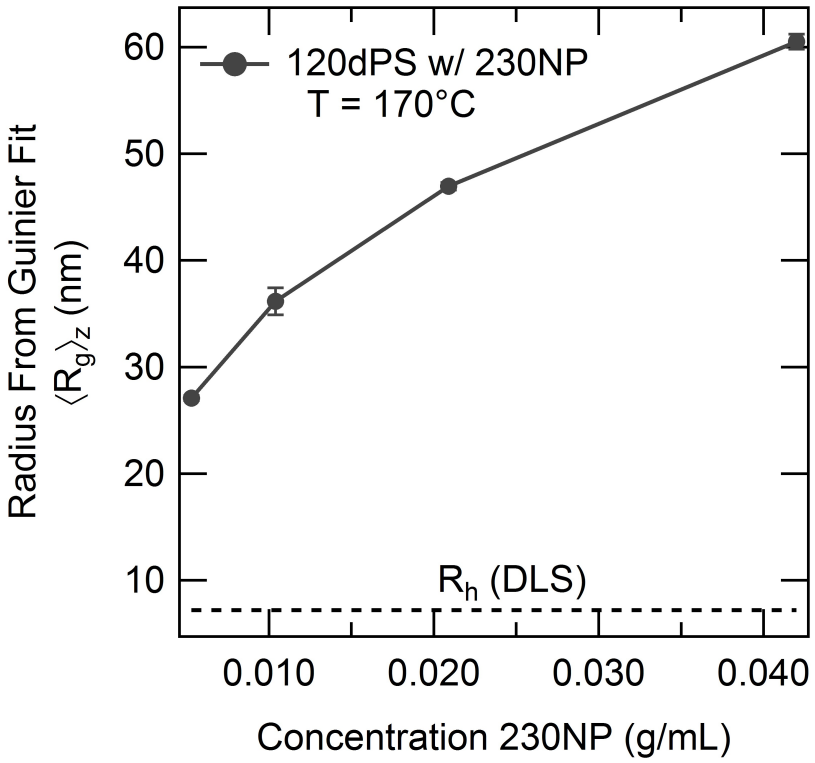

Figure 3.10: Aggregate size from 4 volume fractions of 230 kD tightly crosslinked polystyrene nanoparticles[2] (230NP) in 120 kD perdeuterated linear polystyrene (120dPS) at 170 °C. The large 230NP aggregate size, relative to R_h of individual nanoparticle is a clear sign of phase separation.

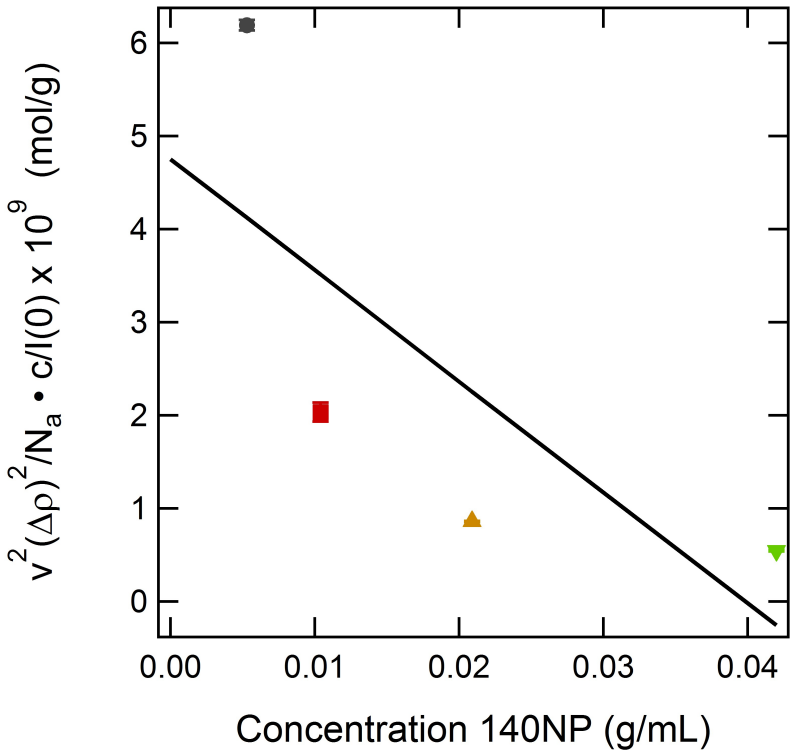

Figure 3.11: Virial plot from Guinier fits of 230 kD tightly crosslinked polystyrene nanoparticles[2] (230NP) in 120 kD perdeuterated linear polystyrene (120dPS). Negative slope indicates insolubility of the 230NP in 120dPS.

molecular weight of $(8.64 \pm 7.88) \times 10^7$ g/*mol*.

We can again see the phase separation through rheology. In Figure 3.12 we show the terminal viscosity ratios for the same 120dPS-230NP "nanocomposite" systems, again at four different volume fractions. Einstein's relation is also included and you can see this systems follow it quite well. In our experience adherence to Einstein's relation simply means the nanoparticle have agglomerated to the point where they cannot produce a reduced viscosity and instead are acting more like a classic colloidal system[9, 10, 11, 12]. Complete master curves for these composites are included at the end of the chapter, Figure 3.15.

Finally enough beam time was given to allow to look at the effect of annealing time on the 120dPS-230NP "nanocomposite" systems. Remember each disk was annealed a for

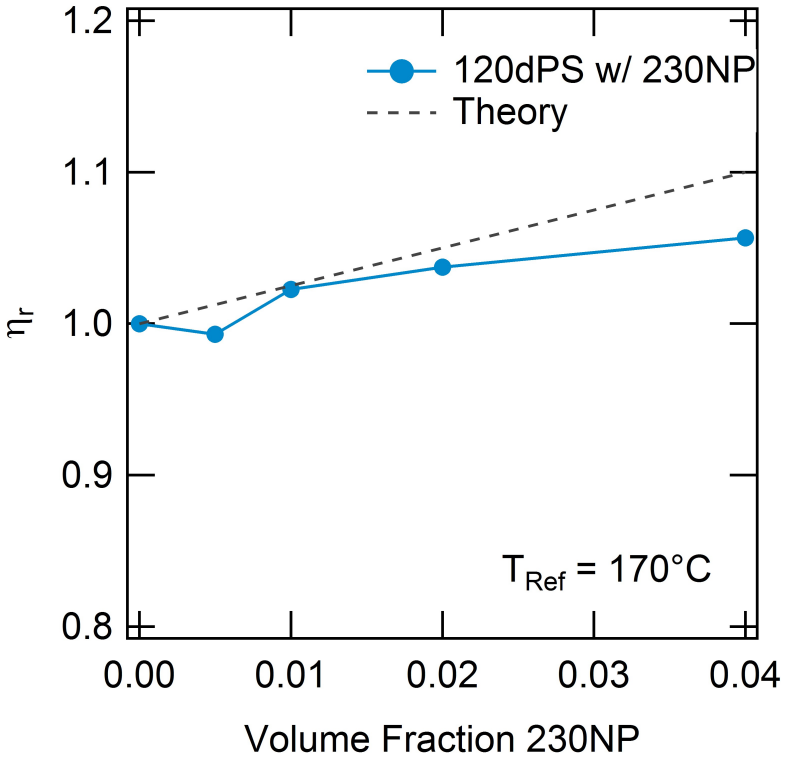

Figure 3.12: Terminal viscosity ratios (η_r^0) of 120 kD perdeuterated polystyrene (120dPS) with four volume fractions of 230 kD tightly crosslinked polystyrene nanoparticles[2]. Theory line indicates Einstein's relation[4] with Batchelor's correction[5] ($\eta_r = 1 + 2.5\phi + 6.2\phi^2$) which this system follows indicating colloidal behavior[9, 10, 11, 12] instead of well dispersed nanoparticles as seen in the 120dPS-40NP terminal viscosity ratios, Figure 3.1. Terminal viscosities are reported as the η^0 parameter from a fit of the Carreau-Yasuda Model[6, 7] following conversion of the complex viscosity to steady shear using the Cox-Merz Rule[7, 8]. Terminal viscosity ratios with 8.5 v% 230NP blends with any v% of 75PS are extrapolated. Complex viscosity and moduli master curves for these composites are included at the end of the chapter, Figure 3.15. All data shifted to a reference temperature of 170 °C.

15 minutes before being loaded into the sample cells. In this portion of the experiment two of the disks were further annealed at 170 °C for 3 hours and the remaining two were loaded at 127 °C. Unfortunately a lack of samples prevented a proper experimental setup i.e., comparison at constant volume fraction. Instead the samples that previously showed the largest agglomerates (2 and 4 v% 140NP), were not annealed any further and the samples with the smallest agglomerates (0.5 and 1 v% 140NP) were annealed for the extra 3 hours. All samples were measured at 127 °C.

In Figure 3.13 we show the Kratky plots for the two different annealing conditions. The two highest concentration (short annealing time) composites have a peak at a much higher q value than the two lowest concentrations (long annealing time) indicating larger agglomerates as the sample worked toward equilibrium. In Table 3.6 the peak positions and characteristic length scales are reported. Although this experimental set was not ideal, it does show the increase in in agglomerate size with volume fraction and annealing time. Furthermore it points to the fact that the 230NP nanoparticles started off in a well dispersed state. In the 15 minute annealing time cases the characteristic size is only about 2-3 that expected for a single particle, even at the high volume fraction where agglomerates have a better opportunity to form.

The driving force for the agglomeration is probably two fold. First the 140NP particles are approaching the size of the 120 kD dPS and the penalty for chain stretching[22, 23, 24, 25, 26, 27, 28] is too high, remember it scales with $(a/R_g)^3$[20] which is based on stretching of polymer brushes[51, 33] and results in an entropic loss to the chains[50, 51] The scaling for the penalty for 230NP - 120 kD dPS system $(5.9/11)^3$ is an order of magnitude higher than the 25NP - 120 kD dPS system $(2.8/11)^3$. Secondly the volume fractions (chosen for

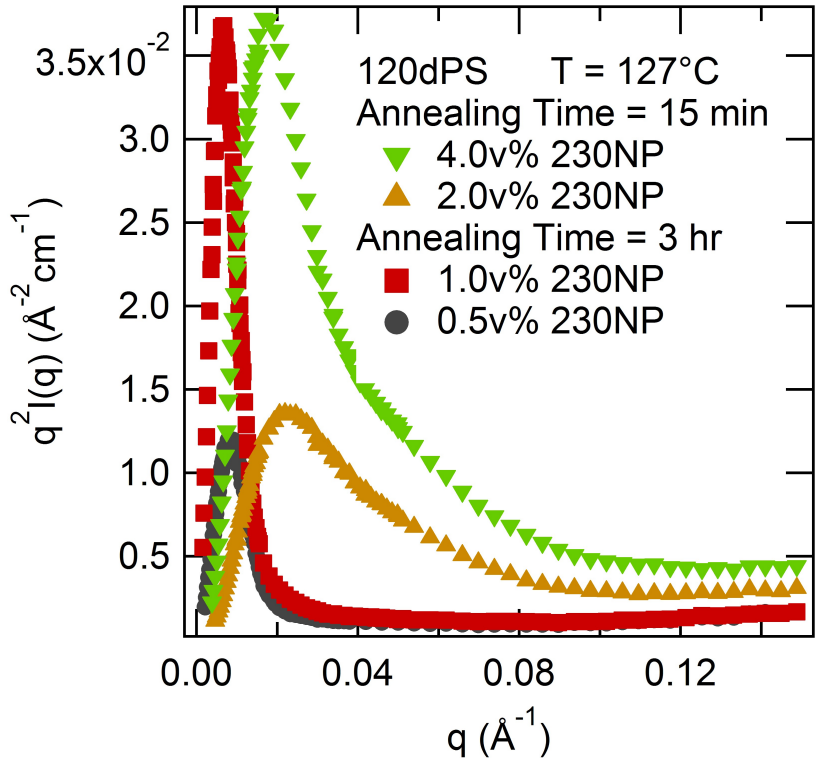

Figure 3.13: Kratky plots ($q^2I(q)$ vs q) of the azimuthally averaged scattering profile from 4 volume fractions of 230 kD tightly crosslinked polystyrene nanoparticles[2] (230NP) in 120 kD perdeuterated linear polystyrene (120dPS), measured at 127 °C. Two annealing times were used, longer annealing time results in larger 230NP aggregates regardless of 230NP volume, indicated by shift of peak to lower q (larger characteristic length scale of scatterer).

Table 3.6: Peak positions from Gaussian fit to peak in Kratky Plots (Figure 3.13) of 230 kD tightly crosslinked polystyrene nanoparticles[2] in 120 kD perdeuterated linear polystyrene (120dPS) at two different annealing times 15 minutes and 3 hours at 170 °C, measured at 127 °C. Characteristic length scale calculated from $q = \pi/d$, longer annealing time has a significantly larger 230NP aggregate size.

Annealing Time	v% 230NP	Peak Position (Å^{-1})	$d = \frac{2.6}{q}$ (nm)
3 hours	0.5v%	0.00858	36.6
3 hours	1.0v%	0.00673	46.6
15 minutes	2.0v%	0.0232	13.5
15 minutes	4.0v%	0.0180	17.5

an accurate Virial analysis) are below that of the confinement limit ($h < Rg$). Again when a chain is in the presence of a nanoparticle is swells or stretches to a non-equilibrium state. Below the confinement condition some segments of the chain are not swollen which causes a contraction of the swollen segment near the sparsely spaced nanoparticles. This process excludes the nanoparticles driving a phase separated condition.

3.4 Summary

The relationship between the nanoparticle size and suspending chain size is quite clear from this work. In the system where the nanoparticle is significantly smaller than the suspending chain the mixing is very favorable as that ratio approaches unity the penalty due to chain swelling (or stretching)[22, 23, 24, 25, 26, 27, 28] and subsequent entropic loss to the chains[50, 51] over takes the entropic gain of nanoparticle dispersion. In the system with the smallest nanoparticle to chain size ratio 120dPS-40NP we see favorable mixing, (negative χ), and a well dispersed system. The 40 kD tightly crosslinked polystyrene nanoparticles[2] are in a slightly swollen state and although a slight attractive force is present between the nanoparticles it is not enough to overcome the entropic loss associated with agglomeration. Furthermore this system exhibits a reduced viscosity in the melt state a result that is often seen in composited with well dispersed spherical nanoparticles.[19, 20, 55] As the ratio of nanoparticle size to polymer length approaches unity the penalty from chain stretching[22, 23, 24, 25, 26, 27, 28] becomes to high and the nanoparticles phase separate as seen in the 120dPS-230NP system. Although a contribution due to lack of confinement can not be ruled out as a driving force for the agglomeration. Looking at agglomerate size with respect to annealing time we can conclude that blending by rapid precipitation produced a

well dispersed system and thermally annealing allowed the composite to move toward it's equilibrium state with the nanoparticles agglomerated, a process requiring several hours. Melt rheology of these systems followed Einstein's prediction, as expected. We also see that rheology, which is quite sensitive to structure, worked as an excellent tool for determining dispersion. Though it is only useful for determining whether or not the nanoparticles were dispersed. Subtle details such as particle size can only be determined with respect to the suspending chain size, however, it is an excellent method for a quick determination of dispersion if other methods such as scattering or TEM are unavailable.

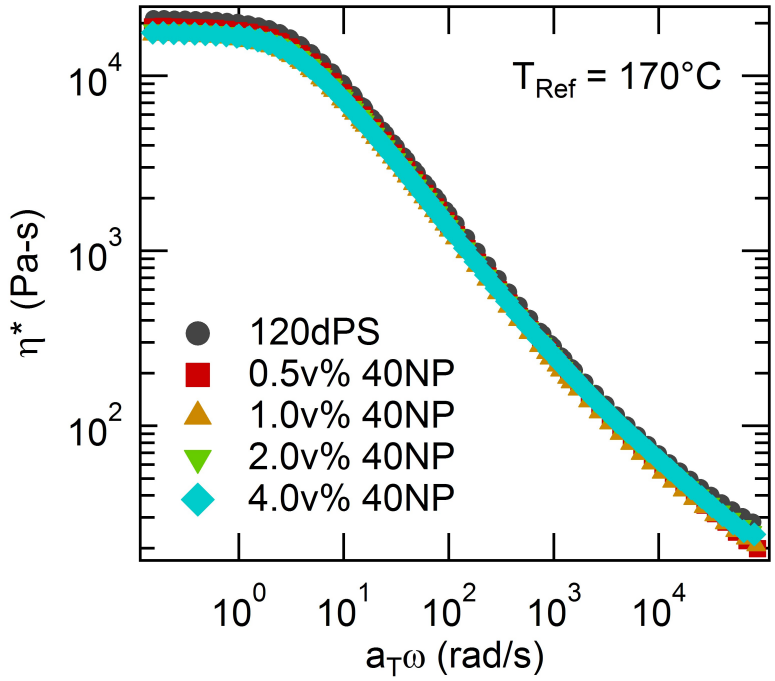

(a) Complex Viscosity

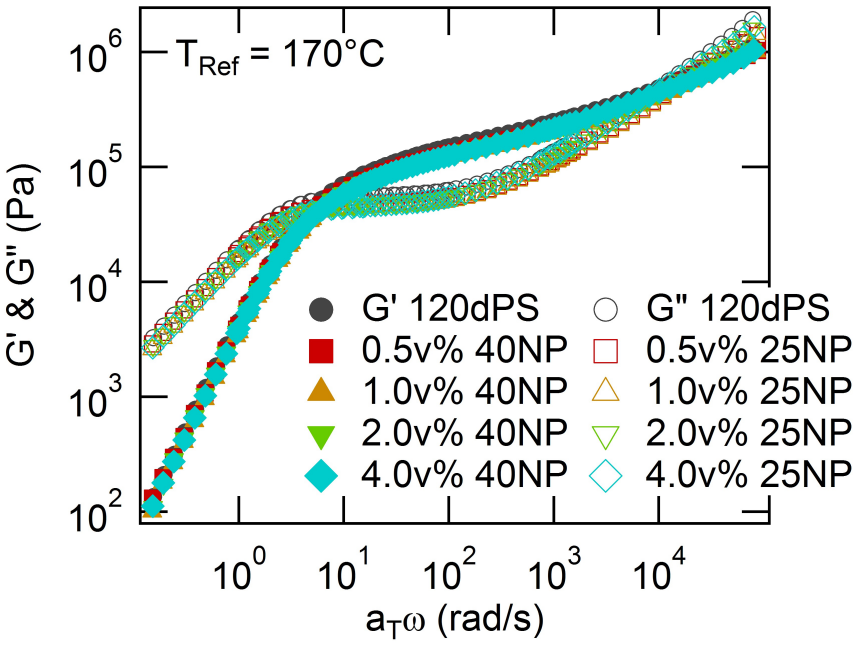

(b) Storage & Loss Moduli

Figure 3.14: Master curves of 120 kD perdeuterated linear polystyrene (120dPS) with four volume fractions of 40 kD tightly crosslinked polystyrene nanoparticles[2] (40NP). Results shifted to a reference temperature of 170 °C.

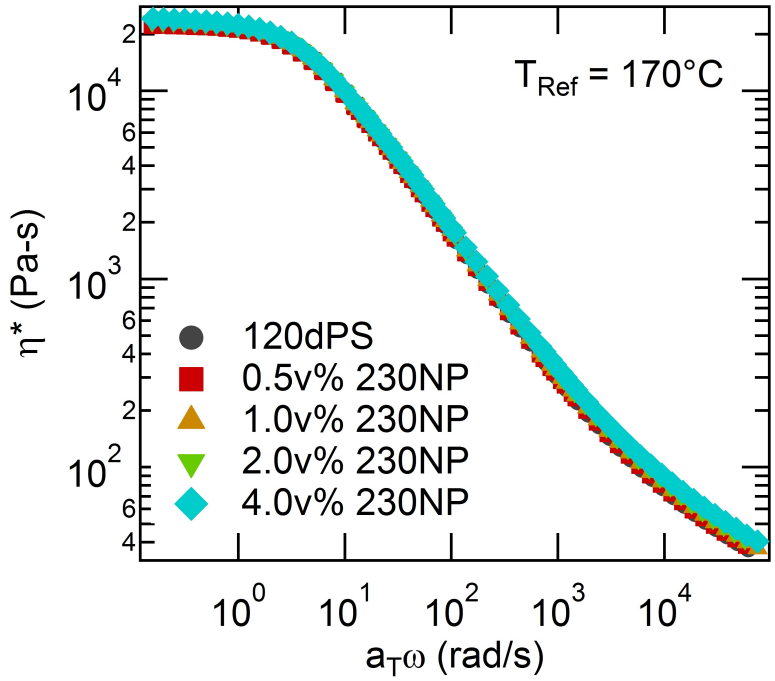

(a) Complex Viscosity

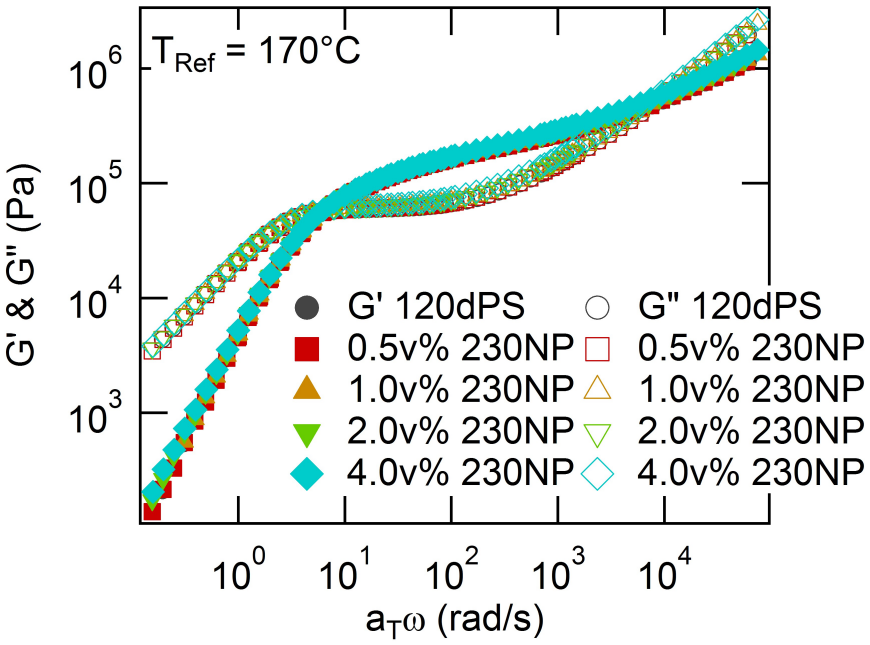

(b) Storage & Loss Moduli

Figure 3.15: Master curves of 120 kD perdeuterated linear polystyrene (120dPS) with four volume fractions of 230 kD tightly crosslinked polystyrene nanoparticles[2] (230NP). Results shifted to a reference temperature of 170 °C.

Chapter 4

PMMA Nanocomposites

4.1 Introduction

Fullerenes (C_{60}) has been added as a dispersed phase into many polymer composite systems resulting in a variety of effects on the composite properties and new properties intrinsic to C_{60}. Polymer composite of PMMA and C_{60} offer protection from ionizing radiation[75] and reduced flammability[76]. The small size of the nanoparticle also changes the morphology. Inclusion of C_{60} distorts or completely disrupts the regular network formation in block copolymers.[77] Nanoparticles including C_{60} prevent de-wetting of polymer thin films.[78, 79] Derivatives of C_{60} like phenyl-C61-butyric acid methyl ester (PCBM) are used heavily in organic electronic devices such as polymer solar cells.[80, 81, 82] However, changes to the material properties are very dependent on dispersion which in turn is dependent on blending method. Using an evaporative blending method, either film casting or spin coating, results in a phase separated system especially in composite systems with chemically dissimilar systems. This phase separation leads to aggregation of the nanoparticles resulting in typical colloidal dispersion results such as an increase in melt viscosity[10, 11] for PMMA-C_{60}[83] and PS-C_{60}[55]. Blending by rapid precipitation resulting in a decrease of melt viscosity in PS-C_{60} composites[55] as well as increased chain dynamics[84]. C_{60} is well known to have a low solubility in many organic solvents[85] and most polymer melts[86]. In this work we blend C_{60} and Fe_3O_4 nanocrystals with PMMA using rapid precipitation where we expect a good dispersion and a decrease in melt viscosity.

4.2 Experimental Methods

77 kD PMMA and 388 kD PMMA were purchased from Scientific Polymer Products, Inc and used as received. C_{60} was purchased from Term-YSA (Moscow, Russia) and used as received. Fe_3O_4 nanoparticles, $R_h = 6\ nm$, were purchased from Ferrotec (San Jose, CA, USA) with an oleic acid solubility agent and used as received. Composite blends were prepared by rapid precipitation. Due to the low solubility of C_{60} in organic solvents it was dissolved separately in toluene at 5 mg/mL, sonicated for 1 hour and filtered though a 0.2-μm Teflon syringe filter to removed aggregates. Solid PMMA was added along with the appropriate volume of C_{60} solution and pure toluene until a polymer concentration of 10 mg/mL was achieved. PMMA and Fe_3O_4 were prepared by adding the appropriate volume of each to toluene again holding the concentration of polymer at 10 mg/mL. These solutions were left to equilibrate for several days. The color varied from clear (pure PMMA) to dark purple increasing on the C_{60} content and clear to dark brown with increasing on Fe_3O_4 content. Prior to precipitation the solutions were sonicated for 60 minutes. The polymer-C_{60} and polymer-Fe_3O_4 solutions are added drop-wise into a 10X volume of vigorously stirring methanol. Precipitates formed immediately, colored similarly to their solution eventually settling our leaving a clear supernatant. The supernatant was decanted off and the remaining solvent/nonsolvent is separated from the precipitates by vacuum filtration using a polyamide membrane ($0.2\mu m$ pore diameter). Solids are placed in a vacuum oven at 40 $^{\circ}$C, approximately 1 week.

Rheological disks are prepared by pressing the dried solids in an 8-mm barrel die with a vacuum attachment. 77 kD PMMA samples are annealed at 160 $^{\circ}$C for 2 hours ($> 10\tau_d$[46]) and 388kD PMMA samples are annealed at 180 $^{\circ}$C for 8 hours ($> 10\tau_d$[46]) both under

slight pressure to shape the disk, examples are shown in Figure 4.1.

Rheological properties are measured on an ARES-G2 strain controlled rheometer with 8-mm parallel plates running TRIOS v1.7 and the associated firmware. PMMA is significantly stiffer than PS, with a friction coefficient 6X larger and a very low thermal degradation temperature 204 °C limiting the experimental range to conduct rheological experiments. For 77kD PMMA samples the plates were preheated to 150 °C at least 1 hour before zeroing the gap, samples were loaded on hot plates and 0.1 ± 0.05 N axial force is applied using the automatic compression feature. A time sweep at 0.1% strain and 0.5 Hz is run for 1 hour under auto compression to ensure contact with plates. The 388 kD PMMA is run under similar condition however due to the stiffness of the material 170 °C was chosen as the starting temperature. Strain sweeps at the lowest temperature and highest frequency were run to determine the linear region, 1.5% strain, and subsequent experiments were run at this stain value or below. Frequency sweeps were run in 20 °C increments up to 190 °C. Time-temperature superposition[30] is used to shift frequency sweeps from different temperature into a single master curve with a reference temperature of 170 °C.

Pressed disks were also used to look for C_{60} diffraction peaks, an indication of dispersion, using wide angle x-ray scattering. Small angle x-ray scattering was used to measure dispersion of Fe_3O_4. X-ray scattering was done on a Rigaku Ultima IV with a copper anode, wavelength 1.54 Å, and equipped with a single point scintillation crystal detector. Wide angle scans were run with the following settings: Scanning Mode = 2Theta, Scanning Type = FT, X-Ray Power = 40kV/44mA, Divergence Slit = 1.0 mm, Divergence Height Limiting Slit = 5 mm, Secondary Slit = 0.2 mm, Receiving Slit = 0.2 mm, Start Angle = 5°, Stop Angle = 65°, Step = 0.01°, Fixed Time = 5 s, and Theta = 10°. Small angle

scans were run with the settings except these: Receiving Slit = 0.1 mm, Start Angle = 0.1°, Stop Angle = 5°, Step = 0.005°, Fixed Time = 3 s, and Theta = 0°. In order to properly scale the intensity for the SAXS profiles transmissions were also collected using Start Angle = -0.1°, Stop Angle = 0.1°, Step = 0.005°, Fixed Time = 0.5 s, Theta = 0° and 0.4 mm of Al absorber was added to attenuate the beam, preventing damage to the detector. The peak intensity of each transmission was compared to an empty cell peak to determine the absorption, see section 6.2. Samples were run at room temperature.

Dynamical mechanical analysis (DMA) and tensile test were performed on a RSA3 (TA Instruments, New Castle, DE). Films were pressed from unused rheology disks using a Carver Model C press with hot plates. Rectangular bars were cut from each using a simple jig and a razor, samples were 0.09-0.12 mm thick by 5 mm wide by 2-3 cm long. Samples for DMA and tensile were loaded in a similar manner on rectangular tension compression geometries with the clamps tightened to 50 cN-m and the samples were pretensioned to 50 grams force. Tensile test were run at room temperature (22°C), with a Hencky strain of 0.01. If a low strain "toe" region was present the strain was corrected by extrapolation from the linear region to determine the proper zero strain point. Young's modulus was determined from the slope of a fit to the linear region at low strain. DMA test were run in at a frequency of 10 rad/s from 60°C to 175 °C at a ramp rate of 3 °C/minute and a strain of 0.05. Static force tracking dynamic force at 125% was enabled to ensure a good signal to noise ratio as the sample softened. A Gaussian peak was fit to the loss tangent to determine the glass transition temperature (T_g). The RSA3 was controlled using TA Orchestrator V7.2.1.1.

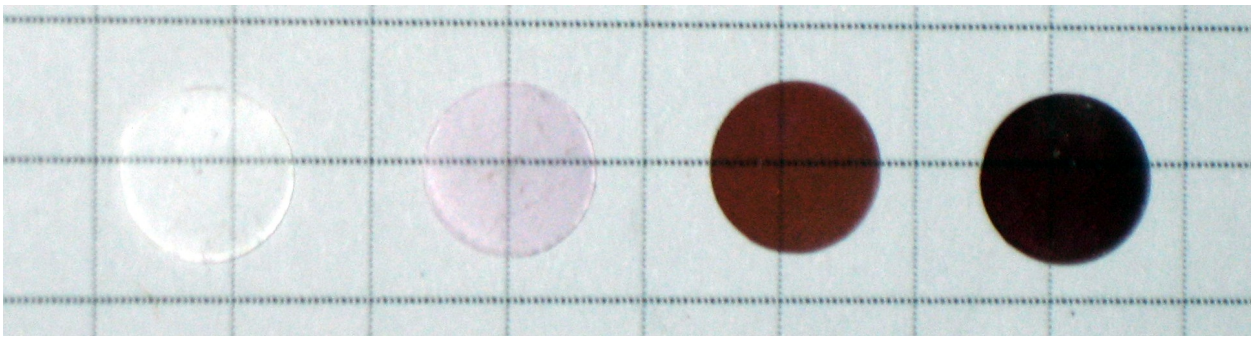

Figure 4.1: Images of 388 kD PMMA C_{60} nanocomposites at 3 different volume fractions of C_{60}. C_{60} is a strong absorber in the UV range[13] resulting in the dark purple-brown color at low loading.

4.3 Results & Discussion

Not surprisingly as C_{60} is added to the PMMA the color of the composite moves from clear to a deep purple, (the color of bulk C_{60}). The color change is obvious in Figure 4.1. The precipitates, disks, and films produced were all uniform in color and texture. The low volume fraction of C_{60} was chosen based on the small volume fractions required to achieve confinement[20], limited solubility of C_{60}[77], and for comparison to other PMMA-C_{60} composites in the literature[83].

4.3.1 Rheology

Overall, addition of C_{60} to PMMA decreases the complex viscosity over the full range of frequencies when compared to the neat material, Figures 4.2 & 4.3. This effect is more pronounced in the high molecular weight PMMA system, Figure 4.3, which is consistent with the bimodal blends, Chapter 2, and the literature, higher molecular weight chains typically result in greater viscosity reduction.[29]

The material properties for the two sets of PMMA-C_{60} composites are listed in Table

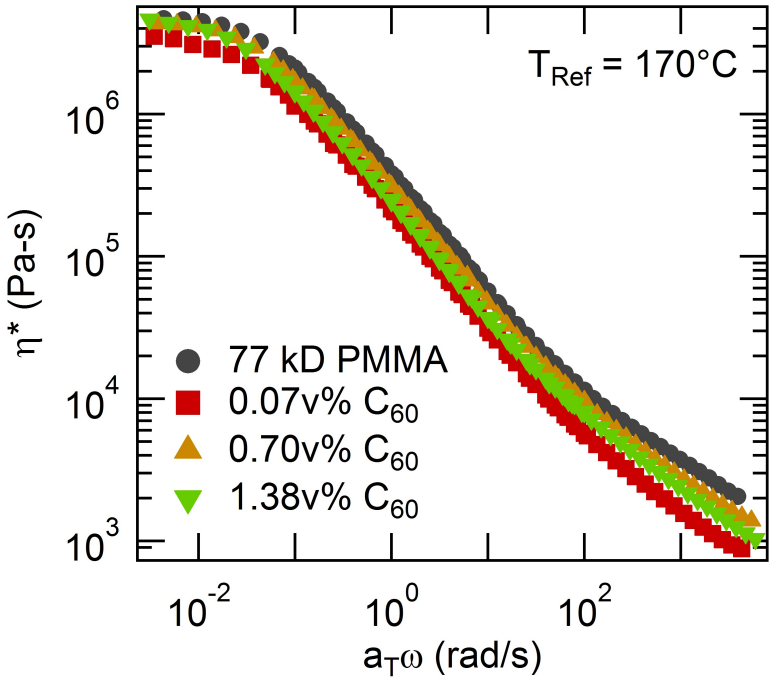

Figure 4.2: Complex viscosities from master curves of 77 kD poly(methyl methacrylate) three volume fractions of C_{60}. The viscosity of the nanocomposites are decreased with respect to the neat PMMA at all viscosities. Complete master curves for these systems are available in Appendix C: Figure C.1. All data shifted to a reference temperature of 170 °C.

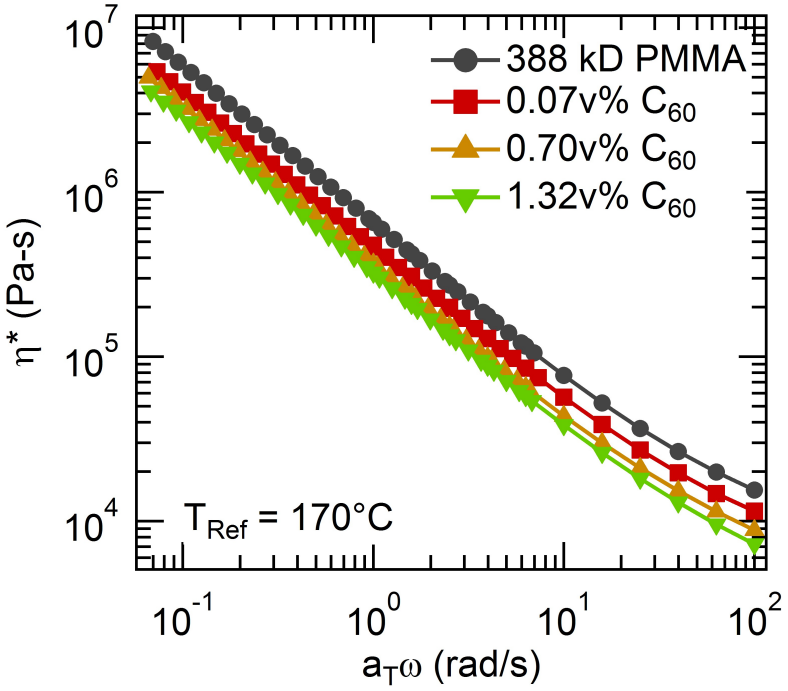

Figure 4.3: Complex viscosities from master curves of 388 kD poly(methyl methacrylate) three volume fractions of C_{60}. The viscosity of the nanocomposites are decreased with respect to the neat PMMA at all viscosities. Complete master curves for these systems are available in Appendix C: Figures C.2. All data shifted to a reference temperature of 170 °C.

Table 4.1: Material properties of PMMA-C_{60} nanocomposites from master curves shifted to a reference temperature of 170 °C. The high viscosity 388 kD PMMA and low thermal degradation point prevented measurement down to the terminal region, the complex viscosity at a frequency of 0.1 $\frac{rad}{s}$ is reported instead. ^{b}The plateau modulus is determined using the Min method[3], $G_N^0 = G'(\omega_{tan(\delta)=min})$.

PMMA M_w (kD)	C_{60} (v%)	η^0 or $^{a}\eta^*(\omega = 0.1\frac{rad}{s})$ (Pa-s)	η_r	$^{b}G_N^0$ (MPa)
77	-	4.65×10^6	1	0.462
77	0.07	3.30×10^6	0.71	0.258
77	0.70	4.33×10^6	0.93	0.361
77	1.38	4.58×10^6	0.98	0.272
388	-	$^{a}5.85 \times 10^6$	1	0.634
388	0.07	$^{a}4.04 \times 10^6$	0.69	0.442
388	0.70	$^{a}3.34 \times 10^6$	0.57	0.347
388	1.32	$^{a}2.88 \times 10^6$	0.49	0.311

4.1. The terminal viscosity was determined by fitting the Carreau-Yasuda model[6] to the complex viscosity. The plateau modulus is determined using the MIN method[47] where the value of the storage modulus at the minimum of Tan(δ) is reported,

$(G_{Nexp}^0 = G'(\omega)_{tan(\delta)\rightarrow minimum})$.

Looking at the terminal viscosity ratios for 77 kD PMMA composites, in Figure 4.2 we see the largest decrease in viscosity is from the smallest C_{60} volume fraction. Subsequent addition of C_{60} increases the viscosity ratio though it remains below the value predicted by Einstein's theory and below 1. Phase separation is a likely culprit, as nanoparticles are less soluble in short chains and it is reasonable to believe C_{60} has less favorable interactions with PMMA than the more chemically similar PS.

Unfortunately the experimental setup used to measure the 388 kD PMMA-C_{60} composite did not capture the terminal region. Still relevant deductions can be made from the complex viscosity at low frequency, for these system $\eta^*(\omega = 0.1rad/s)$ will be used as a substitute.

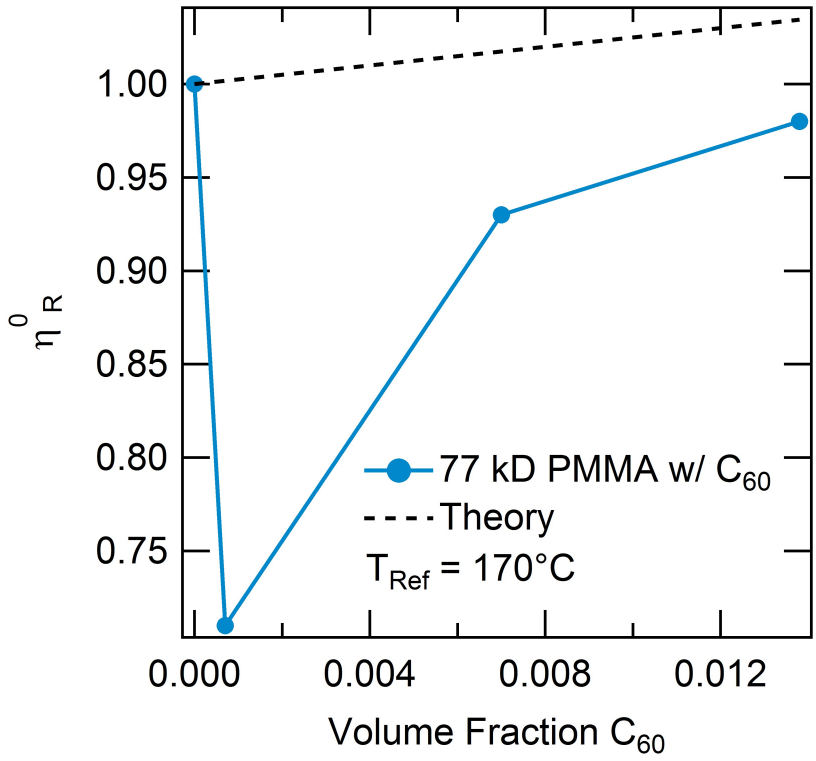

Figure 4.4: Terminal viscosity ratios of 77 kD poly(methyl methacrylate) with three volume fractions of C_{60}. Terminal viscosities are reported as the η^0 parameter from a fit of the Carreau-Yasuda Model[6, 7] following conversion of the complex viscosity to steady shear using the Cox-Merz Rule)[7, 8]. All data shifted to a reference temperature of 170 °C.

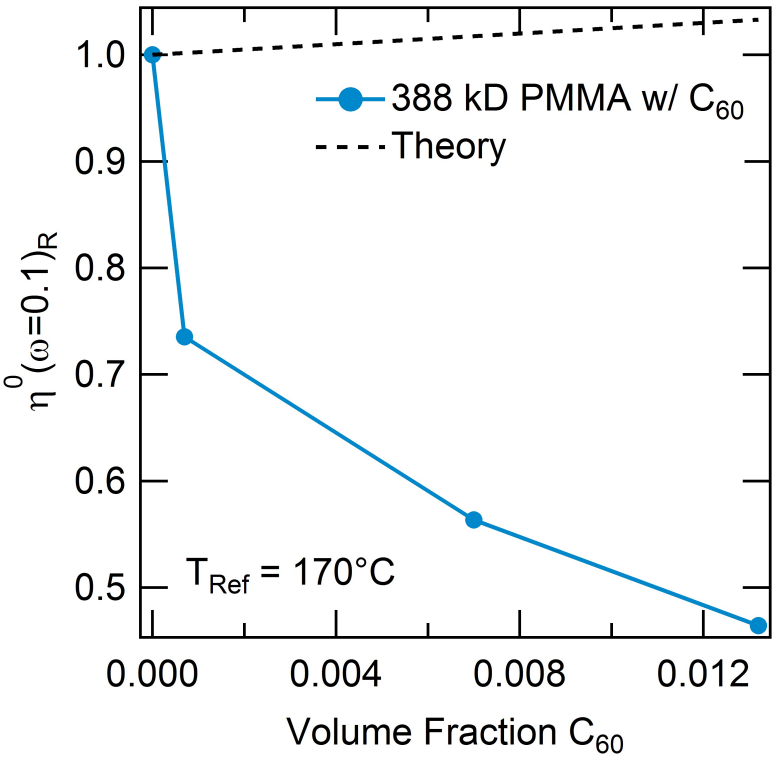

Figure 4.5: Viscosity ratios from complex viscosity at a frequency of 0.01 rad/s from master curves of 388 kD poly(methyl methacrylate) three volume fractions of C_{60}. Complete master curves for these systems are available in Appendix C: Figure C.2. All data shifted to a reference temperature of 170 °C.

In Figure 4.3 we show the complex viscosity ratios (at $\omega = 0.1 rad/s$) for 388 kD PMMA and three volume fractions of C_{60}. Unlike the lower molecular weight case as the C_{60} volume fraction is increased the viscosity reduction continues to improve. In this system we expect the nanoparticles to be more soluble as the ratio of nanoparticle radius to chain length is smaller resulting in a lower amount of chain swell and thus a smaller penalty for dispersion.

4.3.2 DMA

To rule out changes in material properties due to glass transition temperature, seen in thin polymer films[87, 88, 25, 89, 90], DMA was preformed on one group of the composites. In

Table 4.2: Glass transition temperature of 388 kD PMMA C_{60} nanocomposite at four volume fractions of C_{60}. The glass transition temperature for the composite is unchanged from the neat PMMA.

PMMA M_w (kD)	C_{60} (v%)	T_g (°C)	±
388	-	144.1	0.1
388	0.07	145.7	0.2
388	0.70	144.8	1.6
388	1.32	146.5	0.1

Figure 4.6 we show the loss tangent as a function of temperature, all of the peaks overlap around 145 °C, indicating no change in the glass transition temperature. The actual peaks and associated error with the Gaussian peak are listed in Table 4.2. This values a bit high for T_g values of PMMA reported in the literature (110-120 °C). This was initially attributed to the method in which the RSA3 determines temperature. Unlike the ARES-G2 this instrument cannot measure temperature at the sample instead a set of thermocouples are placed near the hot gas inlet resulting in high temperature. However, similar values have been reported for PMMA on other DMA type instruments.[83] These results are not intended to state the precise T_g merely the similarity between the neat material and the C_{60} composites to show that it cannot account for changes to the melt state properties.

4.3.3 WAXS

Wide angle x-ray scattering (WAXS) was used to determine if any C_{60} crystallites were present in the PMMA-C_{60} composites. This method has been used as a gauge for C_{60} phase separation.[77, 91] In our composites no sign of C_{60} is present in the WAXS profiles, Figure 4.7. The scattering profiles for the PMMA samples clearly show the amorphous halo. Pure C_{60} is included to indicate peak positions.

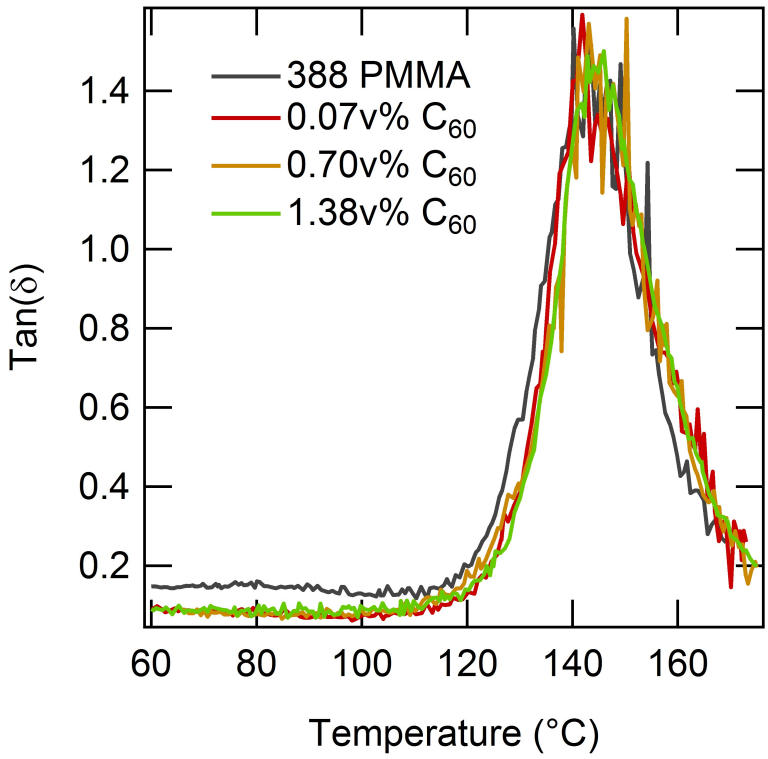

Figure 4.6: Temperature ramps of 388 kD PMMA and PMMA-C_{60} nanocomposites. The glass transition temperature is the same for the neat PMMA and all C_{60} nanocomposite, indicated by the constant peak position. T_gs are listed in Table 4.2.

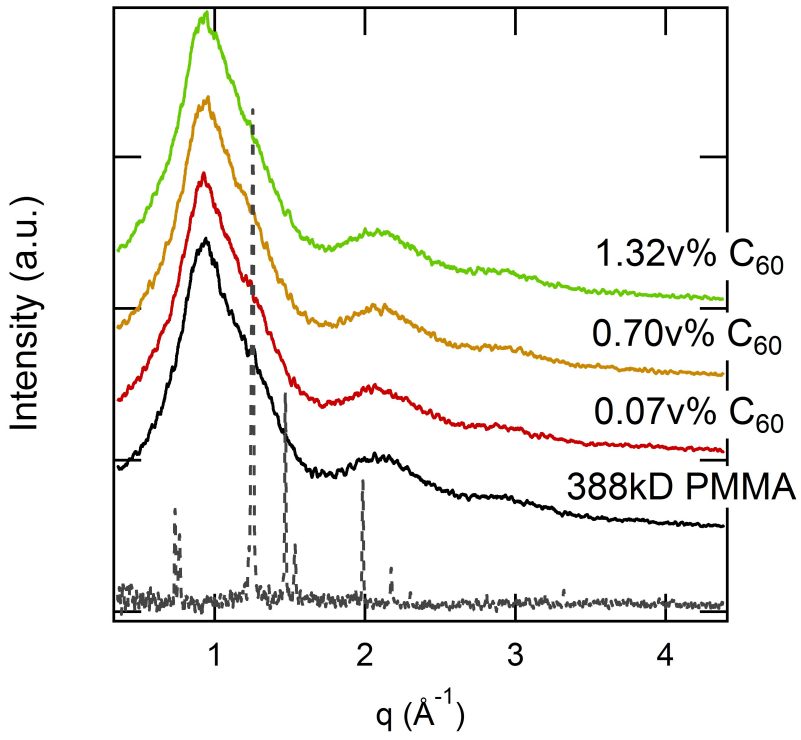

Figure 4.7: Wide angle x-ray scattering profile of 388 kD PMMA C_{60} nanocomposite at four volume fractions of C_{60} results are shifted vertically for clarity. Neat C_{60} is also shown for comparison. The lack of matching peaks indicates no C_{60} crystallites are present.

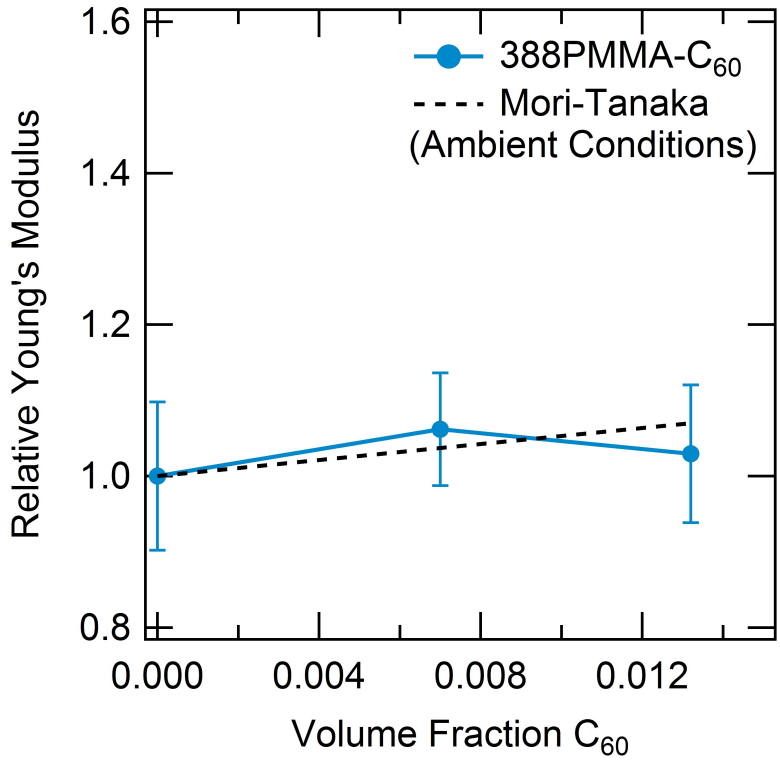

Figure 4.8: Relative Young's modulus of 388 kD poly(methyl methacrylate) with two volume fractions of C_{60}. Mori-Tanaka relationship, $Y_r = 1+5.3\phi$, is included for comparison. The Young's Modulus scales well with the Mori-Tanaka relationship.

The glassy state mechanical properties of the PMMA-C_{60} are rather uninteresting but are included for completeness and comparison to other composites. The results show no change in solid state mechanical properties, Figure 4.8, at least within the sensitivity of the instrument used.

4.4 PMMA-Fe_3O_4

Along with the C_{60} PMMA nanocomposites were also made with Fe_3O_4 which has been previously shown to produce a substantial viscosity reduction in poly(styrene) composites.[55] Much like the C_{60} the $F3_3O_4$ imparted it's color characteristics in to the composite moving

from a clear to a dark brown with increasing concentration. Again the precipitates and the disks pressed from them were uniform in color and texture. It is important to note the that volume fractions of Fe_3O_4 are much higher than those of C_{60} and only the high molecular weight system was studied (388 kD PMMA). Both the molecular weight of the suspending chain and the volume fraction of the nanoparticle were chosen to ensure solubility of the nanoparticles[20] and confinement of the chains[29]. In the case of the Fe_3O_4 which has a radius of 5-6 nm a larger volume fraction was required to ensure the half-gap was less than the R_g of the suspending polymer. Also the nanoparticle size is approaching the R_g of the lower molecular weight polymer (77 kD PMMA) so in the interest of solubility only the 388 kD PMMA was used.

4.4.1 Rheology

In Figure 4.9 we show the terminal viscosity ratio of Neat PMMA and PMMA with two volume fractions of Fe_3O_4 (2 and 5v%). An improved experimental procedure allowed data collection to a lower frequency compared to the PMMA-C_{60} systems. The terminal viscosity was again determined by fitting to the Carreau-Yasuda model. At 2 v% loading we see a decrease in the melt viscosity, similar to poly(styrene) Fe_3O_4 systems found in the literature[55], though not to the same magnitude.

4.4.2 SAXS

The high electron contrast between the Fe_3O_4 and PMMA allows the use of X-Rays to quickly measure dispersion. Instead of looking for crystallites as was the case for C_{60} we can use small angle scattering to determine the size of the nanoparticles and/or aggre-

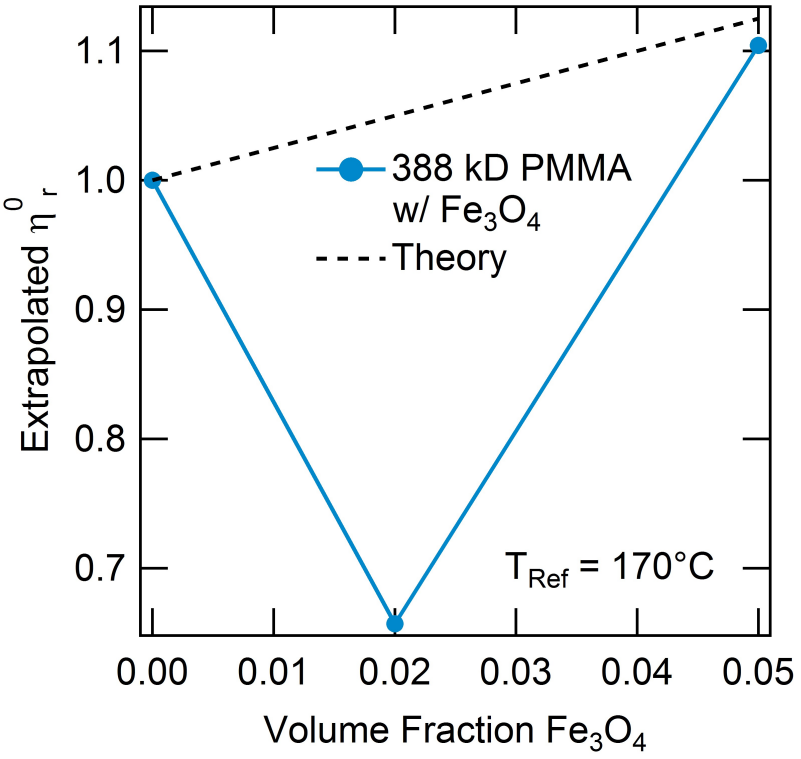

Figure 4.9: Relative zero-shear viscosity (extrapolated) of 388 kD PMMA Fe_3O_4 nanocomposites with two different volume fractions of Fe_3O_4. The high viscosity of 388 kD PMMA and low degradation temperature prohibited measurement in the terminal region. The 2.0 v% Fe_3O_4 nanocomposite has a significantly lower viscosity than predicted by Einstein's hydrodynamic theory, by 5.0 v% Fe_3O_4 the system adheres to the Einstein's prediction indicating phase separation. Terminal viscosities are reported as the η^0 parameter from a fit of the Carreau-Yasuda Model[6, 7] following conversion of the complex viscosity to steady shear using the Cox-Merz Rule[7, 8]. Complex viscosity and moduli master curves for these systems are available in Appendix C. All data shifted to a reference temperature of 170 °C.

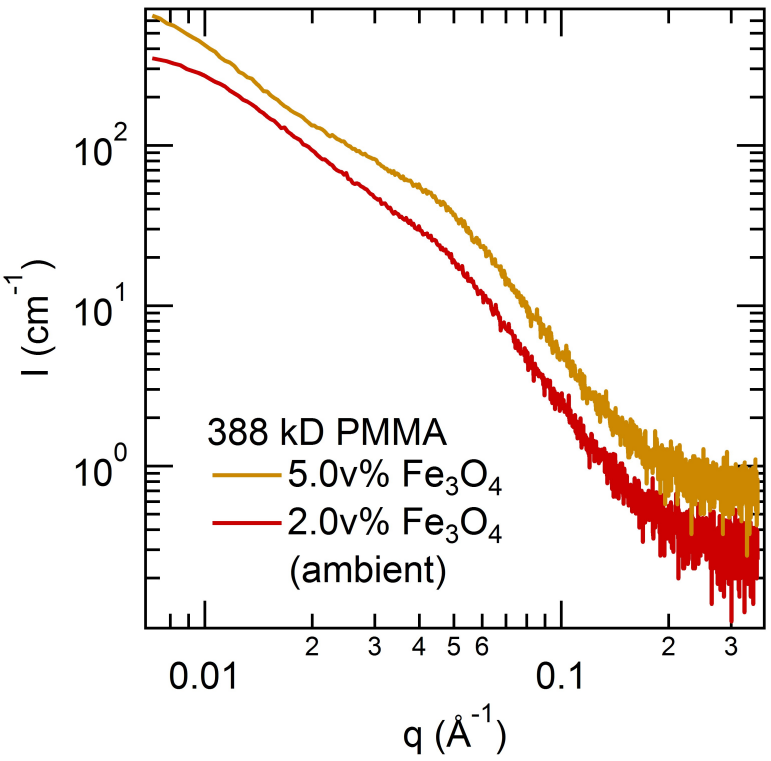

Figure 4.10: Small angle x-ray scattering profile of 388 kD PMMA Fe_3O_4 nanocomposites with two different volume fractions of Fe_3O_4, at ambient temperature.

gates. In Figure 4.10 we show the one dimensional scattering x-ray scattering profile for two volume fractions of Fe_3O_4. Absolute intensity is reported as our instrument has been calibrated against a glassy carbon standard supplied and characterized at APS by Jan Ilavsky's group[92], see Section 6.2. The scattering intensity increases with increasing volume fraction of nanoparticles as expected.

Using the same technique as the SANS work in Chapter 3 the one dimensional scattering profile are plotted as $Ln(I(q))$ vs q^2 also know as a Guinier plot, Figure 4.11. In this form fitting the low q region to the Guinier equation ($Ln(I) = -(qR_g)/3 + Ln(I_0)$) gives us the intensity at zero wavevector (I_0) and the R_g of the scatterer. This technique is limited to the region of $0.5 < qR_g < 1.0$ though qR_g up to 1.5 acceptable for polydisperse scatterers.

Table 4.3: Peak positions determined from Gaussian peak fits to Kratky Plots, Figure 4.12, of 388 kD PMMA with two volume fractions of Fe_3O_4. Characteristic length scale is reported using the following conversion, $q = 2.6/d$ based on a hard sphere scatterer.

PMMA M_w (kD)	Fe_3O_4 (v%)	q_{Peak} (Å^{-1})	d (nm)
388	2.0	0.0450	5.8
388	5.0	0.0475	5.5

The particles should be 5-6 nm in radius resulting in an upper bound of $q^2 = 1/50^2 = 4 \times 10^{-4}$ Å which is within the experimentally measured range. Unfortunately linear fits in the low-q region did not satisfy these requirements, $qR_g > 1.5$, most likely due to proximity to the primary x-ray flux. Although the slope of the intensity at low-q is slightly higher for the 5 v% system which indicates a larger scatterer. This is consistent with viscosity results as the 5 v% system is approaching the Einstein's predicted value. Regardless we will turn to another method of determine size scales of scatterers. Here we assume hard sphere scatterers and covert a the peak position from a Gaussian fit using $q = 2.6/d$, Table 4.3. The characteristic length scales determined from the peaks are consistent with the expected size of the nanoparticles, 5-6 nm. Thought this analysis suggest the high volume fraction has a smaller scatterer, contrary to the incomplete Guinier analysis. Regardless the characteristic length scale is consistent with the size of the magnetite for both volume fractions. However the we suspect there to be some agglomeration, not captured in the Kratky plot but in the incomplete Guinier analysis.

Turning instead to Kratky plots ($q^4 I(q)$ vs q) shown in Figure 4.12 we see peaks characteristic of individual spherical scatterers. The peak position can be used to determine a characteristic scatterer size.

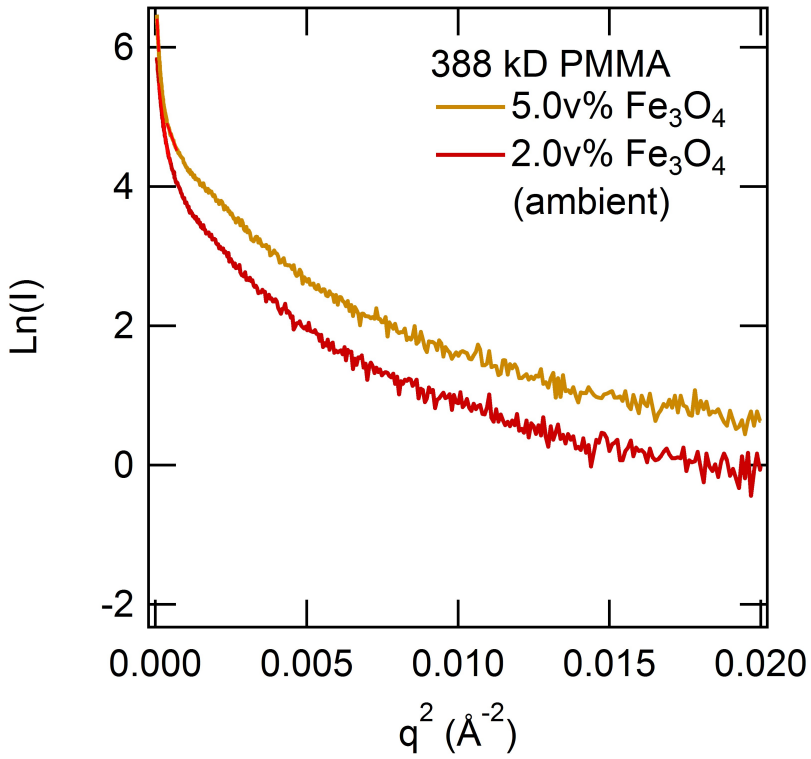

Figure 4.11: Guinier plots ($Ln(I(q))$ vs q) constructed from x-ray scattering profiles of 388 kD PMMA Fe_3O_4 nanocomposites with two different volume fractions of Fe_3O_4, at ambient temperature.

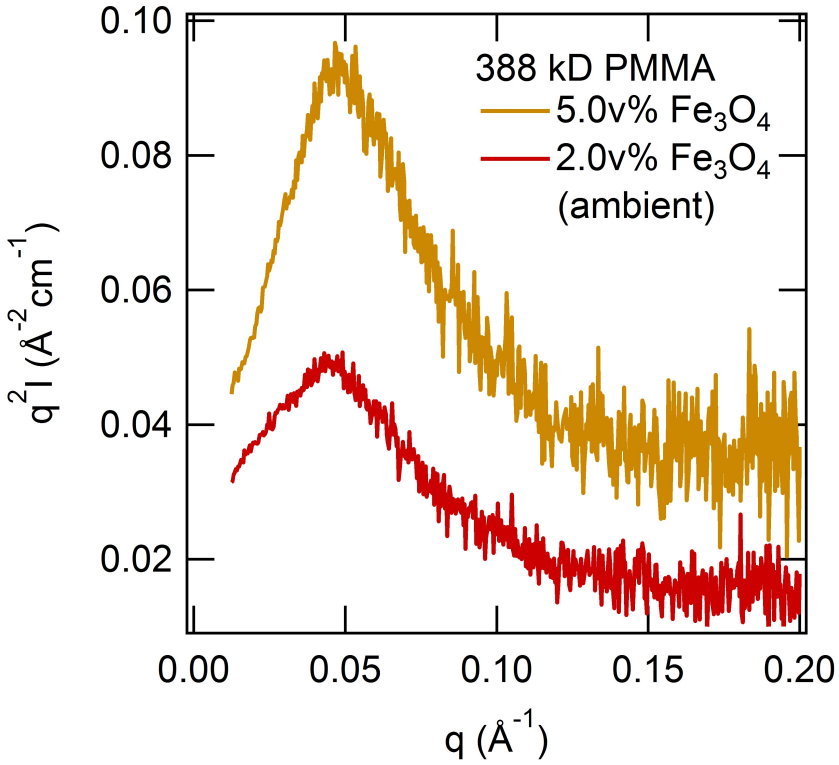

Figure 4.12: Kratky plots ($q^4 I(q)$ vs q) constructed from x-ray scattering profiles of 388 kD PMMA Fe_3O_4 nanocomposites with two different volume fractions of Fe_3O_4, at ambient temperature. A peak in the Kratky plot indicates a particle like structure, which is expected for this system.

4.4.3 Young's Modulus

Finally we look at the Young's Modulus for the PMMA-Fe_3O_4 composites. In Figure 4.13 we show the relative Young's Modulus for the neat PMMA and PMMA with two volume fractions of Fe_3O_4. The results here echo those found when measuring the rheological properties. In this case we see a large increase in the Young's Modulus for the 2 v% case that returns to the predicted value for the 5 v% case. Again the relative Young's Modulus is compared to the Mori-Tanaka model for infinitely hard spheres, a reasonable model for Fe_3O_4 in PMMA. The unusual increase at 2 v% is attributed to unusual reinforcement by the pseudo-fiber effect where regions of higher density overlap forming a high density network. The formation of these high density regions are attributed to an increase in the density fluctuations around the nanoparticles, partially described in simulations of polymer near spherical surfaces[93] and polymer-particle systems[94, 95, 96, 97, 98, 99] though the equilibrium state is not captured due to computational challenges[100, 101, 102, 103], though excess free-volume has been measured by experiment[104]. The return to the classic response is taken along with the viscosity and weak Guinier analysis to be a clear sign of phase separation in the 5 v% sample.

4.5 Summary

In this work we see a rich difference in the results generated by the incredibly small C_{60} vs the larger Fe_3O_4. In the case of the C_{60} we see a large decrease in viscosity, larger than that see for the polystyrene-polystyrene systems in Chapters 2 and 3, and larger than the decrease seen with the Fe_3O_4 from this work. There are a few things to consider when describing these results. First, and foremost, if we assume the diffusion[21, 84] of the nanoparticles to be

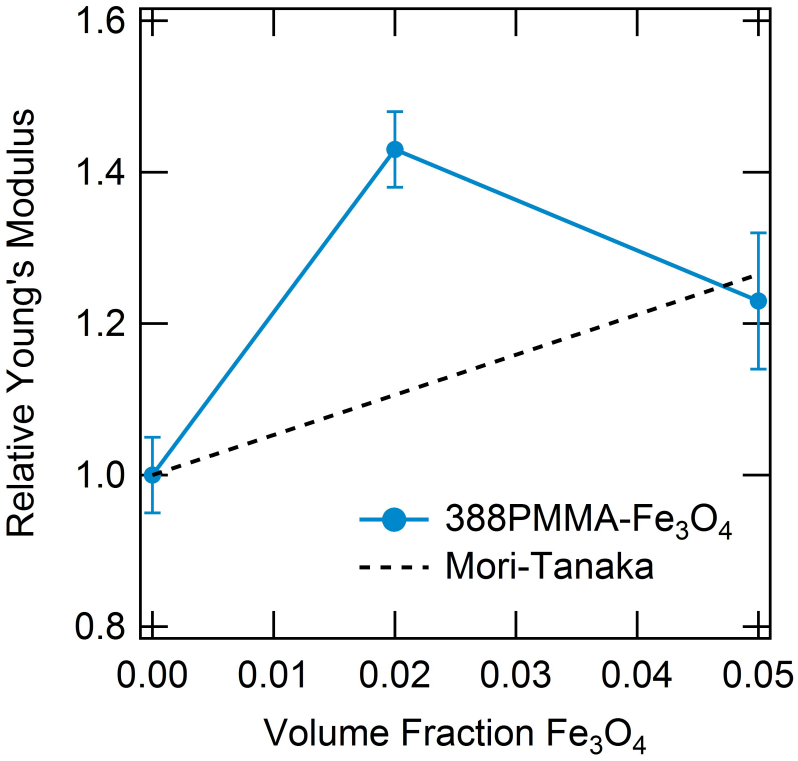

Figure 4.13: Relative Young's Modulus of 388kD PMMA Fe_3O_4 nanocomposites with two different volume fractions of Fe_3O_4. Mori-Tanaka relationship, $Y_r = 1 + 5.3\phi$, is also plotted for comparison. The 2.0 v% Fe_3O_4 nanocomposite greatly out performs the Mori-Tanaka model, by 5.0 v% Fe_3O_4 the system adheres to the Mori-Tanaka model.

the driving force for the viscosity reduction than it is not surprising that the incredibly small C_{60} molecules diffuse faster resulting in a faster terminal relaxation (the exact mechanism remains unknown). The small size of the C_{60} will also effect is solubility[19, 20, 29] and chain confinement limits[19, 20, 29]. Remember that nanoparticle must be smaller than the suspending chain ($a < R_g$) and the interparticle half-gap must also be smaller than the chain ($h < R_g$). Each of these limits is easily achieved at low volume fraction due to the small radius of C_{60} making it an ideal nanoparticle for this work. Chemical incompatibility may also play a role, C_{60} has a limited solubility is many solvents, including polymers (<2 v%), being below that limit the C_{60} remains dispersed but unfavorable interactions may drive the chains to swell a bit larger than what is seen in the PS-PS systems[27]. The larger swelling may also allow for faster diffusion, though the penalty due to swelling[20] must remain small compared to favorable separation of the C_{60}. Unfortunately this system did not result in any beneficial changes to the glassy state mechanical properties, instead resulting in essentially no change. It is clear that the results presented in this work, blended by rapid precipitation, are significantly different than systems prepared by other methods.[83]

With the larger Fe_3O_4 nanoparticles we see somewhat different results. Though higher volume fractions were required to satisfy the confinement requirement. While this appears to make a direct comparisons difficult if the systems were made below the confinement condition would be useless as they would phase separate resulting in classic colloidal conditions with an increased viscosity[9, 10, 11, 12]. The PMMA-Fe_3O_4 composites clearly show the importance of dispersion. In both the melt viscosity and solid state Young's Modulus we see the unusual effects of nanoparticles for only the 2 v% case. In the 2 v% Fe_3O_4 case we clearly see the reduced viscosity and indirect reinforcement effect nanoparticles have on

polymer chains. However the 5 v% case results in the expected increases for both viscosity and Young's Modulus from well understood theories, Einstein-Batchelor and Mori-Tanaka. It is not clear from this single data set if 5 v% is actually a solubility limit or if the dispersion technique for this system could be improved. Although best-practices were employed a few improvements, details to the rapid precipitation technique will be discussed in Chapter 5.

Overall it is clear that nanoparticles greatly effect the material properties of PMMA and proper dispersion through rapid precipitation is key to creating these interesting systems.

Chapter 5

Rapid Precipitation

5.1 Introduction

All of the composites presented in this dissertation were prepared by rapid precipitation as it is the preferred method for producing a composite will well dispersed nanoparticles. During the course of making the various systems examined and may others not listed some practical limits arose that should be discussed. The rapid precipitation method uses a solvent and nonsolvent common to both the polymer and the nanoparticle. However, during the many system precipitated the precipitant quality and uniformness of the material properties depended on the concentration of the polymer (or nanoparticle in solution). Initial work with somewhat concentrated systems (25-50 mg/mL) tended to result in a single precipitation having two distinctly different solid types. In those cases the a fibrous precipitate would be in a cloudy (particulate like) supernatant that would sometimes settle out after an extended period (weeks). Nanocomposites made with system like this would have wildly different material properties. Before continuing to make new samples the appropriate starting concentration needed to be determined.

5.2 Experimental Setup

Two different linear polymer, monodisperse 393 kD polystyrene (Scientific Polymer Products) and polydisperse Polystyrol 168N (BASF) where blended with 25NP tightly crosslinked polystyrene nanoparticles and 393 kD polystyrene was blended with oleic acid stabilized cadmium selenide quantum nanocrystals both using rapid precipitation. Neat and composite solutions were prepared at three polymer concentrations (5, 25, 50 mg/mL) in toluene and precipitated into a 10X volume of stirring methanol. Image were taken before precipitation

Table 5.1: Preparation specifications for monodisperse and polydisperse polystyrene nanocomposite blended by rapid precipitation.

Sample #	Polymer	v% 25NP	Conc. polymer in Toluene (mg/mL)
365	393PS	-	5
366	393PS	-	25
367	393PS	-	50
368	393PS	3.0	5
369	393PS	3.0	25
370	393PS	3.0	50
371	168N	-	5
372	168N	-	25
373	168N	-	50
374	168N	3.0	5
375	168N	3.0	25
376	168N	3.0	50

and several weeks after precipitation.

5.3 Results

As seen in Figure 5.1 each of the solutions is clear as expected. Each is labeled with a sample number, the preparation specifications for which are listed in Table 5.1.

Moving to the look of the precipitates several weeks after precipitation, Figure 5.2 and 5.3. In the samples with the highest concentration of polymer in solution 50 mg/mL (367, 370, 373, and 376) both the neat and composite precipitate have a fibrous almost nest looking collection of solids. This collection was typically found spun around the magnetic stir bar used to vigorously stir the methanol. Also in the composite blends, those with 25NP nanoparticles (370, 376), there is a cloudy supernatant.

Clearly the concentration of the polymer-nanoparticle solution prior to precipitation is a crucial parameter. Form this experimental set we see that polymer concentrations above

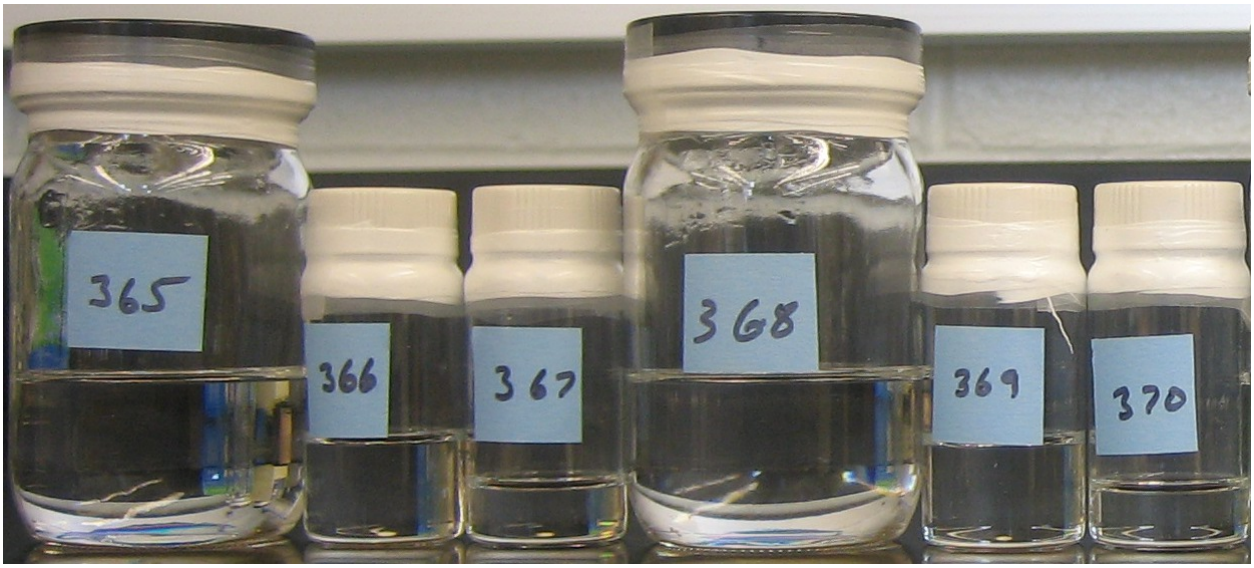

(a) 393 kD polystyrene in toluene at 5 mg/mL (365), 25 mg/mL (366), and 50 mg/mL (367) and 393kD polystyrene with 3 v% 25NP crosslinked polystyrene nanoparticles (relative to the polymer) in toluene at 5 mg/mL (368), 25 mg/mL (369), and 50 mg/mL (370).

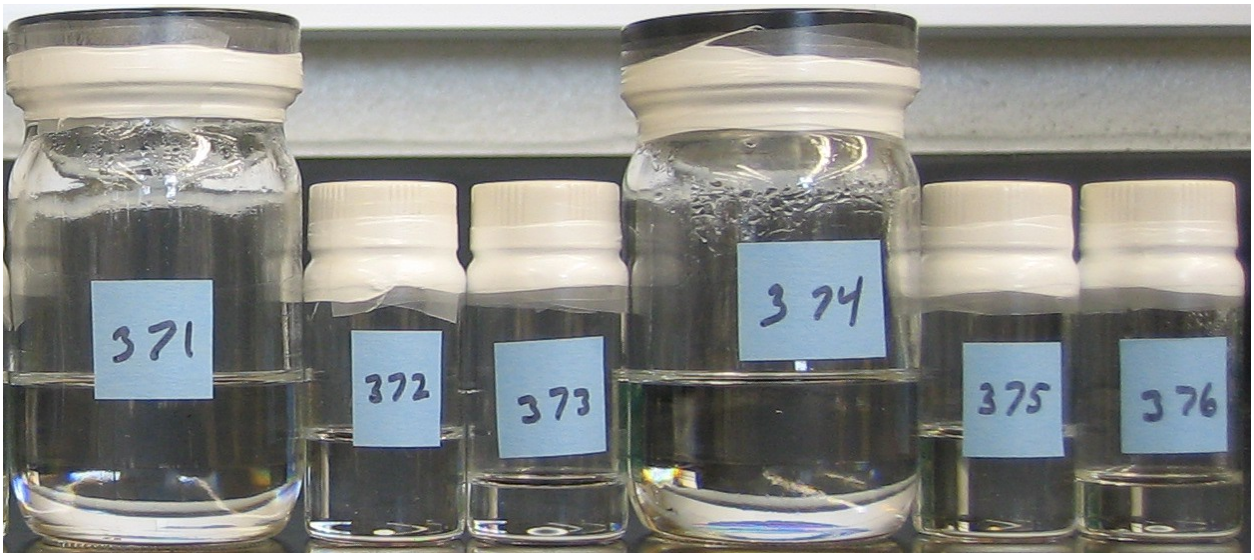

(b) Polystyrol 168N in toluene at 5 mg/mL (371), 25 mg/mL (372), and 50 mg/mL (373) and Polystyrol 168N with 3 v% 25NP crosslinked polystyrene nanoparticles in toluene at 5 mg/mL (374), 25 mg/mL (375), and 50 mg/mL (376).

Figure 5.1: Solutions of polymer and polymer-nanoparticle blends in toluene at three concentrations.

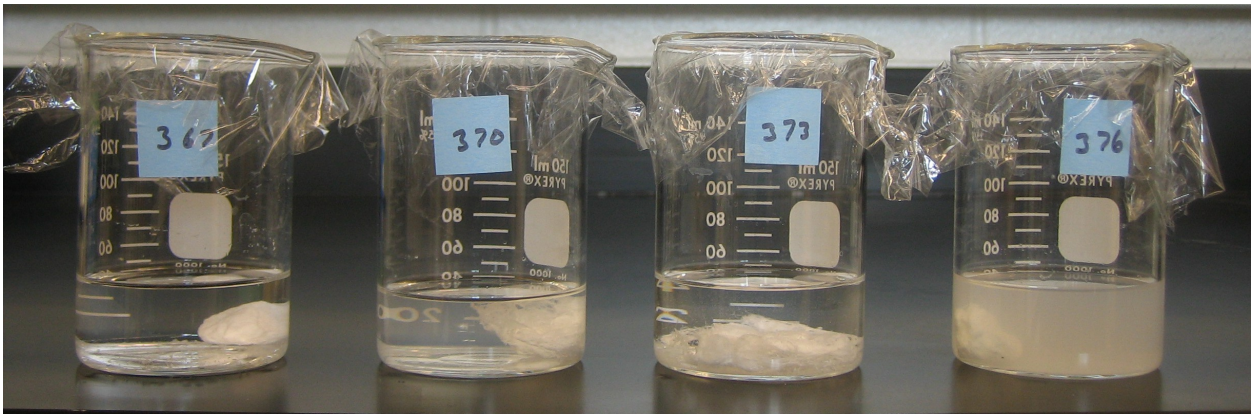

(a) Precipitates from 5 and 25 mg/mL 393 kD polystyrene solutions with and without crosslinked polystyrene nanoparticles. Supernatants in samples with nanoparticles are cloudy (370, 376).

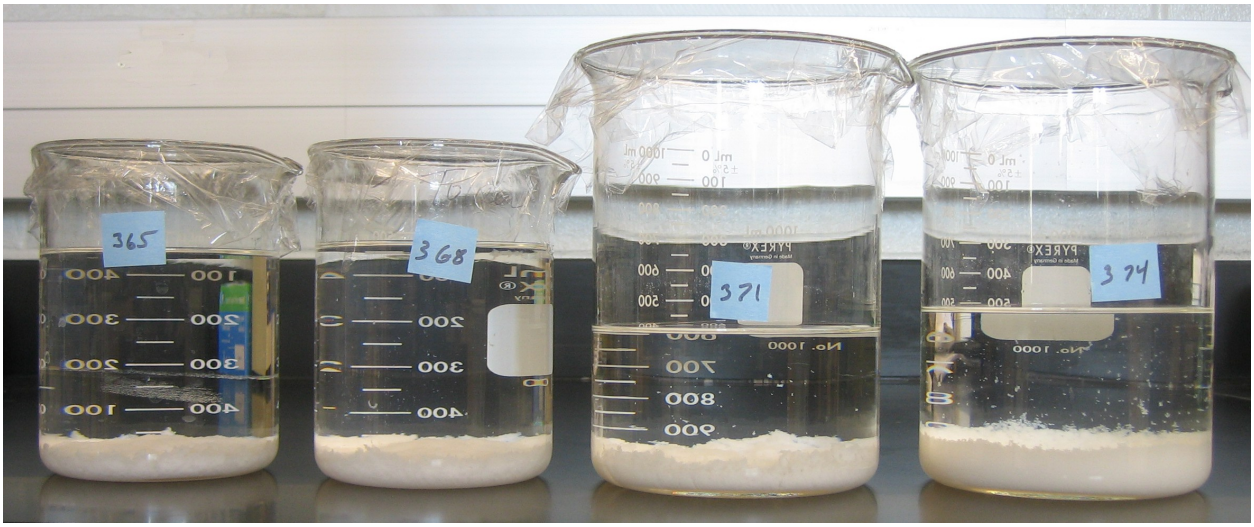

(b) Precipitates from 50 mg/mL 393 kD polystyrene solutions with and without crosslinked polystyrene nanoparticles. All supernatants are clear.

Figure 5.2: Precipitates of 393 kD polystyrene and 393 kD polystyrene with 3 v%25NP crosslinked polystyrene nanoparticles. Notice the cloudy supernatant in samples with nanoparticles precipitated from 5 and 25 mg/mL solutions.

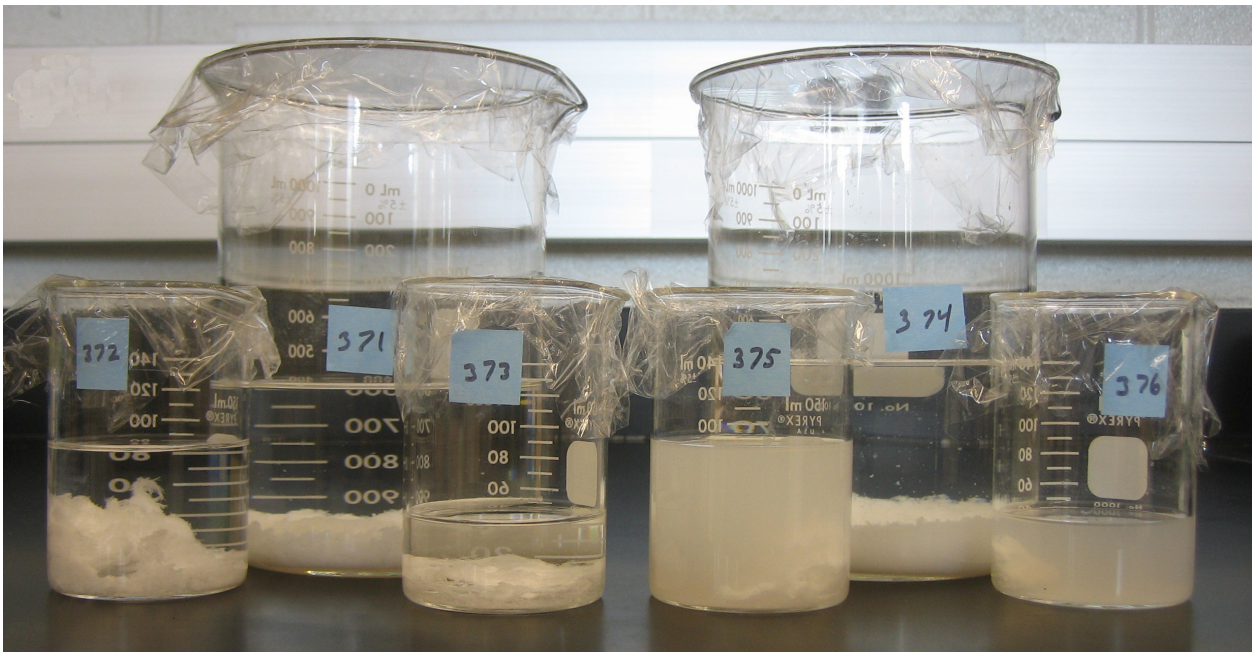

Figure 5.3: Precipitates of Polystyrol 168N and Polystyrol 168N with 25NP crosslinked polystyrene nanoparticles. Again notice the cloudy supernatant in samples with nanoparticles precipitated from 5 and 25 mg/mL solutions (375, 376).

25 mg/mL result in a phase separated system. While this does not prove conclusively that the polymer concentration is the primary issue, the limit falls very close to the overlap concentration for polystyrene at this molecular weight. In the next section we put this knowledge to use, dispersing oleic acid stabilized CdSe nanocrystals in polystyrene.

5.4 X-Ray Scattering of Polystyrene CdSe Nanocomposites

Directly measuring dispersion of polystyrene nanoparticles in linear polystyrene is quite difficult due to the similarity of intrinsic properties i.e., electron density, refractive index, etc. Even indirect methods such as scattering sufferer from the same limitations unless

neutron scattering is employed. To overcome this issue a nanoparticle with higher electron contrast, for this work oleic acid CdSe quantum nanocrystals (oa-QNC) dispersed in 393 kD linear monodisperse polystyrene standard was used. The heavy metal content of the CdSe provides a large amount of electron contrast relative to polystyrene. This allows the use of small angle x-ray scattering to determine the size of the nanocrystals, giving a measure of the dispersion in the polymer matrix.

X-ray scattering was done on a Rigaku Ultima IV with a copper anode, wavelength 1.54 Å, and single point scintillation crystal detector. Wide angle scans were run with the following settings: Scanning Mode = 2Theta, Scanning Type = FT, X-Ray Power = 40kV/44mA, Divergence Slit = 1.0 mm, Divergence Height Limiting Slit = 5 mm, Secondary Slit = 0.2 mm, Receiving Slit = 0.2 mm, Start Angle = 5°, Stop Angle = 65°, Step = 0.01°, Fixed Time = 5 s, and Theta = 10°. Small angle scans were run with the settings except these: Receiving Slit = 0.1 mm, Start Angle = 0.1°, Stop Angle = 5°, Step = 0.005°, Fixed Time = 3 s, and Theta = 0°. In order to properly scale the intensity for the SAXS profiles transmissions were also collected using Start Angle = -0.1°, Stop Angle = 0.1°, Step = 0.005°, Fixed Time = 0.5 s, Theta = 0° and 0.4 mm of Al absorber was added to attenuate the beam, preventing damage to the detector. The peak intensity of each transmission was compared to an empty cell peak to determine the absorption, see section 6.2. Experiments were run at room temperature.

The analysis technique employed will be the same as that used for SANS since the theory of the two experimental techniques are essentially the same. The primary difference between the two techniques being the nature of the electron and it's indefinite position, otherwise known as the electron cloud or orbital. A small correction is used to account

for this, Equation (5.1), where $r_e = 0.282 \times 10^{-5}$nm, electron or Thomson radius and $Z =$ Atomic Number though it does not effect the outcome significantly at low angle.

$$(\frac{\delta\Sigma}{\delta\Omega})(\Theta) = Z^2 r_e^2 \frac{1 + [cos(\Theta)]^2}{1} \tag{5.1}$$

In Figure 5.4 we see the one dimensional scattering profile, unlike the SANS work in Chapter 3 this instrument has a point detector so this profile is not from a two dimensional average. This is the raw data, uncorrected for thickness, sample transmission, and absolute intensity. We see the expected an increase in scattering intensity with nanoparticle concentration, however, the scaling of the intensity is definitely incorrect for the highest volume fraction since it has almost the same value as the next lowest. At the very least we expect the intensity to be proportional to the volume of the scatterer, $I(q) \propto I_0 V \frac{\delta\Sigma}{\delta\Omega}(q)$. This exemplifies the importance of properly correcting for sample thickness and transmission, furthermore to get the absolute intensity the instrument must be calibrated against a known standard. Though it is immediately obvious that sphere like particle with low polydispersity is present, indicated by the local peak.

In Figure 5.5 we see the thickness, transmission and absolute intensity corrected scattering profiles. It is now clear that the intensity is scaling correctly with the volume fraction of the scatterer and as in the Figure 5.4 we see a local peak indicating a spherical scatterer.

To further deduce the size of the scatter we turn to the Kratky plot ($q^4 I(q) vs q$), Figure 5.6, we see a more pronounced peak occurring at approximately the same q position for each volume fraction. Fitting a Gaussian peak to the profile we can determine the exact peak position in q-space. Then assuming a spherical scatterer we can calculate a characteristic scatterer size d, $q = 2.6/d$. The results of this analysis are list in Table 5.2. From this analysis

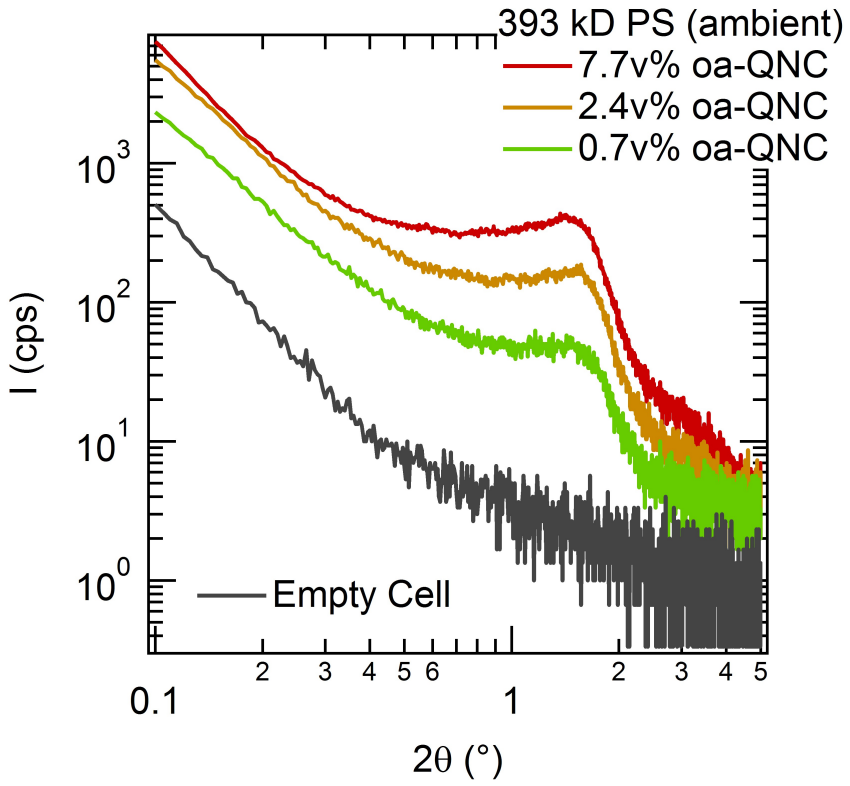

Figure 5.4: Scattering profiles of 393 kD linear polystyrene (393PS) with 3 different volume fractions of oleic acid stabilized CdSe nanocrystals (oa-QNC).

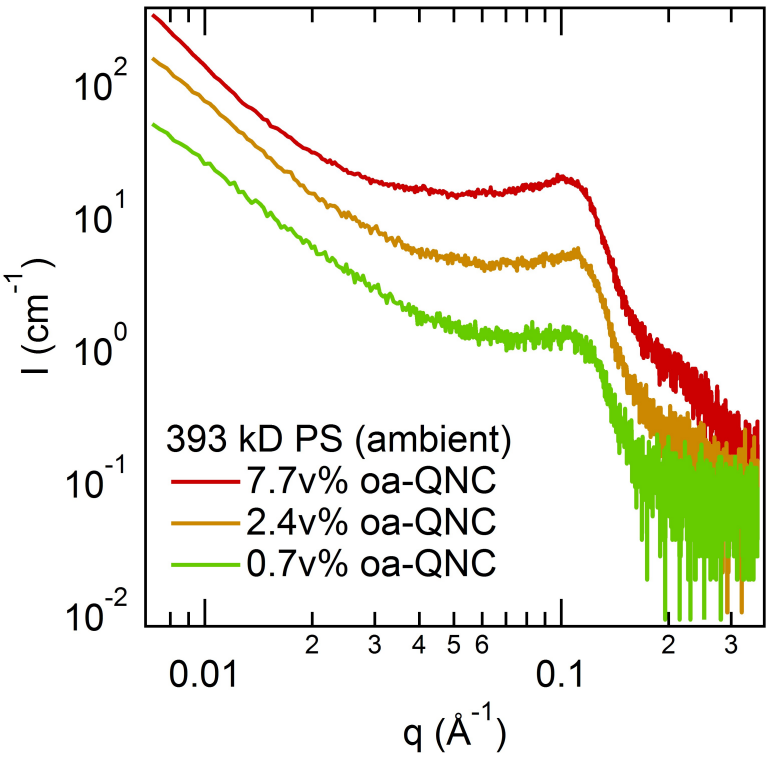

Figure 5.5: Absolute scattering profiles of 393 kD linear polystyrene (393PS) with 3 different volume fractions of oleic acid stabilized CdSe nanocrystals (oa-QNC).

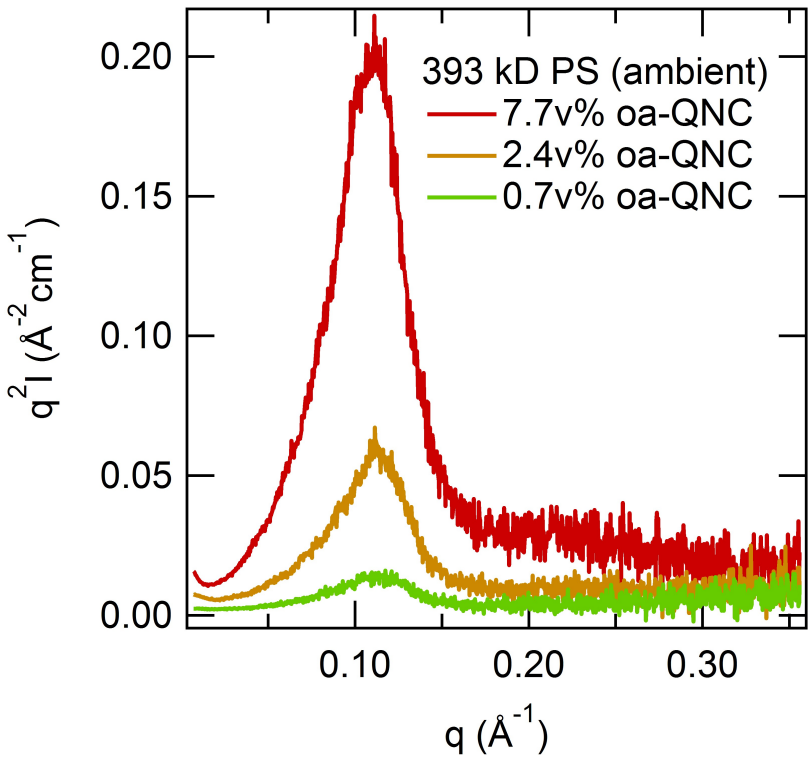

Figure 5.6: Kratky plots created from absolute scattering profiles of 393 kD linear polystyrene (393PS) with 3 different volume fractions of oleic acid stabilized CdSe nanocrystals (oa-QNC). Single peak is indicative of particle like structure.

we see the scatterers are all the same size, 2.3 nm, an excellent indication of dispersion. This value also corresponds well to the size determined by TEM, 2.2 nm.[63]

The final method for determination of dispersion will be though Guinier analysis. In Figure 5.7 we show Guinier plots ($Ln(I) vs q^2$) and by fitting the low q-region to $Ln(I(q)) = -(qR_g)^2/3 + Ln(I_0)$ we can determine the R_g of the scatterer as well as the intensity at zero wavevector, I_0, which could be used for subsequent analysis not relevant to this work. Again we are limited by $qR_g < 1$ especially for these nanoparticles which have a very low polydispersity. Using this analysis we see the same radius 2.3 nm however the variance increases significantly at the volume fraction of the nanoparticles decreases. At the lowest volume fraction the Guinier analysis was unable to converge on linear fit that satisfied the

Table 5.2: Peak positions determined from Gaussian peak fits to Kratky Plots, Figure 5.6, of 393 kD linear polystyrene (393PS) with three volume fractions of oleic acid stabilized CdSe Nanocrystals (oa-QNC). Characteristic length scale is reported using the following conversion, $q = 2.6/d$ based on a hard sphere scatterer.

PS M_w (kD)	oa-QNC (v%)	q_{Peak} (Å^{-1})	d (nm)
393	0.7	0.1111	2.3
393	2.4	0.1119	2.3
393	7.7	0.1091	2.3

Table 5.3: Results of linear fit to low q-region in Guinier Plots, Figure 5.7, of 393 kD linear polystyrene (393PS) with three volume fractions of oleic acid stabilized CdSe Nanocrystals (oa-QNC).

PS M_w (kD)	oa-QNC (v%)	R_g (nm)	±	I_0 (cm^{-1})	±
393	0.7	-	-	-	-
393	2.4	2.3	1.0	6.8	1.3
393	7.7	2.3	0.7	20.2	1.0

$qR_g < 1$ limit. Again this is most likely do to the low volume of scatterers and proximity to the primary x-ray flux. The results of the Guinier analysis are listed in Table 5.3. The intensity at zero wavevector (I_0)is also reported but no subsequent analysis was preformed.

5.5 Summary

It is clear that choosing the proper concentration is crucial to the success of blending polymer chains and nanoparticles via rapid precipitation. It appears that using polymer concentrations below the overlap concentration are key, though this was not proven unequivocally. Regardless is it important to see the precipitates settle out in a short amount of time and that they are uniform in texture and color. Permanent suspension of some solids is a definite

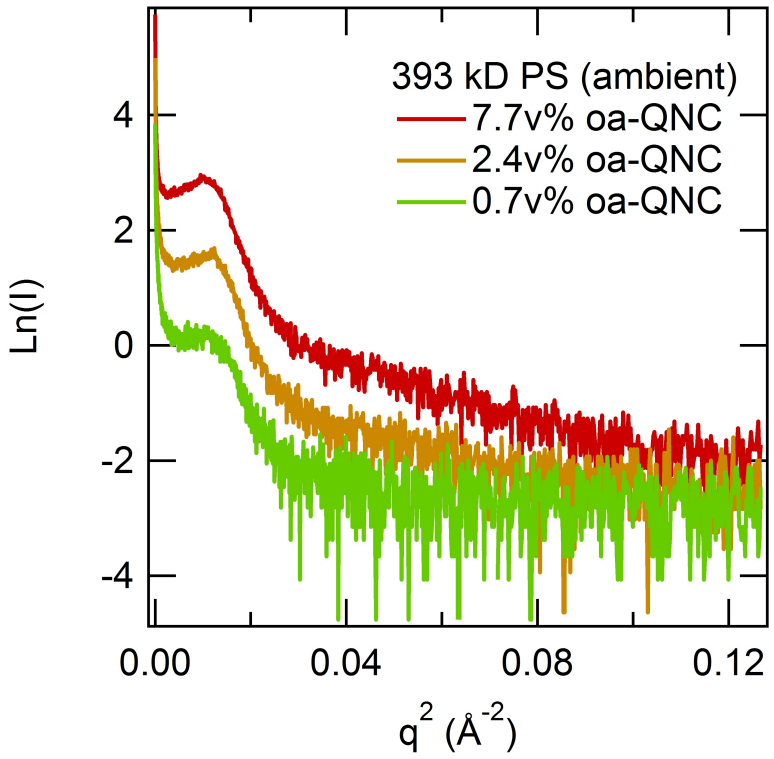

Figure 5.7: Guinier plots created from absolute scattering profiles of 393 kD linear polystyrene (393PS) with 3 different volume fractions of oleic acid stabilized CdSe nanocrystals (oa-QNC).

indication of phase separation and separation via filtering will lead to a very heterogeneous solid.

Using this knowledge we were able to produce a set of composites with oleic acid stabilized quantum nanocrystals dispersed in polystyrene. The dispersion was characterized by small angle x-ray scattering. Even at several different volume fractions proper use of rapid precipitation created a composite with well dispersed nanoparticles even though the solubilizing layer as a bulk liquid is incompatible with polystyrene.

Chapter 6

Experimental Techniques

6.1 Rheology

The field of rheology encompasses the flow and deformation of matter. This wide ranging definition covers a variety of materials and methods. From macroscopic to microscopic, experiments and theory the field of rheology covers a wide variety of materials and methods. At its core it is the study of deformation by two interrelated mechanisms; force or stress and displacement or strain. In this section I will cover the basics related to the rheological studies done as part of this work.

6.1.1 Simple Shear

One of the most basic deformations, simple shear, is described by the flow field in Equation (6.1) and (6.2). If material was sandwiched between two plates of infinite area and one of the plates were subjected to a constant velocity in x relative to the other a simple shear flow would be produced.

$$V_x = f(x, y) \tag{6.1}$$

$$V_y = V_z = 0 \tag{6.2}$$

In a stress-controlled rheometer a constant force is supplied to move on of the plates the stress (σ) on the system will be known and the resulting displacement Δx can be measured and given a known sample thickness (h) the strain (γ) can be determined. The opposite is true for a strain-controlled rheometer, the stain is supplied and the force is measured. In either method a time dependent modulus G(t) can be calculated via Equation (6.3)[7]. If

the strain rate is also known then the viscosity under those measurement conditions can be determined.

$$G(t) \equiv \frac{\sigma(t)}{\gamma_0} \tag{6.3}$$

Unfortunately no instrument has infinitely large plates to work with so other geometries were developed to mimic this flow and various limitations an errors for each have been well studied.[105] The geometry most often utilized in this work is the 8-mm parallel plate. Parallel plates work by turning one plate relative to the other along a central axis. Although the stress field is inhomogeneous they can replicate the infinite plate since they can be continuously turned without losing contact with the sample. They are well adapted for use with polymer since it is rather easy (compared to other geometries) to make samples that fill them appropriately.

6.1.2 Oscillatory Shear

Steady shear poses a problem to polymeric systems, the constant shearing will pull chains into a non-equilibrium state. Typically this will permanently damage the sample but even a subtle over straining will pull chains out of their entanglement (tubes) without allowing them to re-entangle (re-enter a new tube) rendering the sample unsuitable for study. To over come this oscillatory shear is used. Instead of a constant shear direction the strain (or stress) follows a sinusoidal amplitude, Equations (6.4) and (6.5), passing back through zero. This technique, if used properly i.e., in the linear region, the polymer will remain in equilibrium through out the test (baring thermal degradation).

$$\gamma = \gamma_0 \sin \omega t \tag{6.4}$$

$$\sigma(t) = \sigma_0 \sin \omega t + \delta \tag{6.5}$$

In order to determine the linear region the material must be subjected to a strain sweep, typically under the conditions where the sample is most stiffest, low temperature and high frequency. In Figure 6.1 we show a typical strain sweep, in this example a hyperbranched polystyrene-anhydride nanoparticle supplied by BASF. The strain sweep was run from 0.01 to 100% strain, at 100 rad/s (typical upper end of a frequency sweeps) and 130 °C (typical starting temperature for polystyrene, $T_g + 25$ °C). Referring again to Figure 6.1 a large linear region (plateau in G', G" and $\eta*$) exists from approximately 0.01% strain up to 10% strain above 10% strain both the storage and loss modulus (and there for the viscosity) begin decreasing slightly with a sharp drop off (non-linear response) above 20% strain also called the non-linear region. The usable non-linear region ends around 60% strain where you can see the torque begin to decease, this is a classic sign of sample failure most likely do to edge fracture. Beyond 60% strain the sample is no longer in contact with the plates and the data should be ignored. Subsequent experiments (such as a frequency temperature sweep) with this material should be run at a maximum strain of 10% to ensure a linear response. The measured linear region will remain valid for all temperatures higher than 130 °C and frequencies lower than 100 rad/s.

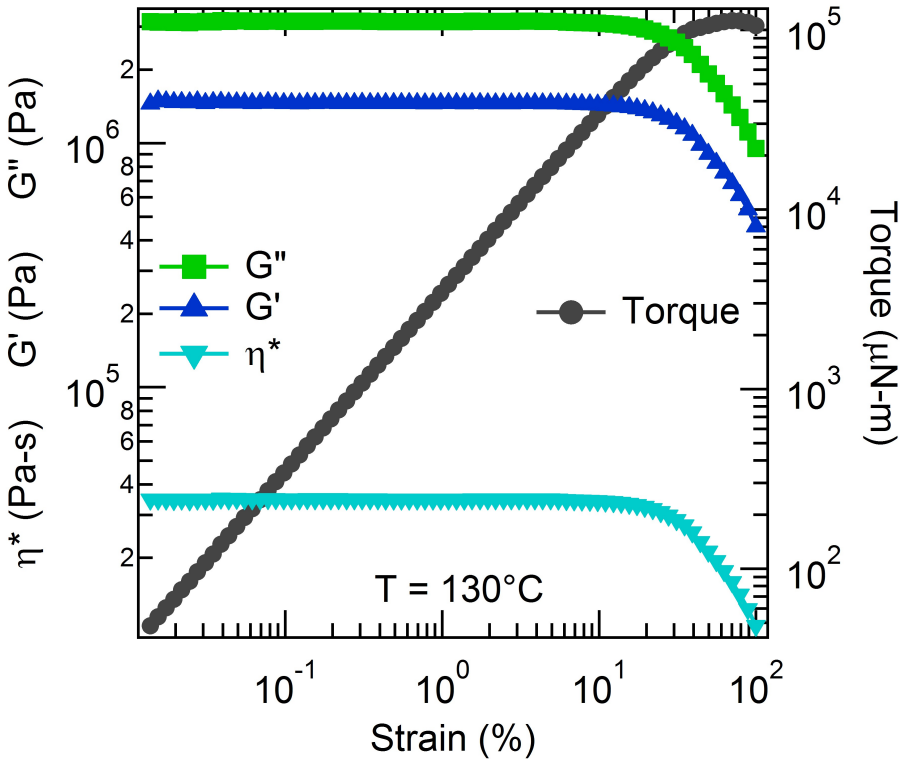

Figure 6.1: Strain sweep of GK1604/23 hyperbranched polystyrene-anhydride nanoparticle run at 130 °C and 100 rad/s. Linear region extends from 0.01 to 10% strain.

Table 6.1: Complex viscosities from PDMS standard at a single point oscillatory test at 0.1 rad/s and ever decreasing plate gaps.

Gap (mm)	1/Gap (mm^{-1})	$\eta * (\omega = 0.1 rad/s)$ (KPa-s)
0.986	1.01	0.709
0.897	1.11	0.541
0.796	1.26	1.943
0.695	1.44	0.805
0.595	1.68	1.256
0.497	2.01	1.163
0.377	2.65	1.024
0.286	3.50	1.282
0.231	4.33	0.907
0.185	5.41	1.106
0.144	6.94	1.019
0.096	10.4	0.257
0.048	20.8	0.158

6.1.3 Plate Alignment

Ensuring proper plate alignment is crucial to the accuracy of experimental results in parallel plate and cone-and-plate geometries. The simplest method for determining alignment is a series of measurements while decreasing the gap. Eventually the scale of any misalignment (axial center, normal vector alignment) will become on the order of the plate gap. Simply put the miss alignment will become a large factor in the measurement. All shear experiments in this dissertation use 8-mm parallel plates for which the alignment was checked with high viscosity PDMS standard provided by TA Instruments. A series of single point oscillatory test at 0.1 rad/s and ever decreasing plate gap were run at room temperature, the results of which are listed in Table 6.1 below.

In Figure 6.2 the measured viscosity at 1 rad/s for several the plate gaps (h) are plotted. It is immediately obvious there is a sharp drop off in the terminal viscosity around 0.1 mm,

indicating the lower usable limit. Above 0.1 mm the terminal viscosity is independent of the plate gap, though the values start to vary wildly above 0.6 indicating the upper limit. The gap used for all of the system studied in this work was between 0.18 mm and 0.36 mm well within the usable range.

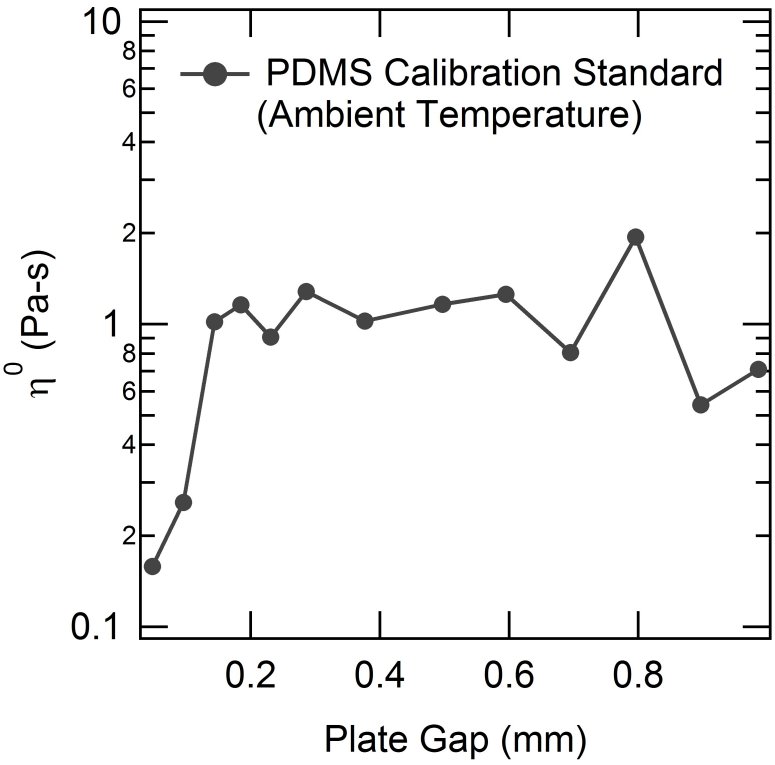

Figure 6.2: Complex viscosity of PDMS standard at different plate gaps. The drop off in viscosity denotes the lower usable gap with the current alignment.

6.1.4 Wall Slip

6.1.5 Sample Stability

Ensuring samples are stable during the course of an experiment is very important to gain the full understanding of the system being studied. If the polymer degrades or if a suspension

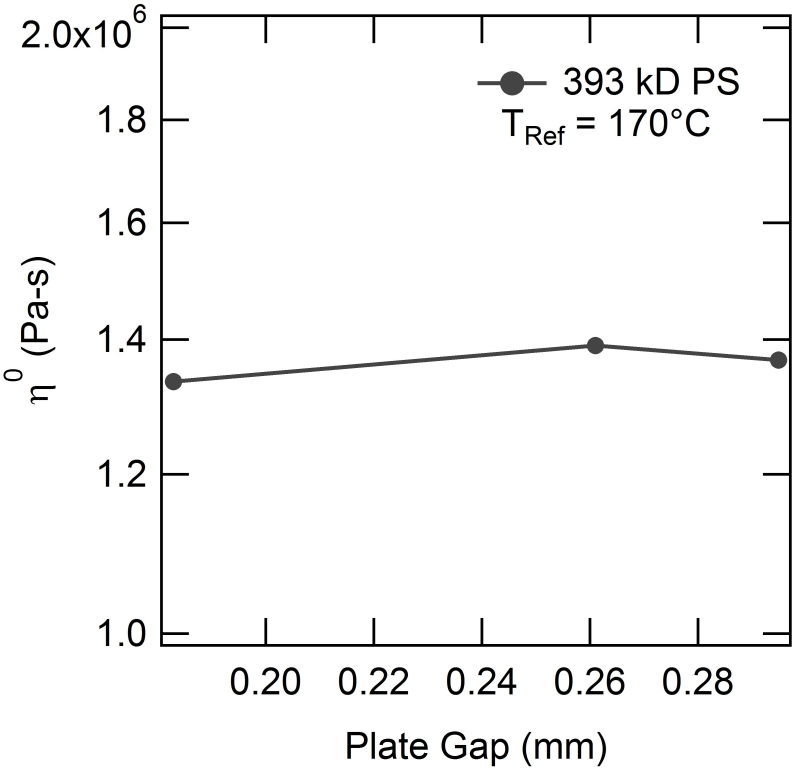

Figure 6.3: Terminal viscosity of 393 kD polystyrene standard at different plate gaps. The stable value indicates no wall-slip is present.

collapses over the course of a frequency-temperature sweep Boltzmann-Time-Temperature superposition will sometimes fail or worse it will work but the results are the combination of a non static system. One quick check that can be done is the classic hysteresis loop. For the case of a frequency temperature sweep returning to one of the lower temperature at the end of an experiment will give a good indication of the stability of the system being studied.

In Figure 6.4 we show sweeps of poly(styrene-co-acrylonitrile) with cross linked poly(styrene-co-acrylonitrile) nanoparticles. The 1^{st} cycle frequency sweep was measured during the typical frequency-temperature sweep (130, 150, 170, 190, 210 °C) used to make a master curve, the second frequency sweep was measured following the last frequency sweep (210 °C) during the frequency-temperature sweep experiment. As you can see the two frequency sweep are

in excellent agreement, which is typical for most of the system report in this dissertation, indicating the stability of the nanoparticle dispersion during the course of the frequency temperature sweep.

6.2 SAXS

6.2.1 Absolute Intensity Calibration

Bench top x-ray instruments are readily available from several manufacturers. Modern machining and control techniques allow their use as a small angle x-ray scattering (SAXS) instruments, over a limited yet useful range. Typically bench top setups are employed to measure size scales with SAXS. However, subsequent analysis requires absolute intensity, which is unknown. In order to determine the absolute intensity a correction factor is employed. The correction factor is determined by scattering from a well characterized standard, in the this case glassy carbon supplied and characterized at the Advanced Photo Source (Argonne National Lab).[92] By measuring the standard on the bench top instrument a simple scaling factor can be calculated. The procedure and equations are taken directly from Dreiss' paper on the subject.[106] The characteristic momentum scattering Equation (6.6) is shown below.

$$I_S(q) = \frac{N_S(q)}{t_S} = I_0(\lambda) A \Delta\Omega \eta(\lambda) T_S(\lambda) d_S \frac{\delta\Sigma}{\delta\Omega}(q) + BG_S \tag{6.6}$$

The scattering intensity, $I_S(q)$, is the measured quantity of photons, $N_S(q)$, detected per unit time, t_S, where $q = 4\pi/\lambda \sin(\frac{\Theta}{2})$. $I_0(\lambda)$ is the incident x-ray flux which is itself a function of wavelength, λ. A is the illuminated area, $\Delta\Omega$, is the solid angle element

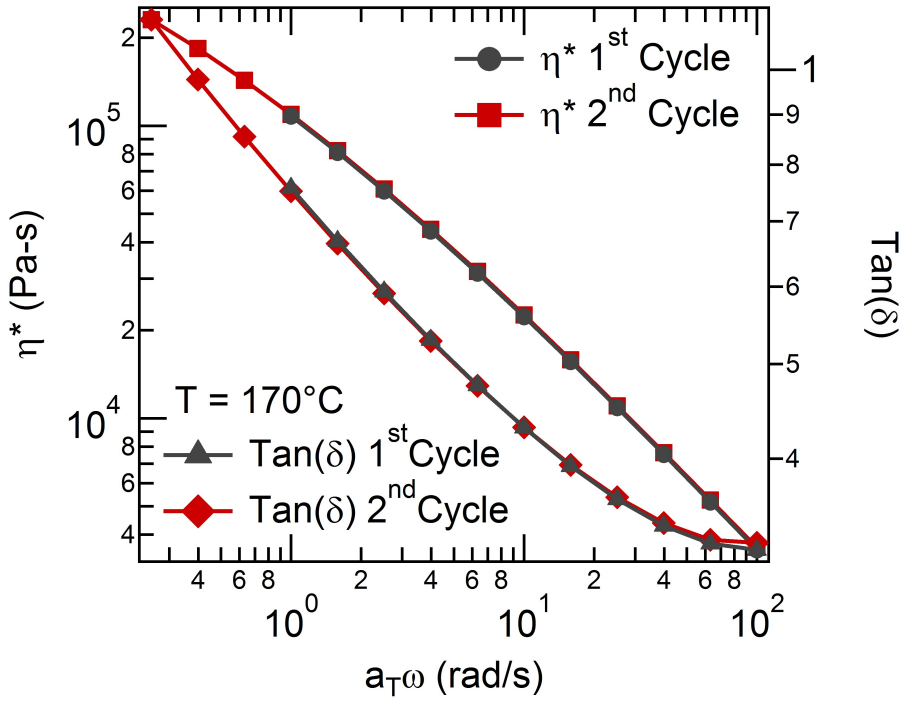

(a) Complex Viscosity

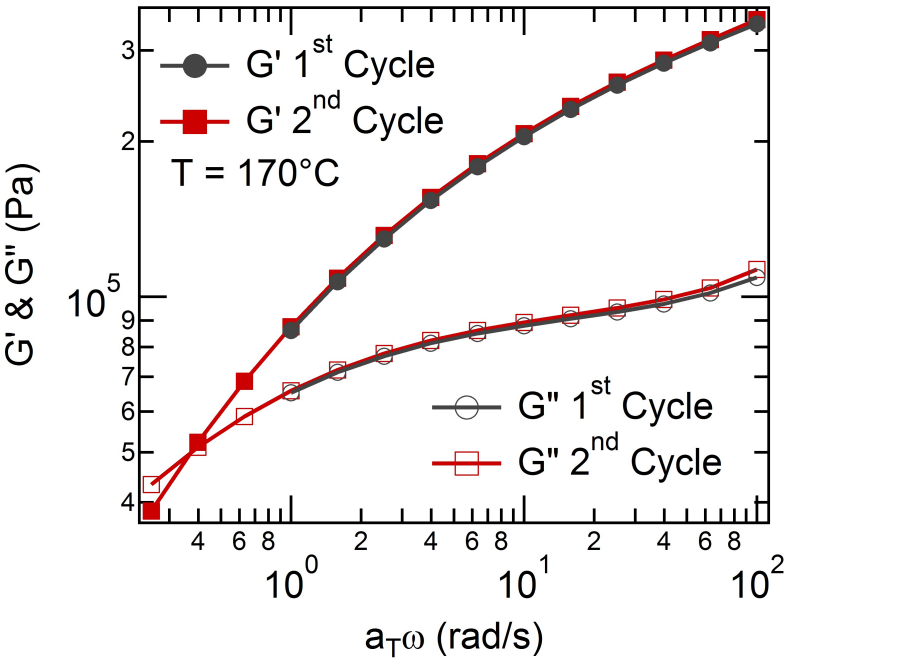

(b) Storage & Loss Moduli

Figure 6.4: Frequency sweeps at 170 °C poly(styrene-co-acrylonitrile) with cross linked poly(styrene-co-acrylonitrile) nanoparticles. Overlap of material properties indicated stability of system during the time frame of the typical experiment.

(pixel detector size), $\eta(\lambda)$ is the detector efficiency (a function of wavelength), $T_S(\lambda)$ is the sample transmission (a function of wavelength), d_S is the sample thickness and BG_S is the background. The calibration for our instrument will use $(\frac{\delta\Sigma}{\delta\Omega})_s$, the differential scattering cross section of a well characterized standard (Glassy Carbon). The differential scattering cross section of a sample can be determined by Equation (6.7), where 's' indicates the sample and "st" indicates the Glassy Carbon Standard. Background scattering typically very weak and can be ignored.

$$(\frac{\delta\Sigma}{\delta\Omega})_s(q) = (\frac{\delta\Sigma}{\delta\Omega})_{st}(q)\frac{[I_s(q) - BG_S]}{d_S T_S}\frac{d_{st}T_{st}}{[I_{st}(q) - BG_{st}]} \tag{6.7}$$

If the standard and sample are measured under identical conditions the remaining variables from Equation (6.6) cancel out. The calibration factor can be derived from all of the "st" labeled variables, Equation (6.8) below. Accurate measurements of the calibration standard can then be used to correct unknown samples.

$$CF = (\frac{\delta\Sigma}{\delta\Omega})_{st}(q)\frac{d_{st}T_{st}}{[I_{st}(q) - BG_{st}]} \tag{6.8}$$

Once the correction factor has been determined the differential scattering cross section of an unknown sample can be calculated from Equation (6.9), below.

$$(\frac{\delta\Sigma}{\delta\Omega})_s(q) = CF \times \frac{[I_s(q) - BG_S]}{d_S T_S} \tag{6.9}$$

Table 6.2: Instrument configuration for transmission measurements.

Scanning Mode	=	2Theta
Scanning Type	=	FT
Source Voltage	=	40kV
Source Current	=	44 mA
Divergence Slit	=	1.0 mm
Divergence Height Limiting Slit	=	5.0 mm
Secondary Slit	=	0.2 mm
Receiving Slit	=	0.1 mm
Start	=	-0.100°
Stop	=	0.100°
Step	=	0.005°
FT	=	0.5 s
Fixed Angle (Theta)	=	0°
Al absorber thickness	=	0.4 mm

6.2.2 Experimental Setup

Glassy carbon sample was provided by Jan Ilavsky at APS, labeled as Glassy Carbon L18. The sample was characterized at APS on 32ID-B USAXS line. Differential scattering cross section as a function of wavevector was supplied for calibration of local instruments. The glassy carbon sample thickness is 0.100 cm which was confirmed locally. Rigaku UltimaIV was warmed up to 40kV at 44mA for 30 minutes. This instrument has a copper source providing a x-ray wavelength of 1.54Å(Cu K_α). Standard automatic alignment procedure for SAXS was followed. Tables 6.2 and 6.3 detail the instrument configuration for transmission and SAXS measurements. Al absorbers were used during the transmission to prevent damage to the detector. 5 empty cell measurements and 5 sample measurements were conducted for each configuration. Intensities are reported in counts per second (cps). In x-ray nomenclature the scattering angles are reported as 2Θ (this is not $2 \times \Theta$) for this work the scattering angles are converted to q-space using $q = 4\pi/\lambda \sin(\frac{\Theta}{2})$.

Table 6.3: Instrument configuration for SAXS measurements.

Scanning Mode	=	2Theta
Scanning Type	=	FT
Source Voltage	=	40kV
Source Current	=	44 mA
Divergence Slit	=	1.0 mm
Divergence Height Limiting Slit	=	5.0 mm
Secondary Slit	=	0.2 mm
Receiving Slit	=	0.1 mm
Start	=	0.070°
Stop	=	5.000°
Step	=	0.005°
FT	=	0.5 s
Fixed Angle (Theta)	=	0°

It is important to note that this calibration is only valid for the slit configurations listed in Table 6.3, changes to the source flux or detector flux will result in a different correction factor, see Equation (6.6). However using a different q-range does not change the correction factor. Changes to the transmission setups will not effect the result.

6.2.3 Results

6.2.3.1 Absorbance

The results for the peak intensities for the empty cell runs and glassy carbon standard are list in Table 6.4. The calculated transmission of the glassy carbon, $T_{st} = 0.538 \pm 0.011$, is in excellent agreement with Dreiss' reported value, (0.527 ± 0.003), with a similar sample[106] and within the acceptable transmission range of 1/3 to 2/3.

Table 6.4: Intensity at 0 angle for an empty cell (EC) and L18 glassy carbon (GC) sample.

Run	EC Peak Intensity cps	GC Peak Intensity cps
1	21311	11507
2	20822	11122
3	21365	11559
4	21712	11600
5	21092	11432
Average	21260	11444
Standard Deviation	296	170

Table 6.5: Intensity at q=0.06Å (interpolated) for an empty cell (EC) and L18 glassy carbon (GC) sample.

Run	EC $I(q = 0.06)$ (cps)	GC $I(q = 0.06)$ (cps)
1	3	2138
2	3	2240
3	5	2261
4	4	2207
5	2	2153
Average	3	2200
Standard Deviation	1	48

6.2.3.2 SAXS

In Figure 6.5 I show the differential scattering cross section vs wavevector q (provided by APS) and the scattering intensity vs wavevector q (measured locally) of the L18 Glassy Carbon standard provided by APS. Overall the two curves are in excellent agreement. However there are slight differences in the plateau region, similar to those experienced by Dreiss.[106] To avoid including unnecessary error in the calibration factor the data from our instrument will be corrected at q=0.06 Å. The intensities at q=0.06 Åare listed in Table 6.5.

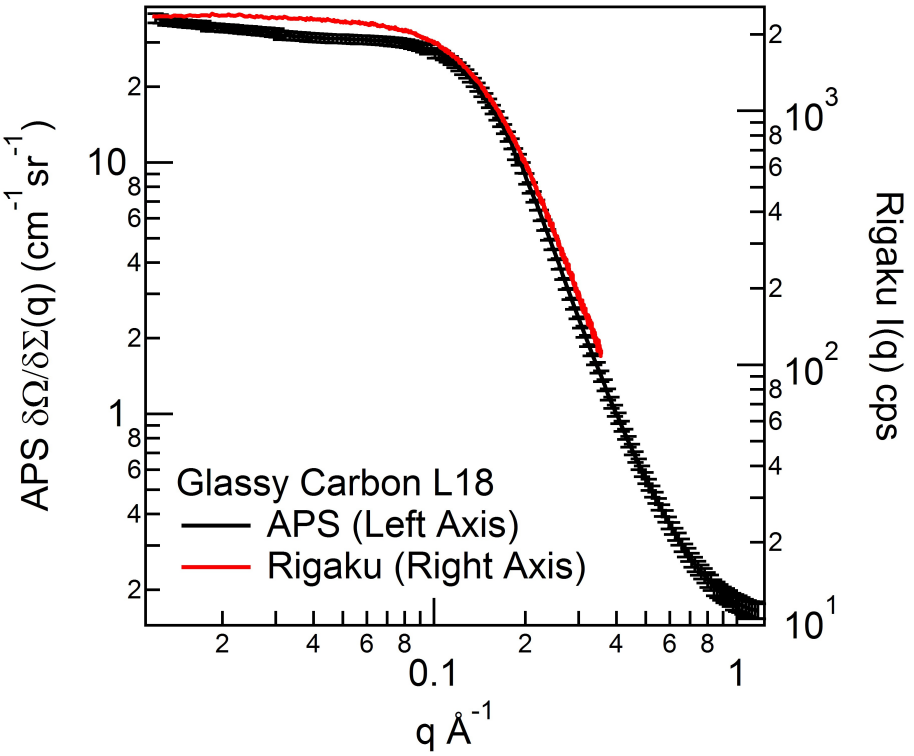

Figure 6.5: Differential scattering cross section and scattering intensity for glassy carbon standard.

Table 6.6: Differential scattering cross section (APS) and intensity (Rigaku) of L18 Glassy Carbon Stand at q=0.06Å.

Instrument	$I(q = 0.06)$	Units
Rigaku UltimaIV	2196	cps
32ID-B (APS)	30.7087	$cm^{-1}sr^{-1}$

6.2.3.3 Correction Factor

Using Equation (6.8) the correction factor was calculated to be $\frac{30.71cm^{-1}(0.1cm \times 0.537)}{2196phs^{-1}} = 7.51 \times 10^{-4}\frac{s}{sr-ph}$. This value was then applied to Equation (6.9), treating the standard as an unknown sample. The resulting corrected value is shown in Figure 6.6 along with the original differential scattering cross section from APS.

6.2.4 Summary

The correction factor for the Rigaku UltimaIV was determined to be $7.51 \times 10^{-4}\frac{s}{sr-ph}$. This value can be used with the scattering intensity, transmission and thickness to calculate the differential scattering cross section of an unknown sample. In the future the correction factor will be calculated as a function of wavevector, $CF(q)$, and error will be included to achieve a more robust correction.

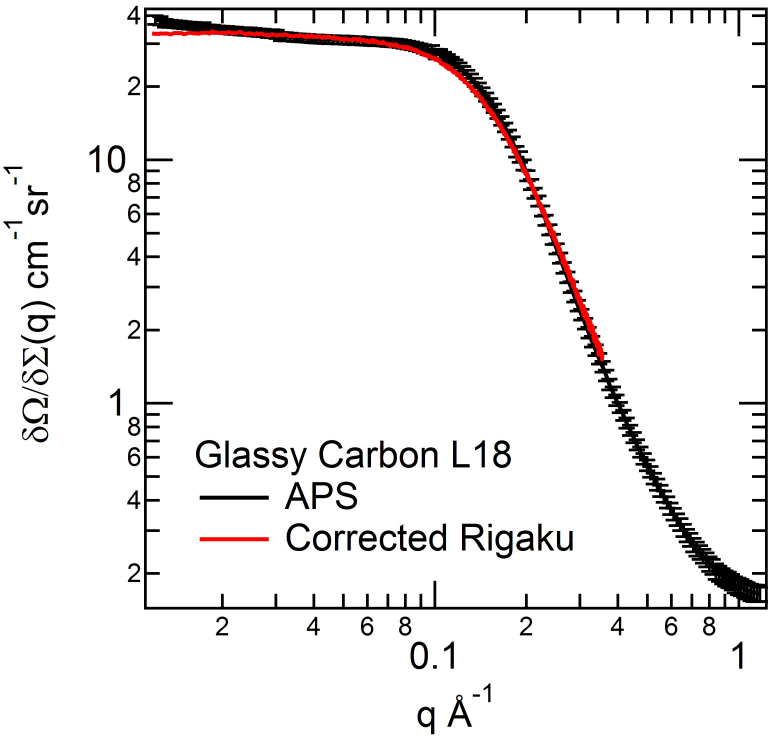

Figure 6.6: Differential scattering cross section of glassy carbon from APS and Rigaku (corrected).

Chapter 7

Conclusions

In this work polymer-nanocomposites with well dispersed spherical nanoparticles were studied to learn more about the reduced viscosity phenomena. The solubility of nanoparticles in polymer melts and confinement aspect nanoparticles on polymer chains with respect to reduced viscosity were studied using bimodal blends. The sensitivity of viscosity reduction to confinement limits was investigated by leaving a portion of the bimodal linear chains unconfined. Determined the partial confinement does not produce a complete reduction, indicating the nanoparticle's effect on the polymer chains must be uniform throughout the sample. The sensitivity to nanoparticle solubility was also studied, again by choosing a low molecular weight linear component of the bimodal blend that the nanoparticles would be insoluble in. The same technique was used to measure viscosity reductions with partial solubility. Similar to the confinement limit if the nanoparticles are insoluble in some of the chains the reduction is suppressed. In the insoluble case the viscosity follows that of Einstein's relation. Then with a more through grasp of these limits a polydisperse-polydisperse polymer-nanocomposite with reduced viscosity was created.

Next the dispersion of ideal nanoparticles in a polymer melt was characterized via neutron scattering and compared to separate rheological experiments. This provided a direct relationship between reduced melt viscosity and nanoparticle dispersion. Systems with well dispersed nanoparticles exhibit a reduced viscosity. Agglomerated system exhibit an increased viscosity following Einstein's relation[4]. Mixing energy scaling with (a/R_g) follows mixing theory of Mackay and co-authors[20]. Also rapid precipitation produces well dispersed system regardless of solubility and lack of confinement or solubility drive a phase separation upon annealing.

Finally attempts to make a PMMA-nanocomposite with reduced viscosity and increased toughness gave mixed results. Using C_{60} and Fe_3O_4 nanoparticles nanocomposites with reduced viscosity were made but only one volume fraction of Fe_3O_4 resulted in an increased Young's Modulus. The remaining systems followed the Mori-Tanaka theory for infinitely stiff additives. Concentration limits for blending polystyrene and crosslinked polystyrene nanoparticles were identified, these limits were then used for preparing subsequent samples.

Moving forward a clear understanding of the phase separation and viscosity of nanoparticles below the confinement limit should be investigated. The diffusion characteristic of nanoparticles with should be studied with well defined chemically similar (to the suspending polymer) at a few nanoparticle radii to compare reduced viscosity to nanoparticle size and hence diffusion. With the diffusion-viscosity relationship being compared by volume fraction, confinement ratio ($h/R_g < 1$), and normalized by a viscosity increase to the Rouse limit by the nanoparticles.

APPENDIX

Appendix A

Master Curves of Bimodal Poly(styrene) Blends With Cross Linked Polystyrene Nanoparticles

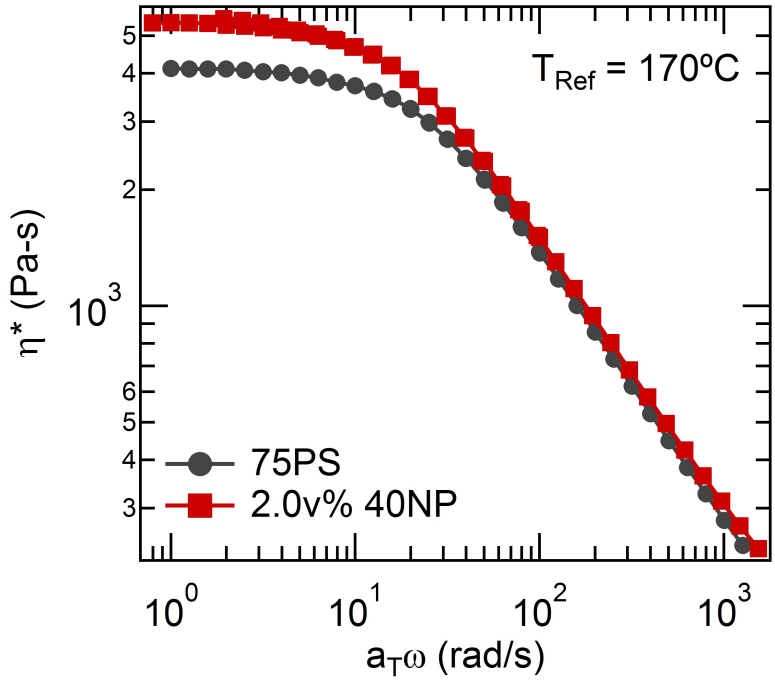

(a) Complex Viscosity

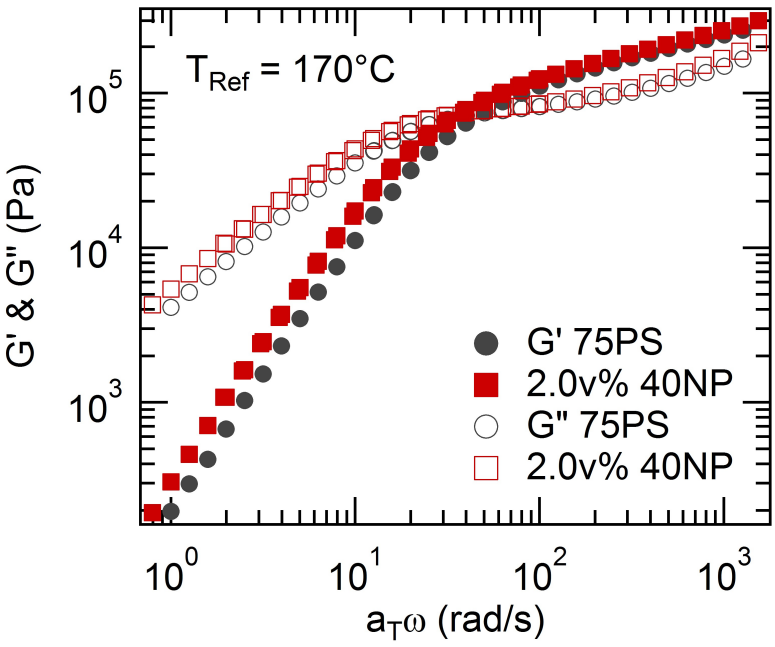

(b) Storage & Loss Moduli

Figure A.1: Master curves of 75 kD polystyrene with two volume fractions of 25NP cross linked polystyrene nanoparticles. Results shifted to a reference temperature of 170 °C.

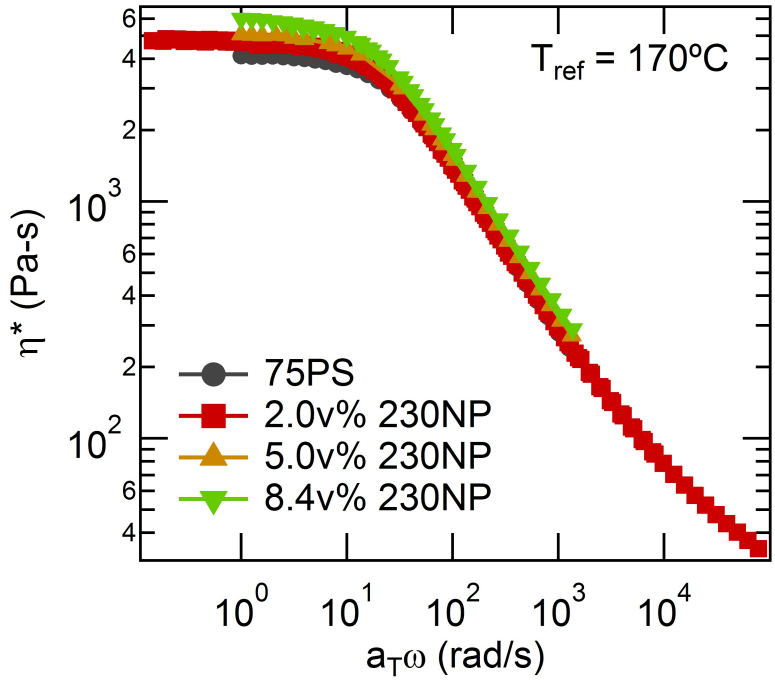

(a) Complex Viscosity

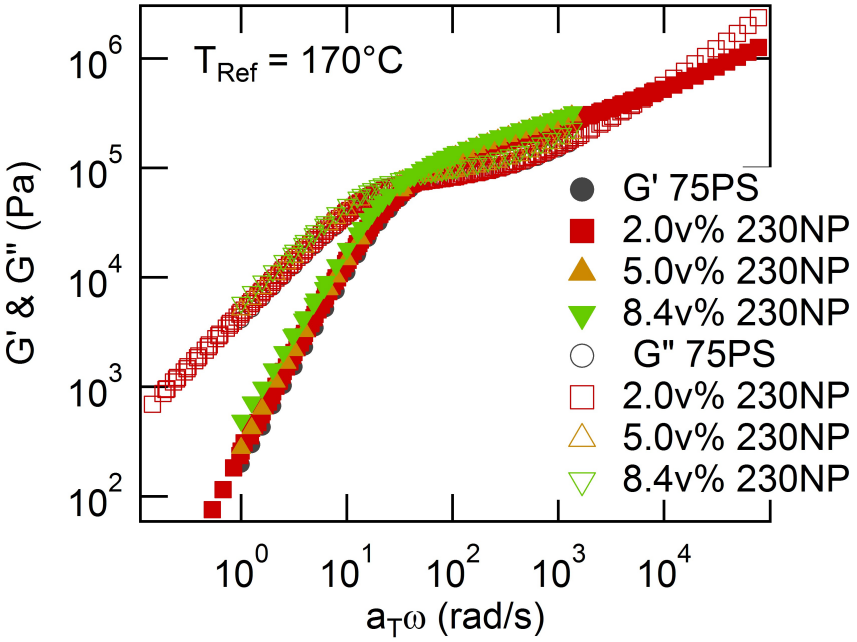

(b) Storage & Loss Moduli

Figure A.2: Master curves of 75 kD polystyrene with three volume fractions of 140NP cross linked polystyrene nanoparticles. Results shifted to a reference temperature of 170 °C.

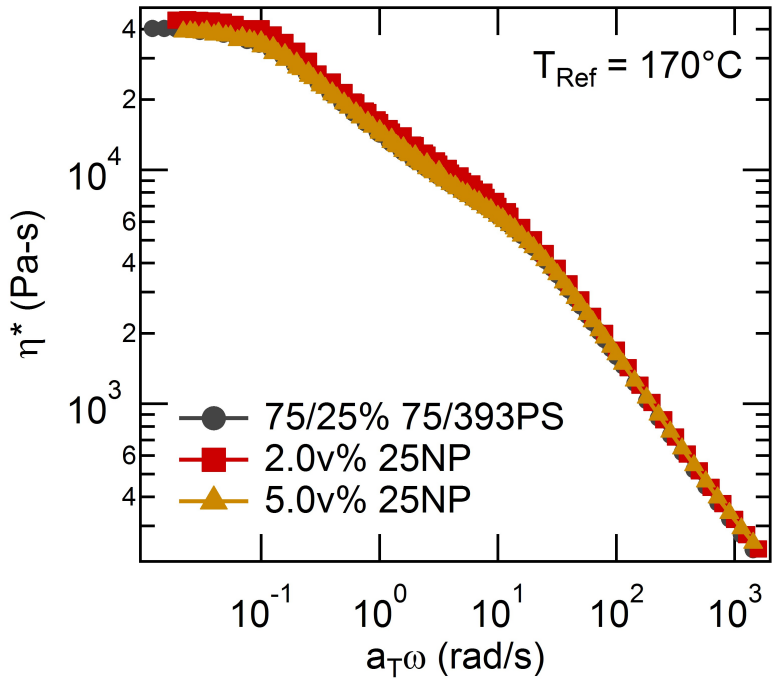

(a) Complex Viscosity

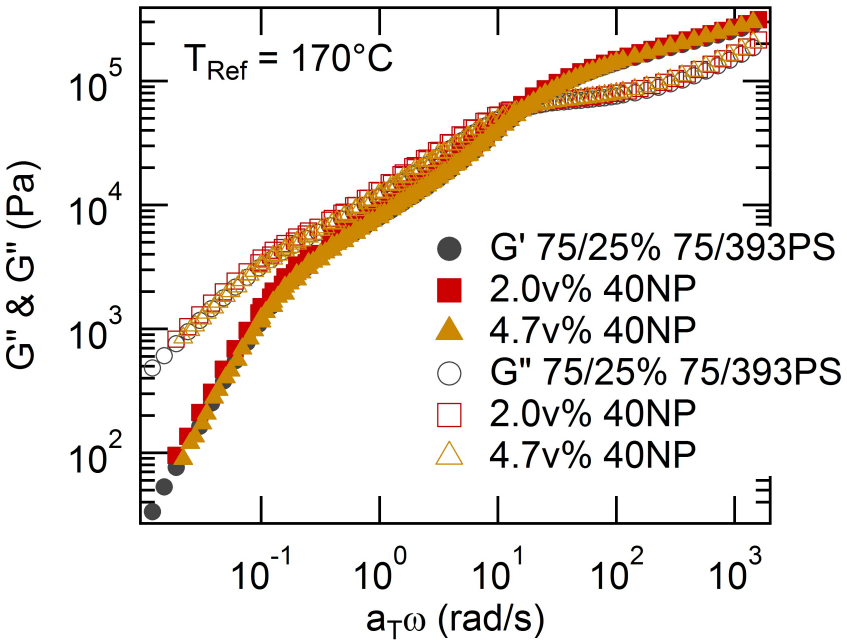

(b) Storage & Loss Moduli

Figure A.3: Master curves of 75/25% 75/393 kD polystyrene with two volume fractions of 25NP cross linked polystyrene nanoparticles. Results shifted to a reference temperature of 170 °C.

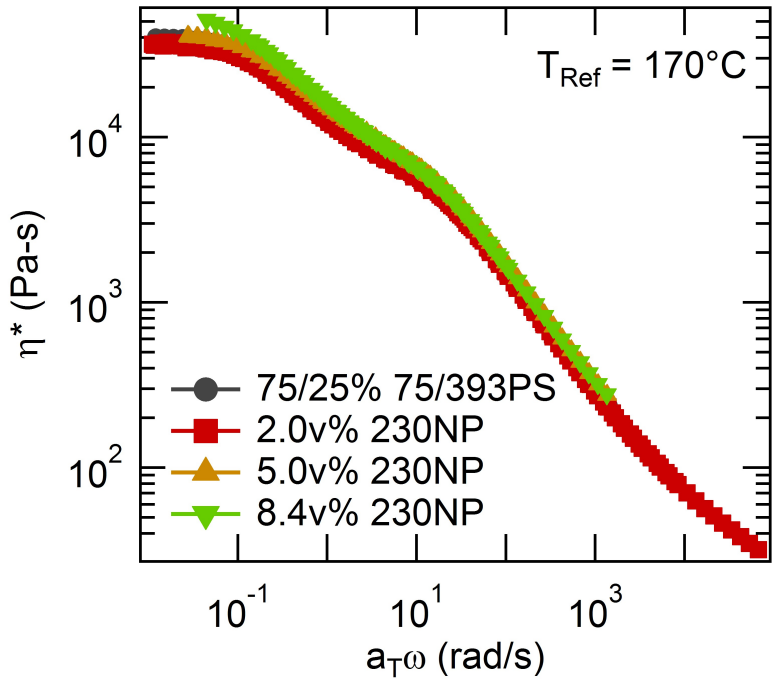

(a) Complex Viscosity

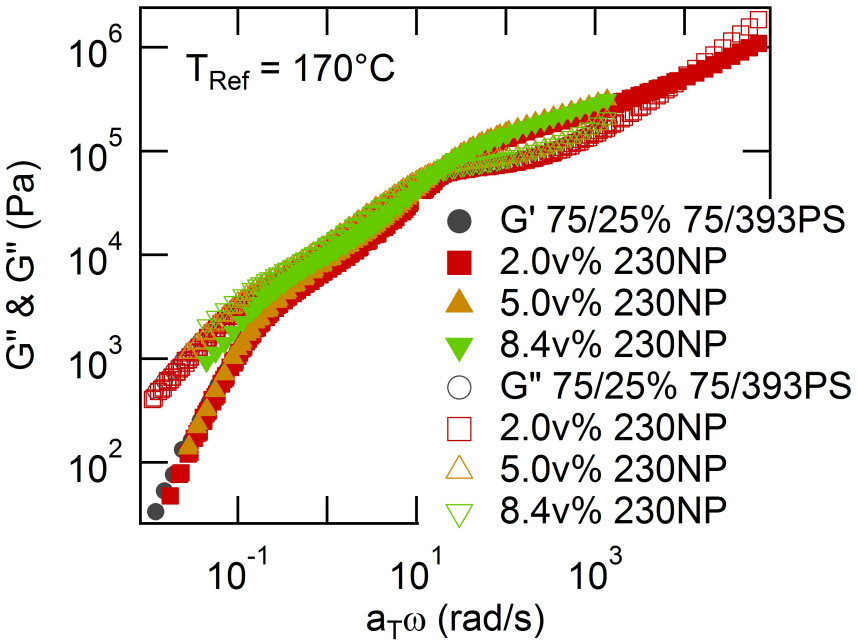

(b) Storage & Loss Moduli

Figure A.4: Master curves of 75/25% 75/393 kD polystyrene with three volume fractions of 140NP cross linked polystyrene nanoparticles. Results shifted to a reference temperature of 170 °C.

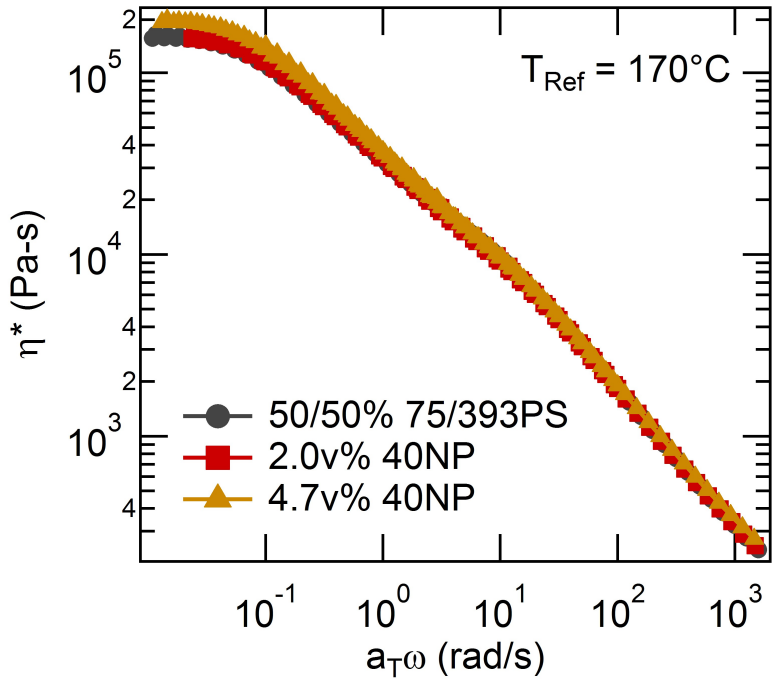

(a) Complex Viscosity

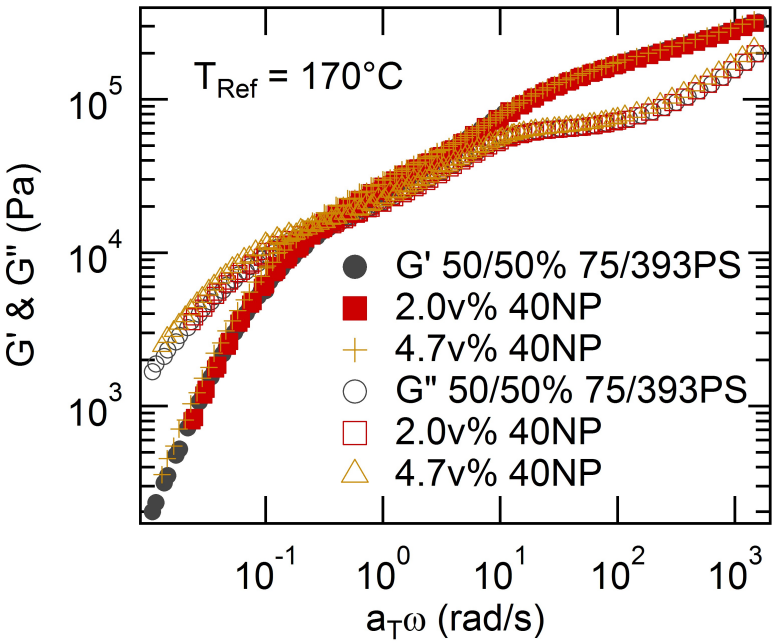

(b) Storage & Loss Moduli

Figure A.5: Master curves of 50/50% 75/393 kD polystyrene with two volume fractions of 25NP cross linked polystyrene nanoparticles. Results shifted to a reference temperature of 170 °C.

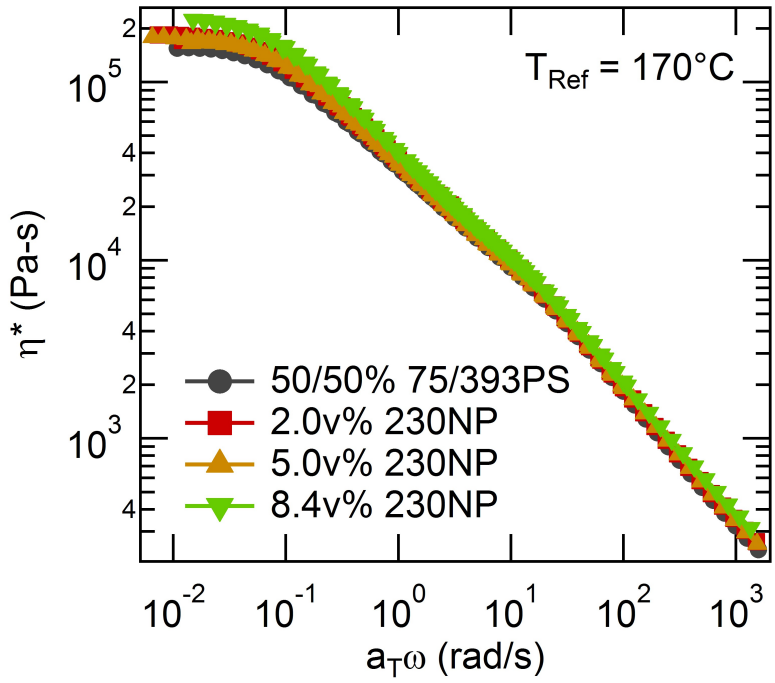

(a) Complex Viscosity

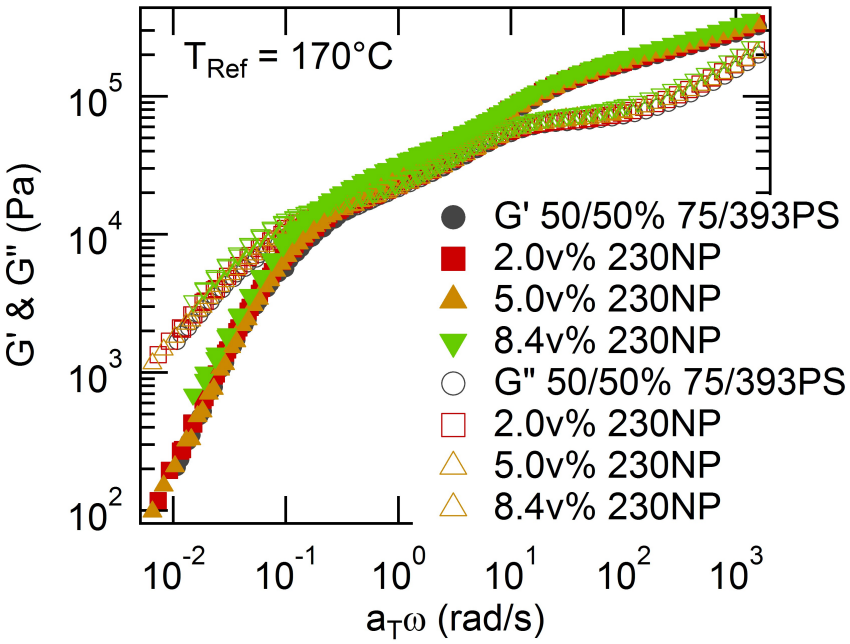

(b) Storage & Loss Moduli

Figure A.6: Master curves of 50/50% 75/393 kD polystyrene with three volume fractions of 140NP cross linked polystyrene nanoparticles. Results shifted to a reference temperature of 170 °C.

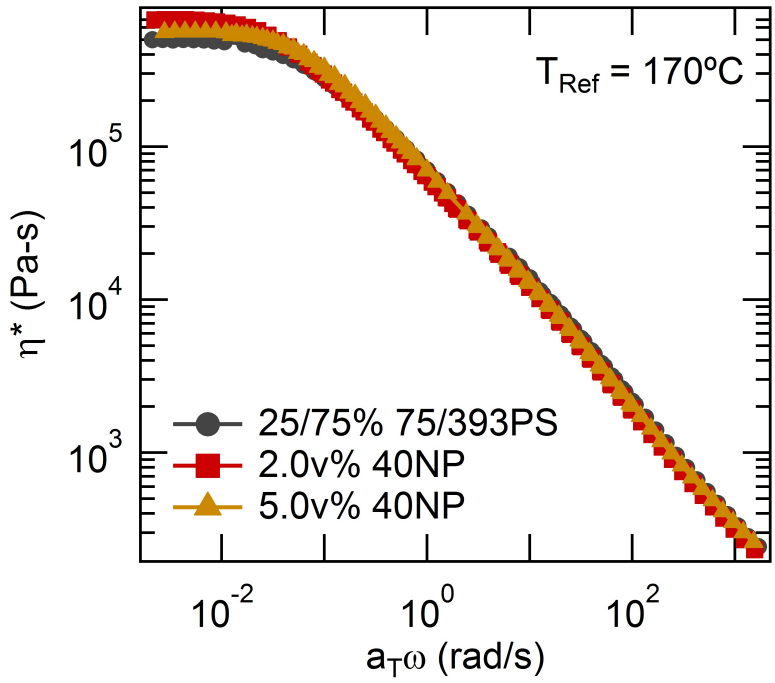

(a) Complex Viscosity

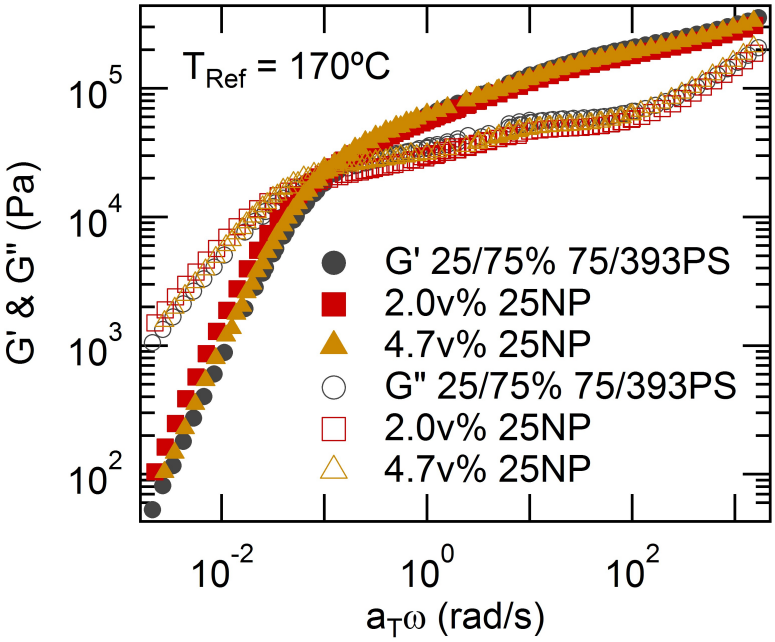

(b) Storage & Loss Moduli

Figure A.7: Master curves of 25/75% 75/393 kD polystyrene with two volume fractions of 25NP cross linked polystyrene nanoparticles. Results shifted to a reference temperature of 170 °C.

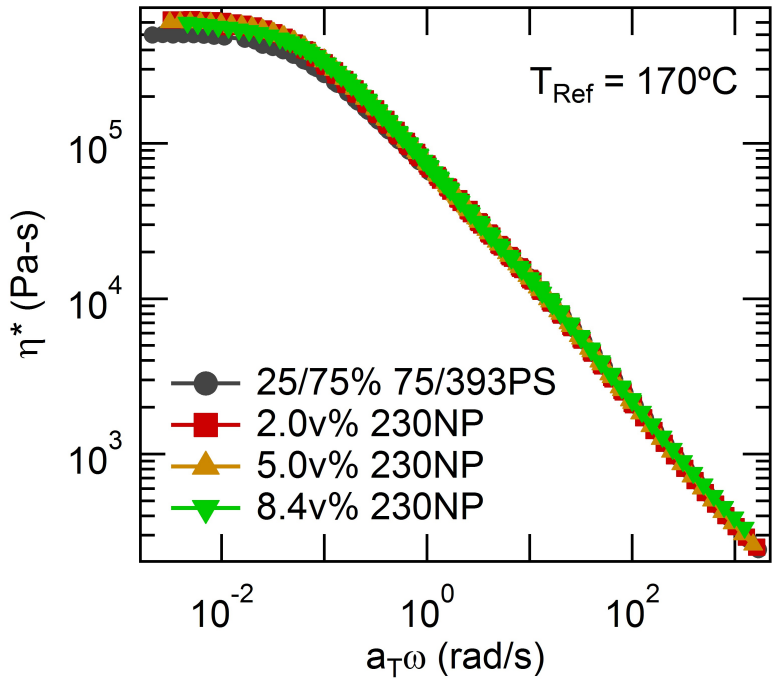

(a) Complex Viscosity

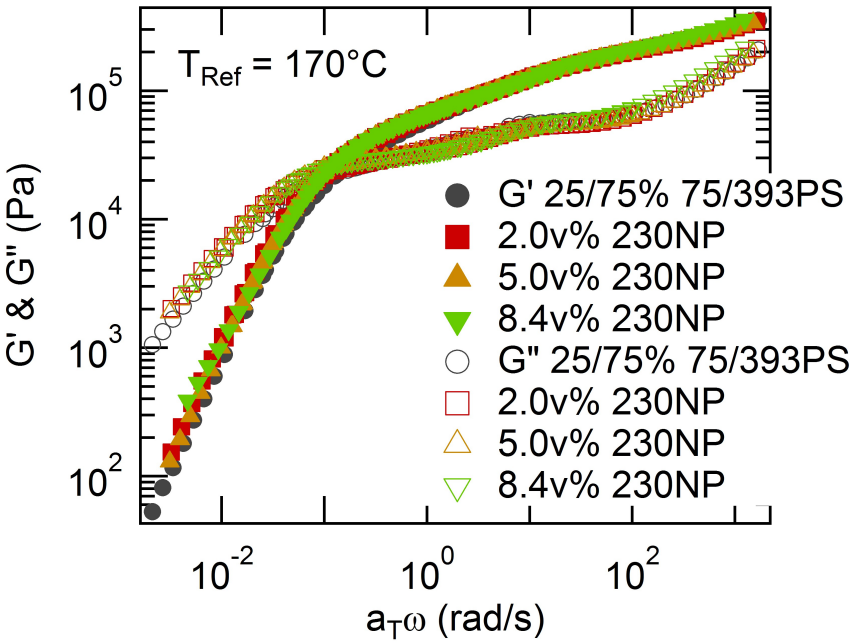

(b) Storage & Loss Moduli

Figure A.8: Master curves of 25/75% 75/393 kD polystyrene with three volume fractions of 140NP cross linked polystyrene nanoparticles. Results shifted to a reference temperature of 170 °C.

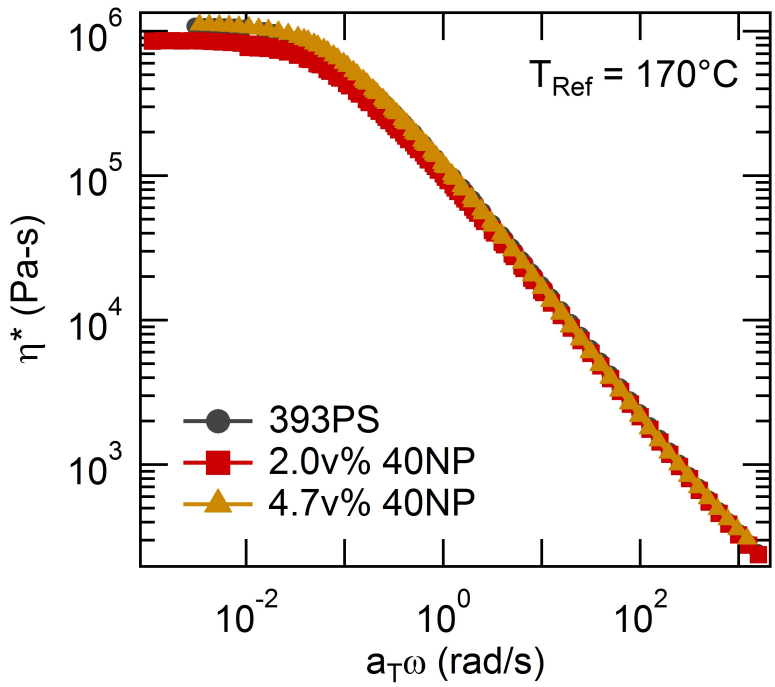

(a) Complex Viscosity

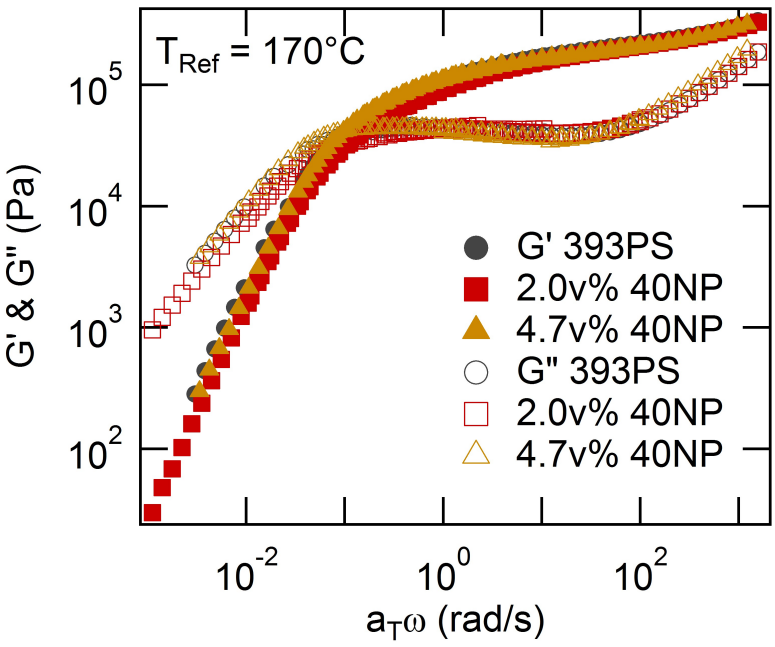

(b) Storage & Loss Moduli

Figure A.9: Master curves of 393 kD polystyrene with two volume fractions of 25NP cross linked polystyrene nanoparticles. Results shifted to a reference temperature of 170 °C.

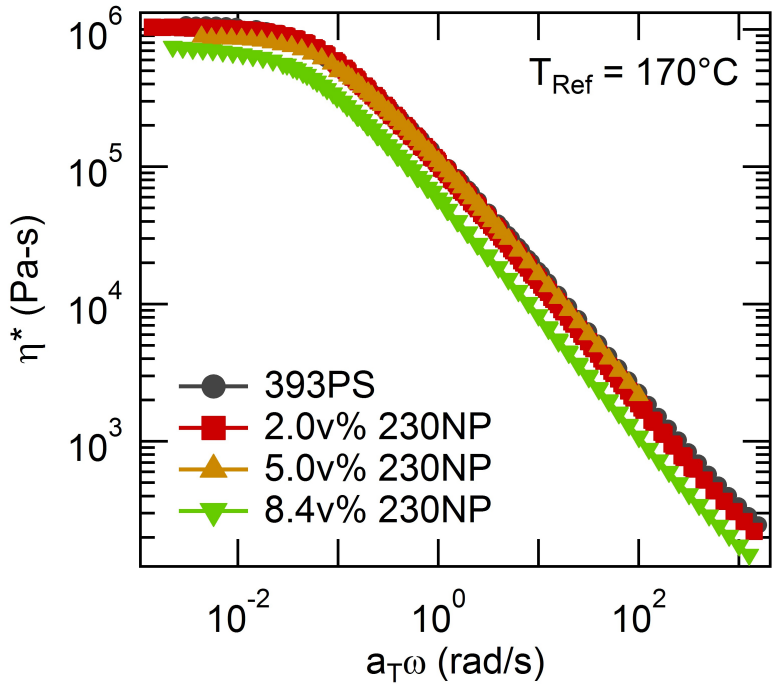

(a) Complex Viscosity

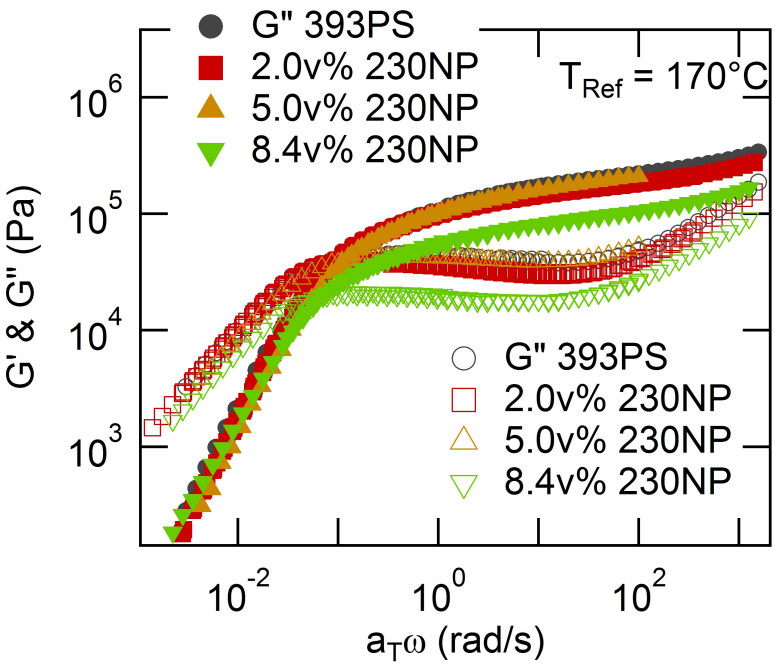

(b) Storage & Loss Moduli

Figure A.10: Master curves of 393 kD polystyrene with three volume fractions of 140NP cross linked polystyrene nanoparticles. Results shifted to a reference temperature of 170 °C.

Appendix B

Master Curves of Poly(styrene-co-acrylonitrile) With Cross Linked Poly(styrene-co-acrylonitrile) Nanoparticles

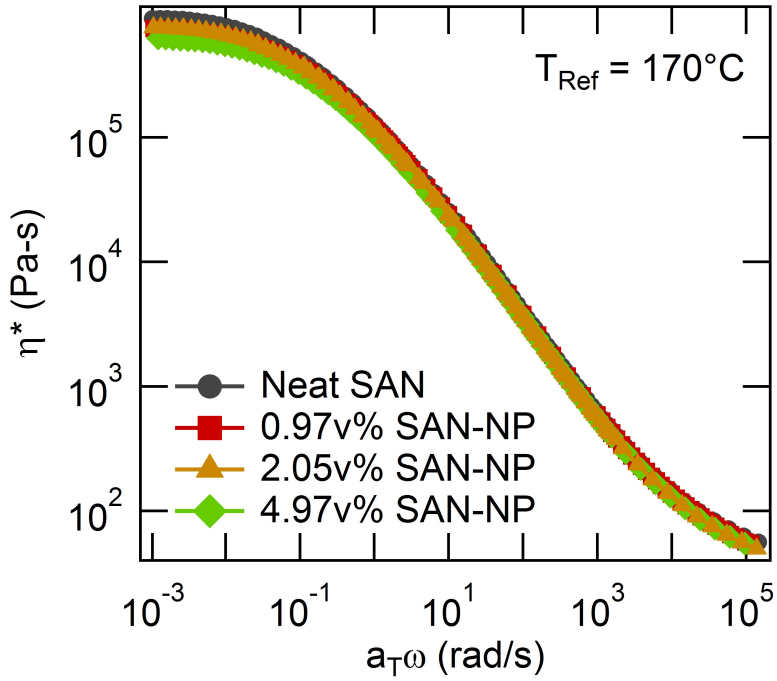

(a) Complex Viscosity

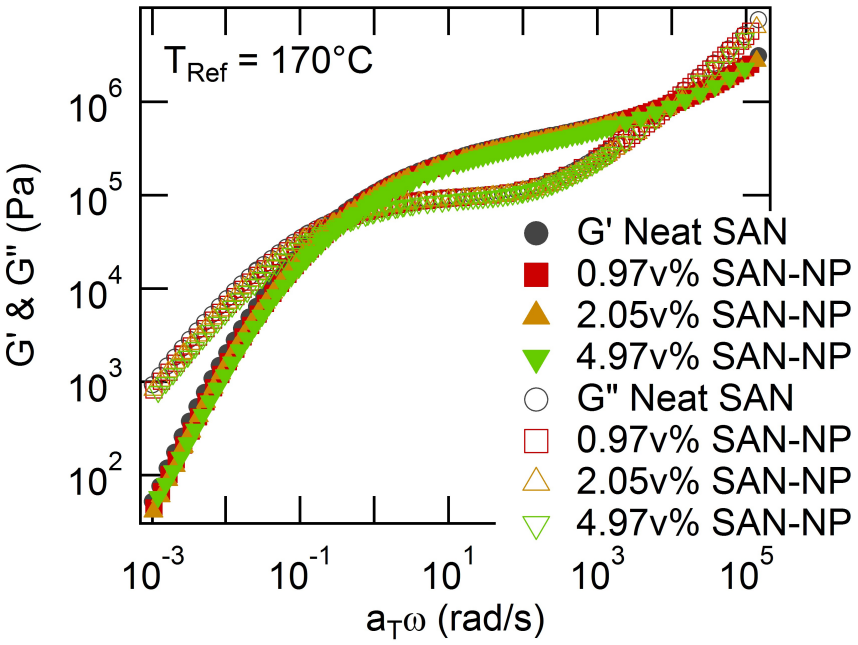

(b) Storage & Loss Moduli

Figure B.1: Master curves of poly(styrene-co-acrylonitrile) (SAN) with cross linked poly(styrene-co-acrylonitrile) nanoparticles (SAN-NP). Results shifted to a reference temperature of 170 °C.

Appendix C

Master Curves of Poly(methyl methacrylate) C_{60} and Fe_3O_4 Nanocomposites

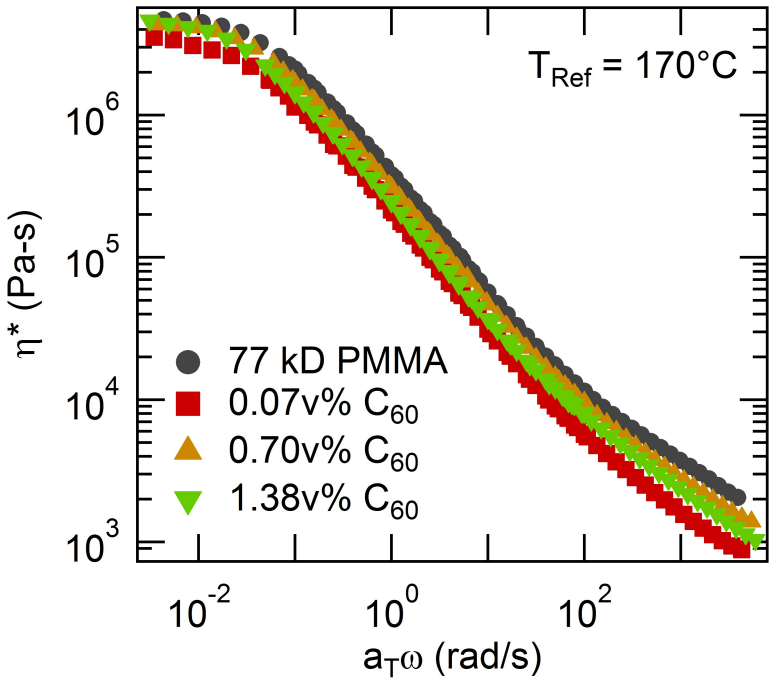

(a) Complex Viscosity

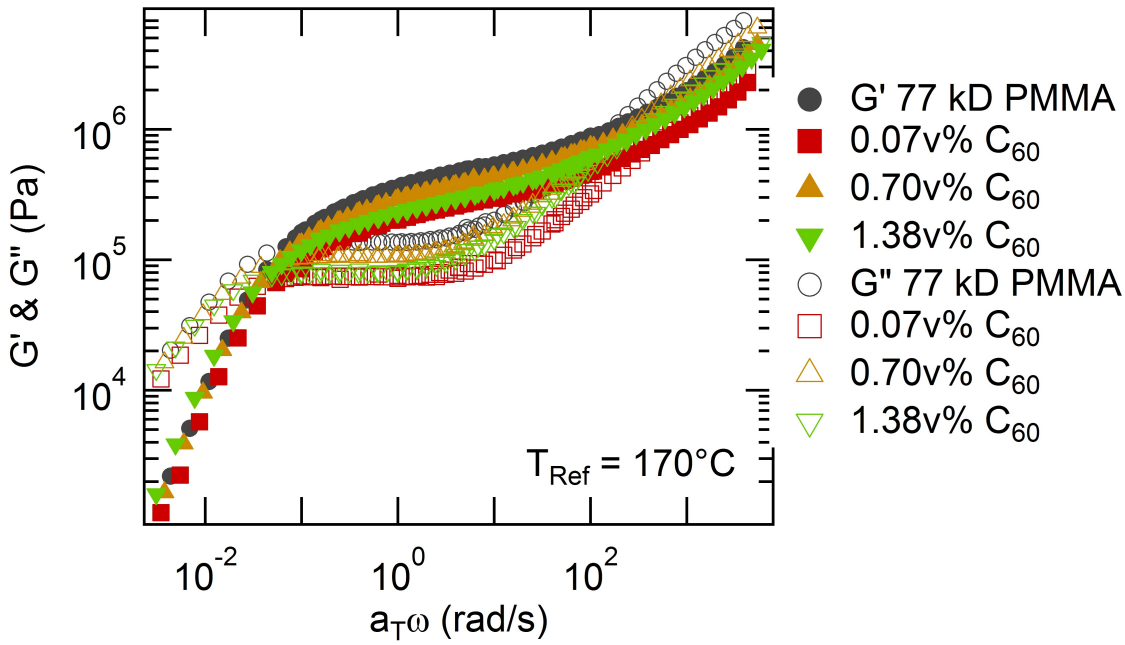

(b) Storage & Loss Moduli

Figure C.1: Master curves of 77 kD poly(methyl methacrylate) with three volume fractions of C_{60}. Results shifted to a reference temperature of 170 °C.

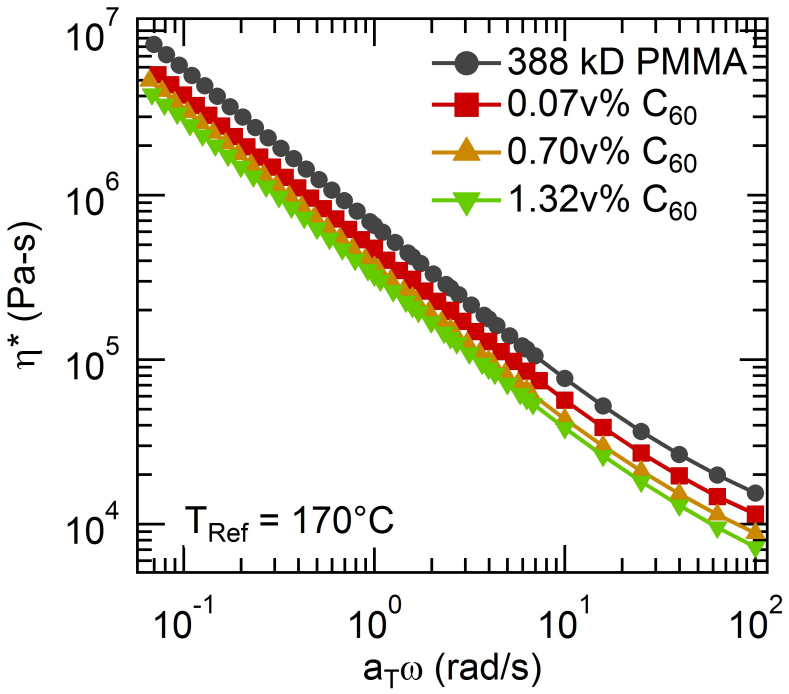

(a) Complex Viscosity

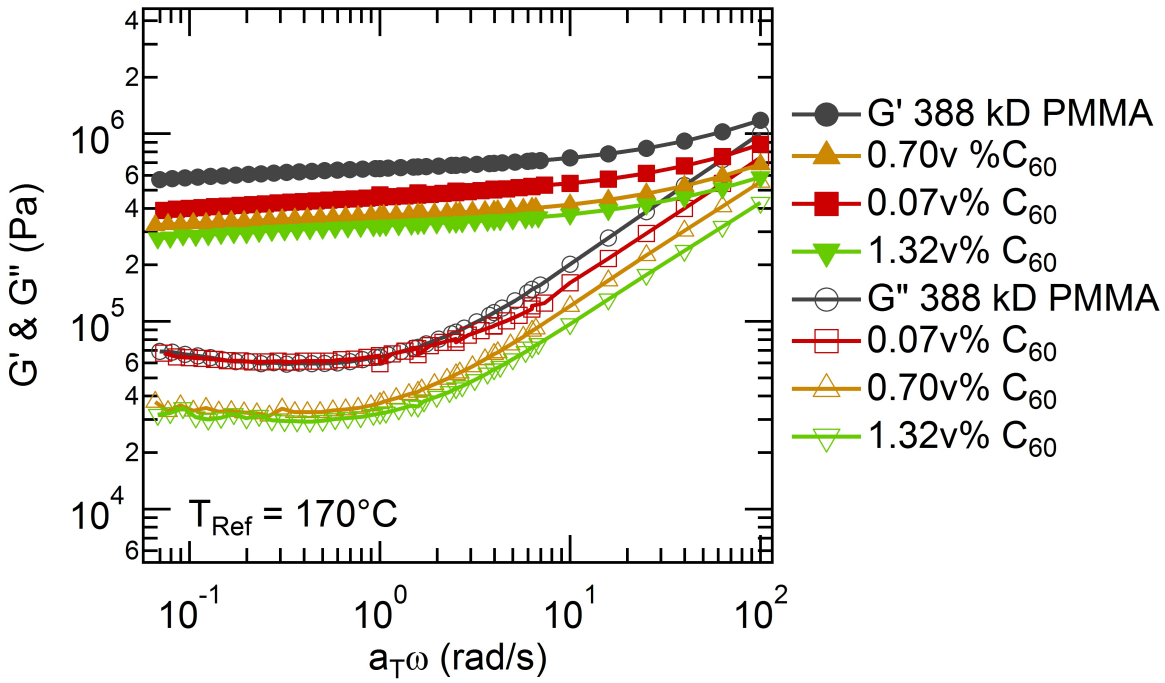

(b) Storage & Loss Moduli

Figure C.2: Master curves of 388 kD poly(methyl methacrylate) with three volume fractions of C_{60}. Results shifted to a reference temperature of 170 °C.

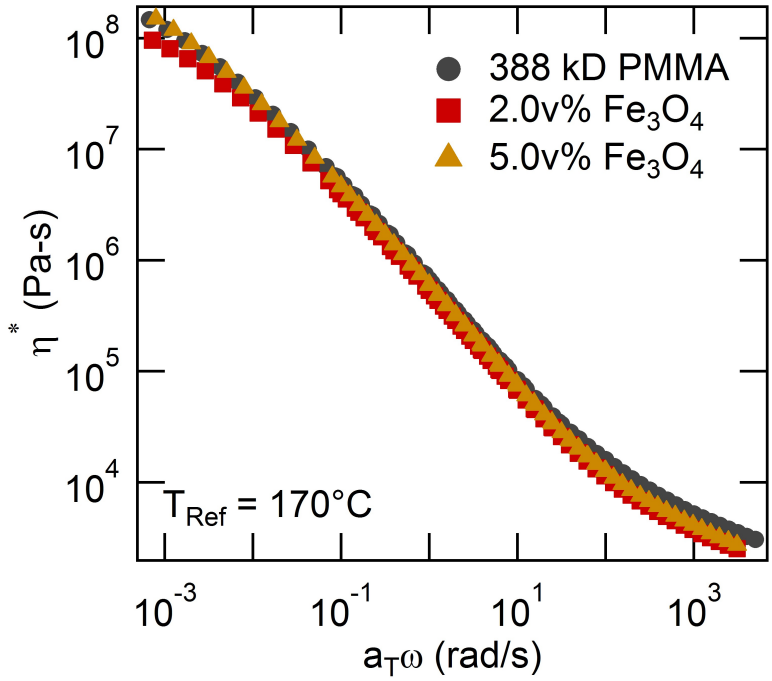

(a) Complex Viscosity

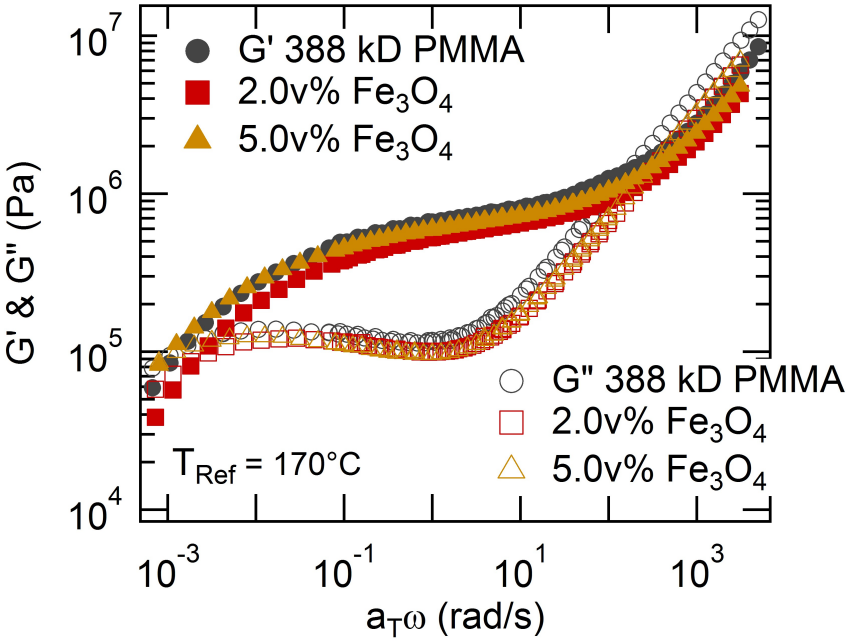

(b) Storage & Loss Moduli

Figure C.3: Master curves of 388 kD with two volume fractions of Fe_3O_4. Results shifted to a reference temperature of 170 °C.

Appendix D

Rheology of Poly(3-hexylthiophene)

Poly(3-hexylthiophene) is the currently the work horse polymer of organic solar cell researchers. The rheological properties were briefly studied in an attempt to provide additional information, such as melt viscosity to other group members. Sepiloid P-100 P3HT (BASF & Reike Metals) was pressed under vacuum into 8-mm rheological disk at 235 °C for 15 minutes.

For oscillatory shear temperature ramps the disks were loaded on to an ARES-G2 at room temperature and a 3 °C/minute ramp was run from 30-250 °C and back down with a strain of 0.1%, frequency of 10 rad/s. Axial force was set to 0.03 ± 0.01 N with force tracking (Axial Force > Dynamic Force at 1.0%) with a minum force of 1.0 N to manintain contact. To compensate for the decrease in visocsity though the melting temperature automatic strain adjustment was employed to keep the oscillartory torque between 30 and 10000 $\mu N - m$ bounded to a minimum strain of 0.1% and 8.0%. All in a nitrogen atmosphere.

For oscillatory shear time sweeps, strain sweeps, and frequency sweeps the disks were loaded at 235 °C after allowing the instrument to thermally equilibrate for 1 hour. Time

sweeps were run at 10% strain and 10 rad/s.

From the temperature ramp, Figure D.1, we determine the T_g for this type of P3HT to be 35.1 °C and the crystalline melting temperature to be between 197.9 °C and 227.4 °C. A time sweep was run to determine thermal stability in nitrogen above the melting temperature.

In Figure D.2 we show a composite time sweep covering 3.5 hours with intermittent frequency and strain sweeps. The P3HT starts off as a viscous liquid that steadily increases in viscosity until approximately 20 minutes (Figure D.2) where we see a G' G" crossover. From the strain sweeps (Figure D.3 taken before (D.3(a)) and after (D.3(b)) the cross over we can again see the change from liquid like to solid like. The set of intermittent frequency sweeps (Figure D.4), taken about ever 30 minutes remain fairly constant. In the final strain sweep, shown in Figure D.5(b) a non-linear region appears at high strain.

There are two likely reasons for the increase in stiffness of the material over the duration of the time sweep. The P3HT known for is instability in air could still be degrading via crosslinking, however, the used disks readily re-disperse in toluene ruling out permanent network formation. However P3HT can readily crystallize and it seems reasonable to suggest the extra thermal mobility is allowing the polymer to for a crystalline network. If this is the case it would begin excluding nanoparticles at that temperature after 20 minutes. This would effect processing conditions if nanoparticle dispersion is desired. Though the ideal organic solar cell is a interdigitated network so using the high temperature crystallization to drive a phase separation could be quite beneficial.

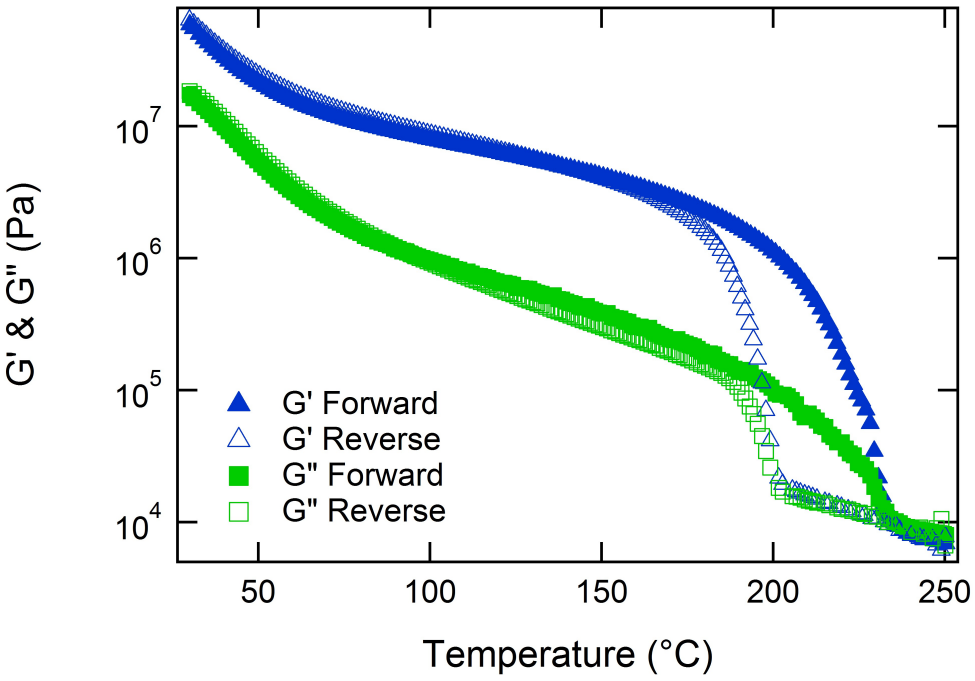

(a) Storage and Loss Modulus

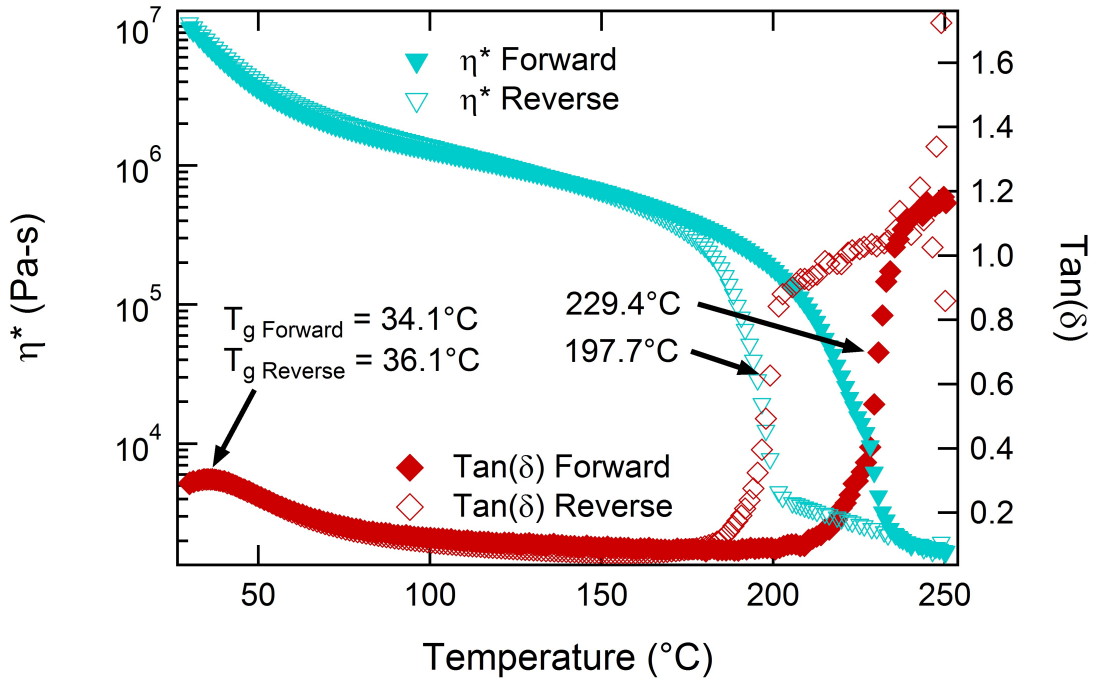

(b) Complex Viscosity and Loss Tangent

Figure D.1: Material properties of P3HT for a temperature ramp from 30-250 ° (forward cycle) and from 250-30 °C (reverse cycle) each at 3 °C/minute. A peak in the loss tangent (T_g) is noted as well as approximate crystalline melting temperatures.

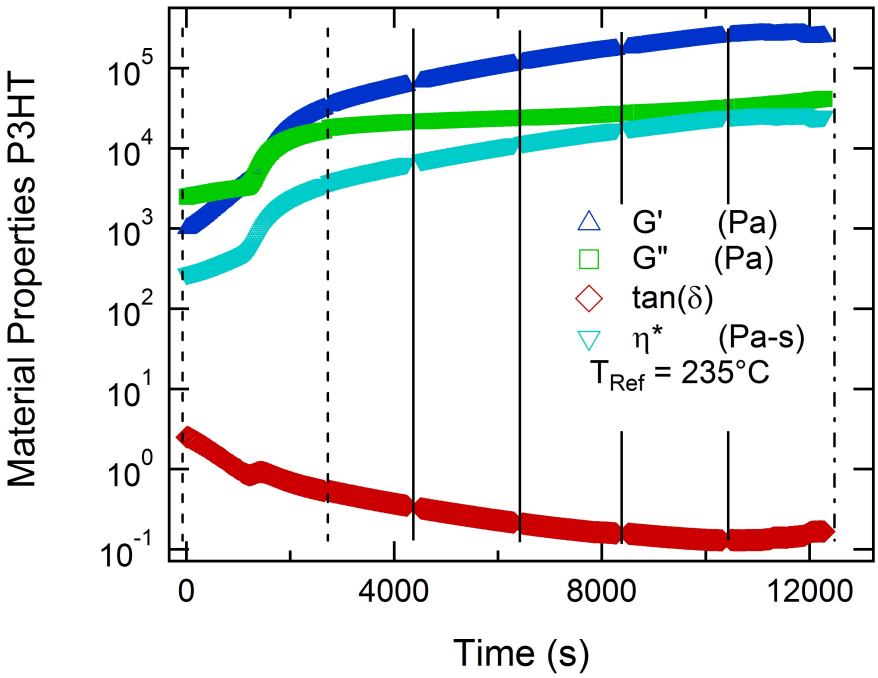

Figure D.2: Material properties of P3HT as a function of time at 235 °C. Note the sudden increase in stiffness after 1200 seconds. The vertical lines indicate times when strain sweeps (dashed lines) Figure D.3 or frequency sweeps (solid lines) Figure D.4 were conducted. The dot-dash line indicates a final frequency sweep followed by a final strain sweep, Figure D.5. All subsequent figures share this legend.

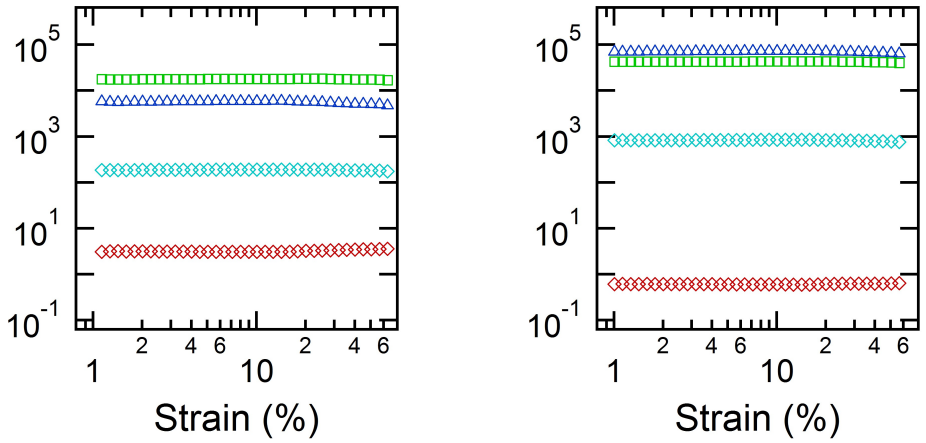

(a) Initial Strain Sweep (b) Strain Sweep at 1200s

Figure D.3: Two strain sweeps of P3HT before and after increase in stiffness at 235 °C. Legend is the same as Figure D.2

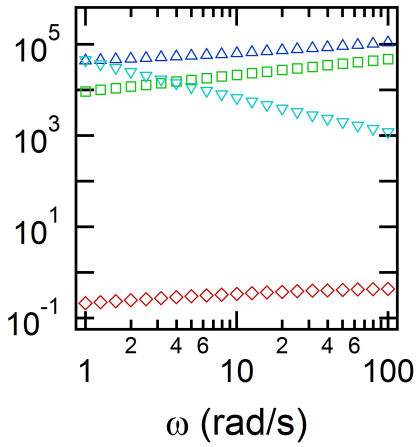

(a) Frequency Sweep at 4300s

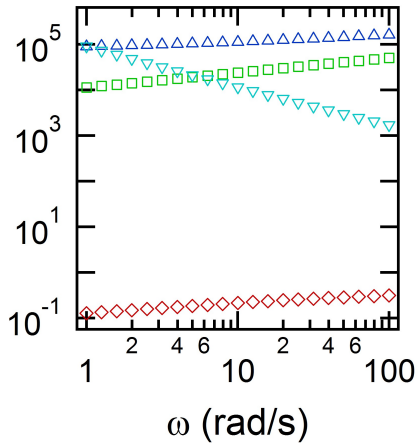

(b) Frequency Sweep at 6300s

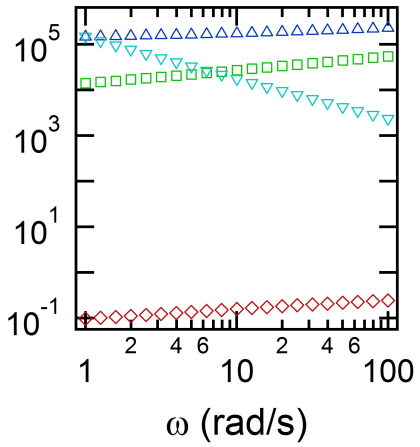

(c) Frequency Sweep at 8300s

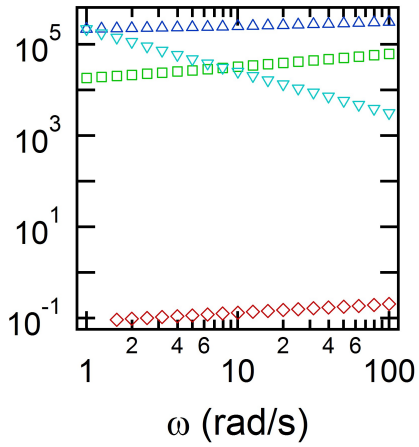

(d) Frequency Sweep at 10300s

Figure D.4: Four frequency sweeps of P3HT following increase in stiffness at 235 °C. Legend is the same as Figure D.2

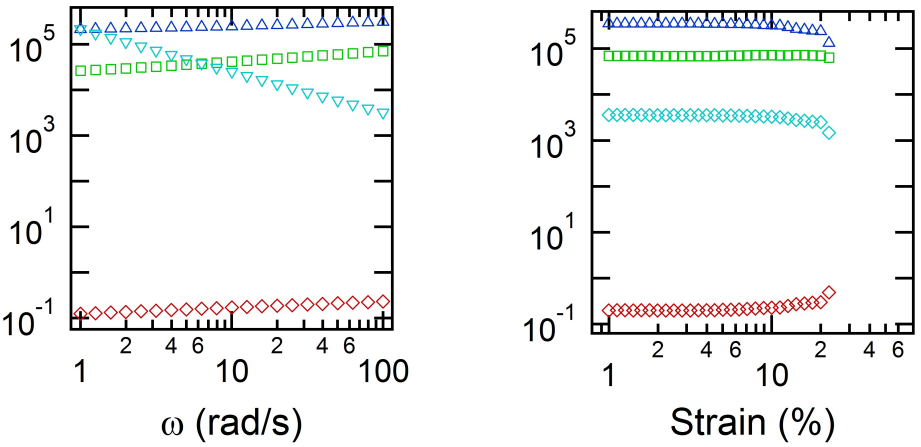

(a) Final Frequency Sweep (b) Final Strain Sweep

Figure D.5: Final frequency sweep and strain sweep. The sample begins to show non linear behavior in at high strain after several hours at 235 °C. Legend is the same as Figure D.2

BIBLIOGRAPHY

[1] Tuteja, A., Mackay, M. E., Hawker, C. J., Horn, B. V. & Ho, D. L. Molecular architecture and rheological characterization of novel intramolecularly crosslinked polystyrene nanoparticles. *Journal of Polymer Science Part B: Polymer Physics* **44**, 1930–1947 (2006).

[2] Harth, E. M. *et al.* A facile approach to architecturally defined nanoparticles via intramolecular chain collapse. *Journal of the American Chemical Society* **124**, 8653–8660 (2002).

[3] Liu, C. Y., He, J. S., van Ruymbeke, E., Keunings, R. & Bailly, C. Evaluation of different methods for the determination of the plateau modulus and the entanglement molecular weight. *Polymer* **47**, 4461–4479 (2005).

[4] A. Einstein, A. The theory of the brownian motion. *Annalen Der Physik* **19**, 371–381 (1906).

[5] Batchelor, G. K. The effect of brownian motion on the bulk stress in a suspension of spherical particles. *Journal of Fluid Mechanics* **83**, 97–117 (1977).

[6] Yasuda, K., Armstrong, R. C. & Cohen, R. E. Shear-flow properties of concentrated-solutions of linear and star branched polystyrenes. *Rheologica Acta* **20**, 163–178 (1981).

[7] Dealy, J. M. & Larson, R. G. *Structure and Rheology of Molten Polymers* (Hanser, 2006).

[8] Cox, W. P. & Merz, E. H. Correlation of dynamic and steady flow viscosities. *Journal of Polymer Science* **28**, 619–622 (1958).

[9] Cheng, P. Y. & Schachman, H. K. Studies on the validity of the einstein viscosity law and stokes law of sedimentation. *Journal of Polymer Science* **16**, 19–30 (1955).

[10] Metzner, A. B. Rheology of suspensions in polymeric liquids. *Journal of Rheology* **29**, 739–775 (1985).

[11] Russel, W. B., Saville, D. A. & Schowalter, W. R. *Colloidal Dispersions* (Cambridge University Press, 1992).

[12] Vanderwerff, J. C. & Dekruif, C. G. Hard-sphere colloidal dispersions - the scaling of rheological properties with particle-size, volume fraction, and shear rate. *Journal of Rheology* **33**, 421–454 (1989).

[13] Hare, J. P., Kroto, H. W. & Taylor, R. Preparation and uv visible spectra of fullerenes c60 and c70. *Chemical Physics Letters* **177**, 394–398 (1991).

[14] Asokan, S. *et al.* The use of heat transfer fluids in the synthesis of high-quality cdse quantum dots, core/shell quantum dots, and quantum rods. *Nanotechnology* **16**, 2000–2011 (2005).

[15] Huang, X. *et al.* Polyethylene/aluminum nanocomposites: Improvement of dielectric strength by nanoparticle surface modification. *Journal of Applied Polymer Science* **113**, 3577–3584 (2009).

[16] Kalima, V. *et al.* Uv-curable zns/polymer nanocomposite for replication of micron and submicron features. *Optical Materials* **31**, 1540–1546 (2009).

[17] Shah, M. S. A. S., Nag, M., Kalagara, T., Singh, S. & Manorama, S. V. Silver on $PEG-PU-TiO_2$ polymer nanocomposite films: An excellent system for antibacterial applications. *Chemistry Materials* **20**, 2455–2460 (2008).

[18] Roberts, C., Cosgrove, T., Schmidt, R. G. & Gordon, G. V. Diffusion of poly(dimethyl siloxane) mixtures with silicate nanoparticle. *Macromolecules* **34**, 538–543 (2001).

[19] Mackay, M. E. *et al.* Nanoscale effects leading to non-einstein-like decrease in viscosity. *Nature Materials* **2**, 762–766 (2003).

[20] Mackay, M. E. *et al.* General strategies for nanoparticle dispersion. *Science* **311**, 1740–1743 (2006).

[21] Tuteja, A., Mackay, M. E., Narayanan, S., Asokan, S. & Wong, M. S. Breakdown of the continuum stokes-einstein relation for nanoparticle diffusion. *Nano Letters* **7**, 1276–1281 (2007).

[22] Yuan, Q. W., Kloczkowski, A., Mark, J. E. & Sharaf, M. A. Simulations on the reinforcement of poly(dimethylsiloxane) elastomers by randomly distributed filler particles. *Journal of Polymer Science Part B - Polymer Physics* **34** (1996).

[23] Nakatani, A. I., Chen, W., Schmidt, R. G., Gordon, G. V. & Han, C. C. Chain dimensions in polysilicate-filled poly(dimethyl siloxane). *Polymer* **42**, 3713–3722 (2001).

[24] Nowicki, W. Structure and entropy of a long polymer chain in the presence of nanoparticles. *Macromolecules* **35**, 1424–1436 (2002).

[25] Starr, F. W., Schroder, T. B. & Glotzer, S. C. Molecular dynamics simulation of a polymer melt with a nanoscopic particle. *Macromolecules* **35**, 4481–4492 (2002).

[26] Sharaf, M. A. & Mark, J. E. Monte carlo simulations on the effects of nanoparticles on chain deformations and reinforcement in amorphous polyethylene networks. *Polymer* **45**, 3943–3952 (2004).

[27] Tuteja, A., Duxbury, P. M. & Mackay, M. E. Polymer chain swelling induced by dispersed nanoparticles. *Physical Review Letters* **100** (2008).

[28] Frischknecht, A. L., McGarrity, E. S. & Mackay, M. E. Expanded chain dimensions in polymer melts with nanoparticle fillers. *Journal of Chemical Physics* **132** (2010).

[29] Tuteja, A., Mackay, M. E., Hawker, C. J. & Horn, B. V. Effect of ideal, organic nanoparticles on the flow properties of linear polymers: Non-einstein-like behavior. *Macromolecules* **38**, 8000–8011 (2005).

[30] Ferry, J. D. *Viscoelastic Properties of Polymers* (John Wiley & Sons, New York, 1980), 3rd edn.

[31] Lauter-Pasyuk, V. *et al.* Neutron reflectivity studies of composite nanoparticle copolymer thin films. *Physica B* **248**, 243–245 (1998).

[32] Thompson, R. B., Ginzburg, V. V., Matsen, M. W. & Balazs, A. C. Predicting the mesophases of copolymer-nanoparticle composites. *Science* **292**, 2469–2472 (2001).

[33] Ginzburg, V. V. Influence of nanoparticles on miscibility of polymer blends. a simple theory. *Macromolecules* **38**, 2362–2367 (2005).

[34] Cotton, J. P. *et al.* Conformation of polymer chain in the bulk. *Macromolecules* **7**, 863–872 (1974).

[35] Degennes, P. G. Reptation of a polymer chain in presence of fixed obstacles. *Journal of Chemical Physics* **55**, 572–579 (1971).

[36] Degennes, P. G. Dynamics of entangled polymer-solutions .1. rouse model. *Macromolecules* **9**, 587–593 (1976).

[37] Klein, J. Evidence for reptation in an entangled polymer melt. *Nature* **271**, 143–145 (1978).

[38] Doi, M. & Edwards, S. F. *The Theory of Polymer Dynamics* (Oxford, New York, NY, 1986).

[39] Edwards, S. F. Statistical mechanics with topological constraints: I. *Proceedings of the Physical Society* **91**, 513–& (1967).

[40] Edwards, S. F. Statistical mechanics of polymerized material. *Proceedings of the Physical Society of London* **92**, 9–& (1967).

[41] Fox, T. G. & Flory, P. J. Viscosity-molecular weight and viscosity-temperature relationships for polystyrene and polyisobutylene. *Journal of the American Chemical Society* **70**, 2384–2395 (1948).

[42] Fox, T. G. & Flory, P. J. The glass temperature and related properties of polystyrene - influence of molecular weight. *Journal of Polymer Science* **14**, 315–319 (1954).

[43] Berry, C. G. & Fox, T. G. The viscosity of polymers and their concentrated solutions. *Advances in Polymer Science* **5**, 261–357 (1968).

[44] Einstein, A. On the movement of small particles suspended in stationary liquids required by the molecular-kinetic theory of heat. *Annalen der Physik* **7**, 549–560 (1905).

[45] Smoluchowski, M. The kinetic theory of brownian motion under molecular suspension. *Annalen der Physik* **21**, 756–780 (1906).

[46] Farrington, P. J. *Polymer structure, dynamics and viscoelasticity.* Ph.D. thesis, University of Queensland, Brisbane, Brisbane, Australia (1996).

[47] Liu, C. Y., He, J. S., van Ruymbeke, E., Keunings, R. & Bailly, C. Evaluation of different methods for the determination of the plateau modulus and the entanglement molecular weight. *Polymer* **47**, 4461–4479 (2006).

[48] Tsenoglou, C. Molecular-weight polydispersity effects on the viscoelasticity of entangled linear-polymers. *Macromolecules* **24**, 1762–1767 (1991).

[49] Hooper, J. B. & Schweizer, K. S. Contact aggregation, bridging, and steric stabilization in dense polymer-particle mixtures. *Macromolecules* **38**, 8858–8869 (2005).

[50] Marrucci, G. Free-energy constitutive equation for polymer-solutions from dumbbell model. *Transactions of the Society of Rheology* **16**, 321–& (1972).

[51] Park, S. Y., Barrett, C. J., Rubner, M. F. & Mayes, A. M. Anomalous adsorption of polyelectrolyte layers. *Macromolecules* **34**, 3384–3388 (2001).

[52] Lan, T., Kaviratna, P. D. & Pinnavaia, T. J. On the nature of polyimide clay hybrid composites. *Chemistry of Materials* **6**, 573–575 (1994).

[53] Croce, F. ., Appetecchi, G. B., Persi, L. & Scrosati, B. Nanocomposite polymer electrolytes for lithium batteries. *Nature* **394**, 456–458 (1998).

[54] Beecroft, L. L. & Ober, C. K. Nanocomposite materials for optical applications. *Chemistry of Materials* **9**, 1302–1317 (1997).

[55] Tuteja, A., Duxbury, P. M. & Mackay, M. E. Multifunctional nanocomposites with reduced viscosity. *Macromolecules* **40**, 9427–9434 (2007).

[56] Yin, Y. & Alivisatos, A. Colloidal nanocrystal synthesis and the organic-inorganic interface. *Nature* **437**, 664–670 (2005).

[57] Cushing, B. L., Kolesnichenko, V. L. & O'Connor, C. J. Recent advances in the liquid-phase syntheses of inorganic nanoparticles. *Chemical Reviews* **104**, 3893–3946 (2004).

[58] Wang, X., Zhuang, J., Peng, Q. & Li, Y. D. A general strategy for nanocrystal synthesis. *Nature* **437**, 121–124 (2005).

[59] Tartaj, P., Morales, M. D., Veintemillas-Verdaguer, S., Gonzalez-Carreno, T. & Serna, C. J. The preparation of magnetic nanoparticles for applications in biomedicine. *Journal of Physics D - Applied Physics* **36**, R182–R197 (2003).

[60] Khomutov, G. B. & Koksharov, Y. A. Effects of organic ligands, electrostatic and magnetic interactions in formation ofcolloidal and interfacial inorganic nanostructures. *Advances in Colloid and Interface Science* **122**, 119–147 (2006).

[61] Yaklin, M. A., Duxbury, P. M. & Mackay, M. E. Control of nanoparticle dispersion in thin polymer films. *Soft Matter* **4**, 2441–2447 (2008).

[62] McGarrity, E. S., Frischknecht, A. L. & Mackay, M. E. Phase behavior of polymer/nanoparticle blends near a substrate. *Journal of Chemical Physics* **128** (2008).

[63] Krishnan, R. S. *et al.* Self-assembled multilayers of nanocomponents. *Nano Letters* **7**, 484–489 (2007).

[64] O'Brien, V. T. & Mackay, M. E. Stress components and shear thickening of concentrated hard sphere suspensions. *Langmuir* **16**, 7931–7938 (2000).

[65] Zimm, B. H. The scattering of light and the radial distrubtion function of high polymer solutions. *Journal of Chemical Physics* **16**, 1093–1099 (1948).

[66] Zimm, B. H. Apparatus and methods for measurements and interpretation of the angular variation of light scattering; prelimiary reults on polystyrene soutions. *Journal of Chemical Physics* **16**, 1099–1116 (1948).

[67] Rubinstein, M. & Colby, H. C. *Polymer Physics* (Oxford University Press, New York, NY, 2003).

[68] Kline, S. R. Reduction and analysis of sans and usans data using igor pro. *Journal of Applied Crystallography* **39**, 895–900 (2006).

[69] Pethrick, R. A. & Dawkins, J. V. (eds.) *Small-Angle Neutron Scattering* (John Wiley & Sons, Chichester, England, 1999).

[70] Higgins, J. S. & Benoit, H. C. *Polymers And Neutron Scattering* (Clarendon Press, 1996), 2 edn.

[71] Mackay, M. E. Dendrimers, nanodevices to create unique phenomena. *Comptes Rendus Chimie* **6**, 747–754 (2003).

[72] Jelenic, J., Kirste, R. G., Oberthur, R. C., Schmittstrecker, S. & Schmitt, B. J. Investigation of exothermic polymer blends by neutron-scattering. *Makromolekulare Chemie-Macromolecular Chemistry and Physics* **185**, 129–156 (1984).

[73] Bates, F. S. & Wignall, G. D. Isotope-induced quantum-phase transitions in the liquid-state. *Physical Review Letters* **57**, 1429–1432 (1986).

[74] Bates, F. S. & Wignall, G. D. Nonideal mixing in binary blends of perdeuterated and protonated polystyrenes. *Macromolecules* **19**, 932–934 (1986).

[75] Zhogova, K. B., Davydov, I. A., Punin, V. T., Troitskii, B. B. & Domvachiev, G. A. Investigation of fullerene c-60 effect on properties of polymethylmethacrylate exposed to ionizing radiation. *European Polymer Journal* **41**, 1260–1264 (2005).

[76] Song, P., Zhu, Y., Tong, L. F. & Fang, Z. P. C-60 reduces the flammability of polypropylene nanocomposites by in situ forming a gelled-ball network. *Nanotechnology* **19** (2008).

[77] Waller, J. H. *et al.* C-60 fullerene inclusions in low-molecular-weight polystyrene-poly(dimethylsiloxane) diblock copolymers. *Polymer* **50**, 4199–4204 (2009).

[78] Barnes, K. A. *et al.* Suppression of dewetting in nanoparticle-filled polymer films. *Macromolecules* **33**, 4177–4185 (2000).

[79] Holmes, M. A., Mackay, M. E. & Giunta, R. K. Nanoparticles for dewetting suppression of thin polymer films used in chemical sensors. *Journal of Nanoparticle Research* **9**, 753–763 (2007).

[80] Sariciftci, N. S., Smilowitz, L., Heeger, A. J. & Wudl, F. Photoinduced electron-transfer from a conducting polymer to buckminsterfullerene. *Science* **258**, 1474–1476 (1992).

[81] Yu, G., Gao, J., Hummelen, J. C., Wudl, F. & Heeger, A. J. Polymer photovoltaic cells - enhanced efficiencies via a network of internal donor-acceptor heterojunctions. *Science* **270**, 1789–1791 (1995).

[82] Kim, Y. *et al.* Effect of electron-transport polymer addition to polymer/fullerene blend solar cells. *Synthetic Metals* **152**, 105–108 (2005).

[83] Kropka, J. M., Putz, K. W., Pryamitsyn, V., Ganesan, V. & Green, P. F. Origin of dynamical properties in pmma-c-60 nanocomposites. *Macromolecules* **40**, 5424–5432 (2007).

[84] Sanz, A., Ruppel, M., Douglas, J. F. & Cabral, J. T. Plasticization effect of c-60 on the fast dynamics of polystyrene and related polymers: An incoherent neutron scattering study. *Journal of Physics-Condensed Matter* **20** (2008).

[85] Bezmel'nitsyn, V. N., Eletskii, A. V. & Okun', M. V. Fullerenes in solutions. *Uspekhi Fizicheskikh Nauk* **168**, 1195–1220 (1998).

[86] Weng, D. *et al.* The influence of buckminsterfullerenes and their derivatives on polymer properties. *European Polymer Journal* **35**, 867–878 (1999).

[87] Starr, F. W., Schroder, T. B. & Glotzer, S. C. Effects of a nanoscopic filler on the structure and dynamics of a simulated polymer melt and the relationship to ultrathin films. *Physical Review E* **64** (2001).

[88] Varnik, F., Baschnagel, J. & Binder, K. Reduction of the glass transition temperature in polymer films: A molecular-dynamics study. *Physical Review E* **65** (2002).

[89] Pham, J. Q. & Green, P. F. The glass transition of thin film polymer/polymer blends: Interfacial interactions and confinement. *Journal of Chemical Physics* **116**, 5801–5806 (2002).

[90] Kim, C., Facchetti, A. & Marks, T. J. Probing the surface glass transition temperature of polymer films via organic semiconductor growth mode, microstructure, and thin-film transistor response. *Journal of the American Chemical Society* **131**, 9122–9132 (2009).

[91] Mirau, P. A. & Lyons, M. Intermolecular interactions and dynamics in polymer/c-60 blends. *Macromolecules* **43**, 625–629 (2010).

[92] Zang, F. *et al.* Glassy carbon as an absolute intensity calibration standard for small-angle scattering. *Metallurgical And Materials Transactions A* **41**, 1151–1158 (2010).

[93] Cerda, J. J., Sintes, T. & Chakrabarti, A. Excluded volume effects on polymer chains confined to spherical surfaces. *Macromolecules* **38**, 1469–1477 (2005).

[94] Brown, D., Mele, P., Marceau, S. & Alberola, N. D. A molecular dynamics study of a model nanoparticle embedded in a polymer matrix. *Macromolecules* **36**, 1395–1406 (2003).

[95] Dionne, P. J., Ozisik, R. & Picu, C. R. Structure and dynamics of polyethylene nanocomposites. *Macromolecules* **38**, 9351–9358 (2005).

[96] Papakonstantopoulos, G. J., Yoshimoto, K., Doxastakis, M., Nealey, P. F. & de Pablo, J. J. Local mechanical properties of polymeric nanocomposites. *Physical Review E* **72** (2005).

[97] Desai, T., Keblinski, P. & Kumar, S. K. Molecular dynamics simulations of polymer transport in nanocomposites. *Journal of Chemical Physics* **122** (2005).

[98] Vacatello, M. Phantom chain simulations of realistically sized polymer-based nanocomposites. *Macromolecular Theory and Simulations* **15**, 303–310 (2006).

[99] Brown, D., Marcadon, V., Mele, P. & Alberola, N. D. Effect of filler particle size on the properties of model nanocomposites. *Macromolecules* **41**, 1499–1511 (2008).

[100] Brown, D., Clarke, J. H. R., Okuda, M. & Yamazaki, T. The preparation of polymer melt samples for computer-simulation studies. *Journal of Chemical Physics* **100**, 6011–6018 (1994).

[101] Neyertz, S. & Brown, D. Preparation of bulk melt chain configurations of polycyclic polymers. *Journal of Chemical Physics* **115**, 708–717 (2001).

[102] Auhl, R., Everaers, R., Grest, G. S., Kremer, K. & Plimpton, S. J. Equilibration of long chain polymer melts in computer simulations. *Journal of Chemical Physics* **119**, 12718–12728 (2003).

[103] Carbone, P., Karimi-Varzaneh, H. A. & Mueller-Plathe, F. Fine-graining without coarse-graining: An easy and fast way to equilibrate dense polymer melts. *Faraday Discussions* **144**, 25–42 (2010).

[104] Merkel, T. C. *et al.* Ultrapermeable, reverse-selective nanocomposite membranes. *Science* **296**, 519–522 (2002).

[105] Macosko, C. W. *Rheology: Principles, Measurements, And Applications* (VCH, 1994).

[106] Dreiss, C. A., Jack, K. S. & Parker, A. P. On the absolute calibration of bench-top small-angle x-ray scattering instruments: a comparison of different standard methods. *Journal of Applied Crystallography* **39**, 32–38 (2006).